

EXPERIMENTS, ANALYSIS, AND DESIGN IMPROVEMENT
FOR NEW-GENERATION BUCKLING-RESTRAINED
BRACES (BRBS)

by
Wenjing Xu

A dissertation submitted to the faculty of
The University of Utah
in partial fulfillment of the requirements for the degree of

Doctor of Philosophy

Department of Civil and Environmental Engineering

The University of Utah

August 2016

Copyright © Wenjing Xu 2016

All Rights Reserved

The University of Utah Graduate School

STATEMENT OF DISSERTATION APPROVAL

The dissertation of Wenjing Xu
has been approved by the following supervisory committee members:

| | | |
|-------------------------------|----------|----------------------------------|
| <u>Pantelides, Chris P.</u> | , Chair | <u>1/8/2016</u> Date Approved |
| <u>Adams, Daniel O.</u> | , Member | <u>1/8/2016</u> Date Approved |
| <u>Bordelon, Amanda C.</u> | , Member | <u>1/8/2016</u> Date Approved |
| <u>Ibarra, Luis Francisco</u> | , Member | <u>1/8/2016</u> Date Approved |
| <u>Reaveley, Lawrence D.</u> | , Member | <u>1/8/2016</u> Date Approved |

and by Barber, Michael Ernest, Chair/Dean of
the Department/College/School of Civil and Environmental Engineering

and by David B. Kieda, Dean of The Graduate School.

ABSTRACT

Buckling-restrained braces (BRBs) are widely used in new and existing buildings to enhance their performance during large earthquakes. The new generation BRB has connection plates welded perpendicular to core plates, which makes the manufacturing easier compared to current construction. The new generation BRB has two connection plates on each end, which makes the pinned end, bolted end, and welded end much easier to construct and connect the BRB to buildings. Nine full-scale experiments carried out in this research demonstrates the ability of new generation BRBs to perform equally well as current generation BRBs.

Research has been done for the buckling force of the core plate and the contact force between concrete and core plate for conventional BRBs, but specific equations for buckling force and contact force considering the friction between concrete and core plates have been developed when the core plate buckles in a number of waves for strong-axis buckling. A theory based on the strut-and-tie model was developed to predict strong or weak axis buckling for a given BRB. In addition, finite element models were developed which are compared to the analytical results for determining the occurrence of strong-axis or weak-axis buckling, as well as the magnitude buckling load.

Allowable ratio of lateral force to BRB axial compressive capacity for a certain casing length and cross-section is determined using finite element analysis, at which BRBs can deform up to 2% interstory drift without global buckling. Simulation of the

hysteretic performance of the nine BRBs tested in full-scale experiments is carried out using finite element analysis with quasistatic cyclic loads, and the results are then compared to the experiments. Finally, the factors which effected the out-of-plane buckling of the gusset plate in one of the experiments are investigated and measures to prevent this are offered.

TABLE OF CONTENTS

| | |
|--|-----|
| ABSTRACT | iii |
| NOMENCLATURE | vii |
| ACKNOWLEDGEMENTS | ix |
| Chapters | |
| 1 INTRODUCTION | 1 |
| 2 LITERATURE REVIEW | 5 |
| 2.1 Testing of BRBs and BRB Frames | 5 |
| 2.2 Review of Core Plate Buckling | 6 |
| 2.3 Review of Design Guidelines for the Steel Casing | 8 |
| 2.4 Review of Analysis of the Out-of-Plane Buckling of Gusset Plate | 10 |
| 3 EXPERIMENTAL RESEARCH | 12 |
| 3.1 Description of Experiments | 12 |
| 3.2 Phenomena Observed in the Tests | 16 |
| 3.3 Evaluation of the BRB Performance | 16 |
| 4 BUCKLING FORCE ON THE CORE FOR STRONG-AXIS BUCKLING | 41 |
| 4.1 Core Buckling Force Derivation | 41 |
| 4.2 Verification with Finite Element Method (FEM) Model of BRBs under Monotonic Axial Compression | 52 |
| 4.3 Verification of Postbuckling Forces from the Derived Equations with the Backbone Curves Obtained from the Tests | 56 |
| 5 STRUT-AND-TIE MODEL FOR THE CROSS-SECTION OF THE BRBS | 68 |
| 5.1 Theory of STM | 68 |
| 5.2 Strut-and-Tie Model Built in BRB Cross-Section | 69 |
| 5.3 General Equation for the Critical Angle | 71 |
| 5.4 Evaluation of the Nodal Zones | 74 |
| 5.5 Calculation of Critical Angle for the Specimens Tested in the Laboratory | 80 |

| | |
|--|-----|
| 6 ANALYTICAL SIMULATION OF BRBS AND CASING THICKNESS REQUIRED FOR LONG BRBS | 85 |
| 6.1 Material Property Determination for BRB Models in ANSYS | 85 |
| 6.2 Comparison of the Simulation Results with Corresponding Test Results | 88 |
| 6.3 Relationship between Thickness of Casing and BRB Length | 91 |
| 7 ANALYSIS OF GUSSET PLATES | 115 |
| 7.1 Code Requirements on Gusset Plate Design..... | 116 |
| 7.2 Calculation of the Design Strength (LRFD) and Allowable Strength (ASD) on the Gusset Plates | 118 |
| 7.3 FEM Simulation of the Top Gusset Plate with Connection Plates in ANSYS | 122 |
| 7.4 Comparison among the Simulation Results | 123 |
| 8 SUMMARY AND CONCLUSIONS..... | 133 |
| APPENDIX CALCULATION OF THE DESIGN STRENGTH (LRFD) AND ALLOWABLE STRENGTH (ASD) OF THE SMALL GUSSET PLATES | 137 |
| REFERENCES | 142 |

NOMENCLATURE

| | |
|-------------|--|
| ACI | American concrete institute |
| AISC | American institute of steel construction |
| BRB | Buckling-restrained brace |
| BRBF | Buckling-restrained-braced frame |
| C-C-C | Compression-compression-compression |
| C-T-T | Compression-compression-tension |
| e | Air gap size between the core plate and the concrete |
| E | Elastic modulus |
| E_{r-co} | Reduced modulus of the core plate |
| E_{r-ca} | Reduced modulus of the steel casing |
| F_B | Contact force for the core plate from the restrainer. |
| F_{ns} | Compressive force in the strut |
| FKN | normal penalty stiffness factor |
| FRP | Fiber reinforced polymer |
| i | Amount of wave number |
| I | Moment of inertia |
| I_s | Moment of inertia in the strong axis |
| I_w | Moment of inertia in the weak axis |
| L_{c-cor} | Critical length of the core plate, which is the length of core plate between |

connection plates in longitudinal direction

| | |
|-----------|---|
| L_{cor} | Total length of the core plate. |
| L_w | Wave length in the weak axis |
| L_s | Wave length in the strong axis. |
| LVDT | Linear variable differential transformer |
| Msi | Million lbf per square in. |
| P | Axial compressive force on the core plate |
| P_E | Euler buckling force on the restrainer |
| P_i | Axial compressive force on the core plate when the core plate has i waves |
| P_y | Yield strength of the core plate |
| PVS | Polyvinyl siloxane |
| t_{ca} | Wall thickness of the casing |
| t_{cor} | Thickness of the core plate |
| T | Tensile force in the tie |
| w_{cor} | Width of the core plate |
| w_{ca} | Width of the casing |
| w_s | Width of the strut |
| w_t | Width of the tie |
| μ | Friction coefficient between the concrete and the core plate |

ACKNOWLEDGEMENTS

I would like to thank my mentor, Dr. Chris Pantelides, for his support and guidance during my educational pursuits. I am grateful for his patience and dedication to help me succeed through his research. Additionally, I would like to express my appreciation for Dr. Lawrence Reaveley, Dr. Daniel Adams, Dr. Amanda Bordelon, and Dr. Luis Ibarra for their support and dedication.

I am grateful to Star Seismic LLC. Without their contributions this research would not have been possible. I would like to thank Mark Bryant, Trevor Nye, Clayton Burningham, Erika Webber, M.J. Ameli, Joel Parks, and Anurag Upadhyay for their assistance in laboratory testing.

Finally, I would like to thank my parents and husband for their love and support, patience, and encouragement during this period of our lives.

CHAPTER 1

INTRODUCTION

The concept of buckling-restrained braces was developed in Japan (1971). Conventional BRBs are composed of a slender steel core continuously supported by concrete inside a steel casing in order to prevent buckling under axial compression. The core and the concrete are decoupled to prevent interaction between them. BRBs appeared in the United States after the 1994 Northridge earthquake and are now widely accepted in building construction. The design of BRBs is regulated in current standards as a displacement-dependent lateral loading resisting solution. Buckling-restrained braces are widely used in both low-rise and high-rise buildings to provide lateral resistance for new and old structures during earthquakes and wind storms, as shown in Figure 1.1.

Current configurations of commercial BRBs have the connection plate and core plate as one piece; the core plate is formed by reducing the cross-section of the steel plate in the middle section (Raddon, B., Pantelides, C., and Reaveley, L., unpublished report). Manufacturing of the core for the current BRB configuration wastes steel material and requires skilled labor and special machinery. To reduce manufacturing time and material cost, BRBs with a new configuration of steel core plates were designed by StarSeismic LLC.

To evaluate the performance of the BRBs with a new configuration of steel core plates, nine full-scale new-generation BRBs were tested in this research at the Structural

laboratory of the University of Utah. During the tests and after opening of the tested BRBs, some phenomena were observed, such as strong-axis and weak-axis buckling of the core plates, bulging of the casing, and out-of-plane buckling of the gusset plate. This research aims to evaluate the performance of the new-generation BRBs, as well as understand and explain the phenomena observed regarding the BRBs.

This dissertation presents research on the new-generation BRBs, including the laboratory tests, analysis of the test data, and explanation of the phenomena observed during the tests. Chapter 2 provides the literature review on the testing of BRBs and BRB frames, core plate buckling, design of the steel casing, and analysis of out-of-plane buckling of gusset plates.

Chapter 3 describes the configuration of new generation BRBs and the experimental setup and loading protocols, evaluates the performance of the new-generation BRBs, and describes the phenomena observed in the tests.

Chapter 4 derives the equations for buckling force on the core plates and the contact force between the concrete and core plates when strong-axis buckling of the core plates occurs. The equations of the buckling force are verified by numerical simulations using finite element analysis and are compared to the test results.

Chapter 5 uses the strut-and-tie model to explain why the strong-axis or weak-axis buckling occurs to the core plates. The general equation is derived for the critical angle between the strut and the tie when core plate buckles in strong axis.

Chapter 6 simulates the BRBs used in nine tests under cyclic axial loading using finite element analysis. The hysteretic loops and hysteretic energy dissipation are compared with those obtained from the tests to verify the simulation results. The same

parameters for the BRB models from the cyclic simulation are used for the model which is used to obtain the critical casing wall thickness for different length of the BRBs when the cross-sectional dimension of the casing is given. The relationship between eccentricity and BRB length for a given cross-sectional dimension of the casing is obtained.

Chapter 7 focuses on the out-of-plane buckling of gusset plates. The tensile and compressive resistant capacity of the gusset plates used in the tests is calculated following the AISC Code (2011). The combination of the gusset plates and the connection plates used in tests 3 through 5 are simulated using finite element analysis under axial load and 1% of axial load as the horizontal load.

Finally, Chapter 8 contains the summary and conclusions generated by the entire research.



Figure 1.1 BRBs applied in the J. William Marriott Library at the University of Utah

CHAPTER 2

LITERATURE REVIEW

A significant amount of research on buckling-restrained braces and their connection assemblies has been performed. The research includes testing of BRBs and BRB frames, analysis of core plate buckling, design guidelines for the BRB casing, and analysis of the out-of-plate buckling of gusset plates.

2.1 Testing of BRBs and BRB Frames

BRBs are commonly composed of steel casing and steel core surrounding by concrete, which are called steel BRBs. Many steel BRBs have been tested (Chou et al. 2014; Daniels 2006; Fahnstock et al. 2007; Genna et al. 2012; Ju et al. 2009; Liu et al. 2012; Mazzolani et al. 2009; Palazzo et al. 2009; Raddon, B., Pantelides, C., and Reaveley, L., unpublished report; Romero, P., Reaveley, L., Miller, P., and Okahashi, T., unpublished report; Staker 2002; Sun et al. 2011; Tremblay et al. 2006; Zhao et al. 2014). Miller et al. (2012) developed and tested self-centered BRBs with nickel-titanium shape memory alloy restrained by three steel tubes. Chou et al. (2014) developed a steel dual-core self-centering brace with post-tensioned tendons.

New materials for either casing or core plate were tested as well, such as aluminum (Wang et al. 2013), Polyvinyl chloride (PVS) pipe (Rahai et al. 2009), and Fiber-reinforced plastic (FRP) rolled sheets (El-Tawil et al. 2009; Rahai et al. 2009).

Compared to steel, aluminum has lower strength, so BRB made of aluminum has lower compressive capacity, PVS is too brittle, and FRP is more expensive.

Several kinds of configuration of cross-section of core have been tested as well, including round (Palazzo et al. 2009), rectangular (Daniels 2006; Mazzolani et al. 2009; Staker 2002; Sun et al. 2011), H-shaped (Ju et al. 2009), and core with steel angle (Zhao et al. 2014). To reduce the stress concentration in the transitional zone of core, the core is either taped (Daniels 2006) or cut with radius (Raddon, B., Pantelides, C., and Reaveley, L., unpublished report). Cutting core with radius requires skilled labor and special machinery. To make BRB easier to manufacture BRBs with connection plate prismatic to core were tested in this research.

2.2 Review of Core Plate Buckling

When compressive axial force applied on a core plate exceeds the critical buckling force, the core plate buckles, and then the contact force between core plate and the restrainer (concrete and steel casing) occurs. It helps to determine if the BRB buckles under a certain load if the axial compressive force on the core plate and the contact force between the core plate and the concrete can be determined. Shen et al. (2007) proposed a mechanical model of line contact between the core plate and steel casing with finite stiffness under axial compression. Formulae were derived for deflection, moment, shear, and contact reaction of the steel casing during point contact and line contact between the core plate and the steel casing. Wu et al. (2012) established the equilibrium equation of a member subjected to axial and lateral force. Equations were derived to describe the deflection curve of the steel core plate under point contact and line contact. The equilibrium equation of the core plate with the axial compression and the contact force

was described in Eq. (2.1), in which P was the compressive force and T was the contact force between restrainer and the core plate. This equation is used for development of general equations for contact force between concrete and core plate, and axial compression on the core plate considering the friction between concrete and core plate. Friction between concrete and core plate was not considered in the research of Wu et al. (2012) but it will be considered in this research.

$$Py - Tx + EI \frac{d^2y}{dx^2} = 0 \quad (2.1)$$

Lin et al. (2012) performed a series of cyclic load tests on a three-story, single-bay, full-scale, buckling-restrained-braced frame (BRBF). The frame responses were satisfactorily predicted by both OpenSees and PISA3D analytical models. The OpenSees and PISA3D were capable of performing inelastic analysis of the structural system for cyclic loads. The authors also estimated the local bulging force demand acting on the steel casing, which was defined by Eq. (2.2):

$$f_{p,max} = P_{max} \frac{2s}{l_w/2} \quad (2.2)$$

where P_{max} was the maximum compressive load, $f_{p,max}$ was the maximum bulging force given by the core plate, s was the air gap size, and l_w was the wave length defined by Eq. (2.3):

$$P_y = \frac{\pi^2(EI_w)_{eff}}{(l_w/2)^2} \quad (2.3)$$

where $(EI_w)_{eff}$ is the equivalent flexural stiffness of the core plate, and P_y is the nominal yield strength of the core plate.

The equations of wave length were developed for either strong-axis buckling or weak-axis buckling occurring on the core plate. Wu et al. (2014) conducted cyclic

loading tests and finite element analyses for six novel all-steel buckling-restrained braces (BRBs) using different loading patterns to investigate the core plate high-mode buckling phenomenon. Eqs. (2.4) and (2.5) were used to calculate the wavelength for strong-axis buckling and weak-axis buckling of the steel core plates, respectively. After the wave length is calculated, the wave number can be determined as well when the length of the core plate is certain. These equations will be used to determine the wave number of a given BRB.

$$L_s = \sqrt{\frac{4\pi^2(EI_s)_{eff}}{P_y}} = \sqrt{\frac{4\pi^2 \times 0.02EI_s}{F_y w_c t_c}} \approx 6w_c \quad (2.4)$$

$$L_w = \sqrt{\frac{4\pi^2(EI_w)_{eff}}{P_y}} = \sqrt{\frac{4\pi^2 \times 0.06EI_w}{F_y w_c t_c}} \approx 11t_c \quad (2.5)$$

where E was the modulus of elasticity of the core plate; I_s and I_w is the moment inertia of the core plate about the strong axis and weak axis, respectively; $(EI_s)_{eff}$ and $(EI_w)_{eff}$ are the equivalent flexural stiffness of the core plate about the strong axis and weak axis, respectively; P_y is the nominal yielding force of the core plate; F_y is the nominal yielding stress of the core plate; w_c is the width of the core plate; t_c is the thickness of the core plate; L_w is the wavelength for strong-axis buckling of the core plate; and L_s is the wavelength for weak-axis buckling of the core plate. In the above expressions, the yield strength of the steel core plate was assumed as 40.9 ksi.

2.3 Review of Design Guidelines for the Steel Casing

The steel casing helps to prevent the global buckling of the BRB, so the buckling capacity of the BRB is vital. The most famous casing design rule followed the research of Watanabe et al. (1988), who suggested that $\frac{P_e}{P_y} \geq 1.5$ to make sure that the braces could

show stable hysteretic performance, where P_e is the Euler buckling load of the steel casing and P_y is the yield load of the core plate. Midorikawa et al. (2012) introduced the buckling load of the restrained part, P_E , shown in Eq. (2.6) from Euler's buckling load equation.

$$P_E = \frac{\pi^2}{L^2} (E_s I_s + E_m I_m) \quad (2.6)$$

where E_s , E_m are the moduli of elasticity of the steel casing and mortar, respectively; I_s , I_m are the moment of inertia of the steel casing and mortar, respectively; and L is the length of the core plate.

Eq. (2.7) was also proposed for the restraining force, F_B , applied from the casing and concrete to the core plate.

$$F_B = \frac{2PS}{L_m + \mu S} \quad (2.7)$$

where F_B is the restraining force, P is the compressive axial force, L_m is the half wavelength, μ is the friction coefficient between concrete and steel core plate, and S is the wave amplitude. The wavelength is the horizontal distance between two nearest peaks of the buckling steel core.

This ratio suggested by Watanabe et al. (1988) was obtained from authors' test result, which are five BRBs with length of less than 11 ft., while BRBs tested in this research are more than 18 ft. long. There was some uncertainty as to whether the ratio of Watanabe et al. (1988) still worked for longer BRBs. Simulation method with ANSYS will be used to find the critical casing thickness to prevent global buckling of BRBs, and the critical thickness of casing obtained from the simulation result will be compared with those obtained using the ratio of Watanabe et al. (1988).

2.4 Review of Analysis of the Out-of-Plane Buckling of the Gusset Plate

Gusset plates connect BRBs to beam-column frame in structures, so gusset plates have to be stiff enough to make sure BRB can fully perform its duty in an earthquake. Therefore, Gusset plates play an important role to make sure BRBs can fully perform during the earthquake.

AISC (2011) contains equations for the calculation of the tensile-resistant, shear-resistant, and compressive-resistant for the gusset plates.

Koetaka et al. (2008) proposed design criteria for BRBs to prevent out-of-plane buckling of the gusset plate and conducted a loading test to verify the criteria. Tsai et al. (2008) performed a series of pseudo-dynamic tests (PDTs) of a full-scale 3-story 3-bay buckling-restrained braced frame (BRBF) using concrete-filled tubes (CFT). The authors evaluated the design of gusset connections and the effects of the added edge stiffeners in improving the seismic performance of gusset connections. Chou et al. (2009) investigated the compressive strength and behavior of BRB frame (BRBF) central gusset plates in an inverted-V-braced configuration. Analytical results for both the BRBF model and central gusset plate connection model utilizing finite element models reasonably predicted the ultimate load of the gusset plate obtained from the frame test. Chou et al. (2012) evaluated a three-story buckling-restrained braced frame (BRBF) with a single diagonal-sandwiched BRB and a corner gusset in cyclic tests of a one-story, one-bay BRBF subassembly, and performed dynamic analyses of the frame subjected to earthquakes. Okazaki et al. (2012) examined the out-of-plane stability of buckling-restrained braces (BRBs) by performing large-scale shake table tests at E-Defense. Takeuchi et al. (2012) discussed the stability of BRBs and confirmed them by a cyclic loading test using out-of-

plane displacement. Hikino et al. (2013) examined the out-of-plane stability of buckling-restrained braces (BRBs) with Large-scale shake table tests performed at E-Defense. Two specimens were subjected repeatedly to a near-fault ground motion with increasing amplification. Takeuchi et al. (2014) presented BRB stability concepts, including their bending-moment transfer capacity at restrainer ends for various connection stiffness values with initial out-of-plane drifts.

All research above focused on the out-of-plane buckling of gusset plates in strong-axis, which is caused by movement of the frame during the earthquake. The out-of-plane buckling of gusset plate in this research is about weak-axis. To explain this phenomenon, AISC code (2011) about the resistant capacity of gusset plate will be followed. And the contribution of connection plate to stiffness of gusset plate will be investigated as well by following AISC code (2011).

CHAPTER 3

EXPERIMENTAL RESEARCH

BRBs tested for this research were designed and built by Star Seismic LLC., and tested at the Structural Laboratory at the University of Utah. In this section, the test setup used, as well as the phenomena observed from these tests, will be described. The compression strength adjustment factor, β , strain hardening adjustment factor, ω , cumulative inelastic deformation, η , and cumulative energy dissipation, E , are defined and calculated. The observed phenomena are combined with the plotted hysteretic loops.

3.1. Description of Experiments

BRBs are widely used in new and old buildings in order to absorb the energy released from large earthquakes. In this section, the construction of a new-generation BRB is described, the connection details between a BRB and the loading frame are expressed, and the loading protocol is listed.

3.1.1 BRB Specimens

Current BRBs that are in use in the market have the connection plate and the core plate constructed as one piece. The core plate is formed by reducing the cross-section of the steel plate in its middle section, as shown in Figure 3.1. Manufacturing of the core for current BRBs wastes steel material and requires skilled labor and special machinery. To reduce manufacturing time and material costs, BRBs with a new configuration are

developed.

The new-generation BRB has the connection plates welded perpendicular to the core plates as shown in Figure 3.2, which makes the manufacturing easier compared to the current construction. Moreover, by manufacturing BRBs this way, there is no extra cutting of the core plate, so no steel is wasted; in addition, welding is much easier to perform than creating the radiused copes. Moreover, the new-generation BRB has two connection plates at each BRB end, which makes the pinned, bolted, and welded connections easier to construct.

These new BRBs consist of concrete embedded inside of a steel casing, as well as one or two core plates welded to four connection plates, with air gaps around both core plates and connection plates, and air intervals between the connection plates and the concrete, as shown in Figure 3.3.

Nine new-generation BRBs were tested in this investigation, in full-scale experiments performed at the Structures Laboratory of the University of Utah. The characteristics of the nine specimens are summarized in Table 3.1. All BRBs had a square cross-section and core plates ranging in width from 6.25 to 10 in. Four of the BRBs had dual core plates and five had a single core plate; the thickness of a single plate was 1 in. (t_{co}). The material properties of all core plates were the same: The yield stress was 40.9 ksi and the ultimate strength 59.7 ksi. Eight BRBs had a length of 219 in., and the remaining one was 209 in. long. The outside cross-sectional dimensions of the casing were either 12 in. \times 12 in. or 10 in. \times 10 in.; the steel casing wall was $\frac{1}{4}$ in. thick for all specimens.

3.1.2 End Connection Details

Each BRB was brought to the load frame vertically, as shown in Figure 3.4; the top gusset plate was then attached to the hydraulic actuator that has an inline load cell. There was an additional plate welded perpendicular to the bottom gusset plate, which is called the base of the bottom gusset plate, mounted in the horizontal direction, as shown in Figure 3.5. Two vertical steel plates, parallel to the bottom gusset plate, were bolted to the east and west walls of a tie-down steel box; once the bolts were tightened to the walls of the tie-down steel box, the bottom gusset plate was fixed to the ground and tension could be applied to the BRB.

Element tests, as well as subassembly tests, were performed in the lab. Two BRBs were analyzed with the element test, in which the BRB was assembled vertically to the load frame without any initial moment. Seven BRBs were tested using a subassembly test, in which the BRB was assembled vertically to the loading frame with an initial moment that was produced by shifting the bottom of the BRB back to the offset locations. Each BRB was assembled to the loading frame with either bolted or welded boundary conditions. The end connection conditions and the test method for each specimen are listed in Table 3.2.

The BRB is assembled to the building by being connected to the beam-column frame, as shown in Figure 3.6 by the solid line. When a horizontal load, P , is applied due to an earthquake, the BRB is in compression and the buckling restrained brace frame (BRBF) deforms, as shown by the dotted line in Figure 3.6. Bending moments are created at both ends of the BRB due to the horizontal movement of the frame, which depends on the displacement, Δ and connection details; this displacement increases gradually.

To derive the performance of the BRB in the BRBF, the subassembly test method specified in the AISC-341 (2010) is used. The procedure of installing the BRB into the loading frame for the subassembly test is shown in Figure 3.7. The BRB is set up vertically between the gusset plates as shown in Figure 3.7 (a). The bolts are then inserted in the bolt holes, attaching the BRB to the gusset plates, as shown in Figure 3.7 (b). The bottom gusset plate is then moved to the left so that the BRB will have a 3 in. offset from the original location, as shown in Figure 3.7 (c). The screws on the top and bottom gusset plates are then tightened, as shown in Figure 3.7 (d). The bottom gusset plate is then moved back to the original location; bending moments are created on both ends of the BRB, as shown in Figure 3.7 (e).

3.1.3 Loading Protocols

The AISC seismic provisions require that BRB design should be based on results from qualifying cyclic tests. The procedures and acceptance criteria of these tests are stipulated in AISC-341 (2010); braces must be tested up to the design story drift (2% interstory drift) and achieve a cumulative inelastic deformation 200 times the yield deformation. Any test protocol that meets these two criteria is permitted, but most test protocols consist of two cycles at $\pm 100\%$ of the yield displacement of the core plate, followed by a displacement corresponding to $\pm 0.5\%$ interstory drift. Then the displacement increases with an increment corresponding to $\pm 0.5\%$ interstory drift until $\pm 2\%$ interstory drift. Additional cycles are required to achieve a cumulative inelastic axial deformation of at least 200 times the yield deformation, which is only required for element specimens, not required for subassembly specimens. The yield displacement of the core plate is predicted based on the yield stress of the core plates.

A displacement control mode was used in all quasi-static cyclic tests with a loading rate of 0.02 in./sec. The actuator loading used is shown in Figure 3.8 and follows the requirements of the loading sequence of the AISC seismic provisions. The test typically was started in tension (positive displacement) and two cycles were run for each displacement until failure.

3.2. Phenomena Observed in the Tests

During the tests, BRBs deformed in a number of ways. Some BRBs had strong-axis buckling of the core, such as BRBs in tests 1 and 5; some BRBs had weak-axis buckling of the core, such as the BRB in test 3; out-of-plane buckling of the gusset plate was also observed once in test 5; fracture of the connection plate was also observed in test 6, as well as bulging of the casing in test 1. These phenomena are described in Table 3.3. Figure 3.9 shows the major deformations of the BRBs after the tests.

To fully understand how the BRB works, further research was performed regarding core plate buckling (strong axis or weak axis), gusset plate buckling, and casing bulging. In addition, finite element analysis will be used to model the hysteretic performance of BRBs in the tests.

3.3. Evaluation of the BRB Performance

AISC-341 (2010) Section K4.3 specifies the acceptance requirements for BRB performance, including stability of the hysteretic loops; the compression strength adjustment factor, β ; the strain hardening adjustment factor, ω ; the cumulative inelastic deformation, η ; and the cumulative energy dissipation, E . The calculations in this section are based on the relative displacement at the two ends of the BRB, measured using linear

variable displacement transducers (LVDTs) and the force from the actuator load cell.

3.3.1. Hysteretic Behavior

Hysteresis curves are conventionally used to demonstrate whether the BRB is stable under cyclic loading. Figure 3.10 shows the hysteresis loops for the nine specimens, which are all stable up to a displacement corresponding to 2% of the story drift without fracture, and therefore meet AISC-341 (2010) requirements. The strain in the core plates, which is the ratio of the maximum displacement over their length, ranged from 2.89% to 4.16%, which is greater than the yielding strain of the steel. The strains achieved in the core plates for each BRB specimen are listed in Tables 3.4 through 3.12. It can be seen from the hysteretic loops that BRBs in tests 1, 2, 3, 7, and 9 failed in tension and BRBs in tests 4, 5, 6, and 8 failed in compression. Combining the hysteretic behavior with the phenomena observed in Section 3.2, it can be seen that if the force declines in tension and the BRB fails in tension (first quadrant in the hysteretic loops), the BRB usually fails due to a fractured steel core. If the force decreases or drops significantly in compression (fourth quadrant in the hysteretic loops), the core experiences buckling.

3.3.2. Compression Strength Adjustment Factor, β

Factor β is calculated as the ratio of maximum compressive force to maximum tensile force of the specimen measured in the same loading cycle from the qualification tests specified in AISC-341 (2010) seismic provision Section K3.4c for the expected deformation. When the building with BRBs is under earthquake or wind excitation, the BRBs will go through a combination of tension and compression loading pattern.

Generally, concrete-filled BRBs have a higher compressive capacity than tensile capacity due to the friction between the concrete and the core and the confinement from the concrete after the core deforms. Therefore, AISC-341 (2010) requires factor β to be greater than 1.0 but smaller than 1.3. The definition of factor β is expressed in the Eq. 3.1.

$$1.0 < \beta = \frac{P_{max}}{T_{max}} < 1.3 \quad (3.1)$$

where β is the compression strength adjustment factor, P_{max} is the maximum compressive force, and T_{max} is the maximum tensile force in the corresponding loading cycle.

Since the test typically starts with tension, the first tension cycle in each step has an overall displacement that is not equal to the next compression cycle. For this reason, the first cycle values of β are not calculated.

From Tables 3.4 to 3.12, it can be seen that the values for factor β vary from 0.92 to 1.28. All are below 1.3, which meets the AISC-341 (2010) requirements. Test 6 has a couple of β s smaller than 1.0 in the beginning of the test because the connection between the bottom gusset plate and the ground was loose.

3.3.3. Strain Hardening Adjustment Factor, ω

Factor ω is the ratio of the maximum tension force measured from the qualification tests specified in section K3.4c to the measured yield force, $R_y P_{y_{sc}}$, of the specimen. The definition of factor ω is expressed in equation 3.2. Strain hardening is the strengthening of a metal by plastic deformation, which means that the tension in the plastic zone is larger than the yield strength of the material. Therefore, ω should be larger than 1.0.

$$\omega = \frac{T_{max}}{R_y P_{y_{sc}}} \geq 1.0 \quad (3.2)$$

where T_{max} is the maximum tensile force, R_y is the ratio of the expected yield stress to the specified minimum yield stress F_y , and $P_{y_{sc}}$ is the axial yield strength of the steel core. R_y need not be applied if $P_{y_{sc}}$ is established using yield stress determined from a coupon test, which is the case for all of these tests.

Strain hardening happens after the material yields. The displacement applied on the brace in the first loading step is the yield displacement of the brace. From Tables. 3.4 to 3.12, it can be seen that most BRBs started strain hardening after the first loading step and all BRBs eventually had strain hardening in the later loading steps. The maximum value of ω ranged from 1.42 to 1.67. This range is wide because the cross-sectional areas of core are not the same.

3.3.4. Cumulative Inelastic Deformation, η

The inelastic deformation μ_i is the permanent or plastic portion of the axial displacement of a buckling-restrained brace, divided by the length of the yielding portion of the brace. This term shows how stretchable the brace is. For each loading cycle, there are four plastic deformations: the loading path from zero force location to maximum displacement in tension, the loading path from maximum displacement in tension to zero load location, the loading path from the zero load location to the maximum displacement in compression, and the loading path from maximum displacement to the zero load location. Therefore, the inelastic deformation for each cycle, μ_i , can be expressed as

$$\mu_i = \frac{2(\Delta_{max-compression} + \Delta_{max-tension})}{\Delta_{by}} - 4 \quad (3.3)$$

where μ_i is the inelastic deformation for each cycle, $\Delta_{max-compression}$ is the maximum

displacement of the brace in compression, $\Delta_{max-tension}$ is the maximum displacement of the brace in tension, and Δ_{by} is the yield displacement of the brace.

AISC 341-10 Section K3.3 requires that cumulative inelastic axial ductility capacity is no less than 200 times the yield displacement. This means that for a BRB to qualify, the plastic deformation created by the end of the test must be at least 200 times the elastic deformation.

The cumulative inelastic deformation is obtained from the Eq. (3.4):

$$\eta = \sum_{i=1}^n \mu_i \quad (3.4)$$

where η is the cumulative inelastic deformation, and i is the loading cycle number.

From Tables 3.4 to 3.12, it can be seen that the minimum cumulative inelastic deformation is 391 for test 8 with the small cross-sectional area of a single core plate, and the maximum is 617 for test 1 with the large cross-sectional area of a dual core. The nine specimens exceed the AISC 341 cumulative inelastic deformation requirement of 200 times the yield displacement by a factor of 2.0 to 3.1.

3.3.5. Cumulative Energy Dissipation, E

During an earthquake, buildings shake and deform. To prevent the buildings with BRBs installed from experiencing major cracking and failure, energy must be dissipated by the BRBs. Cumulative energy dissipation is the term which measures how much energy can be dissipated by a BRB.

The energy dissipation for each loading increment can be calculated from Eq. (3.5):

$$E_{i+1} = \frac{(P_{j+1} + P_j)(x_{j+1} - x_j)}{2} \quad (3.5)$$

where P_j and P_{j+1} are the forces at the loading time of j and $j + 1$, respectively; x_j and

x_{j+1} are the displacement at the loading time of j and $j + 1$, respectively.

The cumulative energy dissipation is a summation of the energy for each loading step, shown in Eq. (3.6):

$$E = \sum_{j=1}^{n-1} E_{j+1} \quad (3.6)$$

where E_{j+1} is the energy dissipation for each loading step, E is the cumulative energy dissipation, and j is the loading time.

Cumulative energy dissipation for each test is calculated in Tables 3.4 to 3.12 and plotted in Figure 3.11. Cumulative hysteretic energy dissipation for specimens 1 through 5 and specimen 9 is higher than that for specimens 6 through 8. BRBs in tests 1 through 5 and 9 have the same cross-sectional casing dimensions of 12 in. \times 12 in. \times 0.25 in. and a steel core cross-sectional area equal to or larger than 10 in.², as shown in Table 3.1. BRBs in tests 6 to 8 have the same cross-sectional casing dimensions of 10 in. \times 10 in. \times 0.25 in. and a steel core cross-sectional area of 7.75 in.²; thus, the larger the cross-sectional area of the core the higher is the hysteretic energy dissipated.

Figure 3.12 shows the cumulative energy dissipation per unit cross-sectional area of the core plates. Starting at the top of the figure, the cross-sectional area of the core plates increases from 7.75 in.² to 18.5 in.²; the smaller the core cross-sectional area, the more efficient the BRB is regarding cumulative energy dissipation per unit cross-sectional area of the core plates. For unit cross-sectional area of the core plates, the larger the perimeter of the core plate, the greater the friction force and the greater the compressive force needed to move the same amount of displacement. In other words, the larger the ratio of the perimeter to the cross-sectional area of the core, the greater the compression needed for BRB to move the same distance. The greater compression force

in the same distance results in the greater cumulative energy dissipation. From Table 3.1, it can be seen that the BRBs with the smallest cross-sectional area have larger ratio of perimeter to the cross-sectional area. Therefore, the BRB with a small cross-sectional area of core is more efficient.

3.3.6. Comparison with Current Generation BRB

Raddon et al. (Raddon, B., Pantelides, C., and Reaveley, L.) reported test results on a current-generation BRB with pinned connections; it had a cross-sectional area of 19 in.² using three steel core plates. The BRBs in tests 1, 2 and 4 of the present investigation have a cross-sectional area of 18.5 in.² which is similar to the BRB tested by Raddon et al. (Raddon, B., Pantelides, C., and Reaveley, L.); this BRB was tested as an element with only uniaxial load and pinned connections to the gusset plates. In test 1, the new-generation BRB was tested as an element under uniaxial load only and was bolted. BRBs in tests 2 and 4 were subassembly tests with both uniaxial load and initial moment, as described in Figure 3.7. The BRB in test 2 was bolted while the BRB in test 4 was welded. The cumulative hysteretic energy dissipation for these four tests is plotted in Figure 3.13; the new-generation BRB in test 1 dissipated a similar amount of hysteretic energy as the conventional BRB. Furthermore, comparing new-generation BRBs in test 1 to tests 2 and 4 shows that the BRB in the element test dissipates more energy than the subassembly tests, which shows that subassembly tests are more severe than element tests because of the initial moment in subassembly tests. Moreover, even though BRBs in tests 2 and 4 were tested with different connections to the gusset plates, the cumulative hysteretic energy dissipation was similar.

Table 3.1
Material properties and geometry of the BRB specimens

| Test # | Wco in. | Tco in. | Core type | Aco in. ² | The ratio of perimeter to area of core/, in. | Lc-co in. | Ltot in. | Casing in. |
|--------|---------|---------|-----------|----------------------|--|-----------|----------|------------|
| 1 | 9.25 | 1 | Dual | 18.5 | 1.2 | 123 | 219 | 12x12x0.25 |
| 2 | 9.25 | 1 | Dual | 18.5 | 1.2 | 123 | 219 | 12x12x0.25 |
| 3 | 6.25 | 1 | Dual | 12.5 | 1.3 | 135 | 209 | 12x12x0.25 |
| 4 | 9.25 | 1 | Dual | 18.5 | 1.2 | 123 | 219 | 12x12x0.25 |
| 5 | 10 | 1 | Single | 10 | 2.2 | 153 | 219 | 12x12x0.25 |
| 6 | 7.75 | 1 | Single | 7.75 | 2.3 | 157 | 219 | 10x10x0.25 |
| 7 | 7.75 | 1 | Single | 7.75 | 2.3 | 157 | 219 | 10x10x0.25 |
| 8 | 7.75 | 1 | Single | 7.75 | 2.3 | 157 | 219 | 10x10x0.25 |
| 9 | 10 | 1 | Single | 10 | 2.2 | 153 | 219 | 12x12x0.25 |

Table 3.2
End connection and test methods for the specimens

| Test # | Shape of BRB casing | End Connection | Test method |
|--------|---------------------|----------------|---------------|
| 1 | Square | Bolted | element |
| 2 | Square | Bolted | subassemblage |
| 3 | Square | Bolted | element |
| 4 | Square | Welded | subassemblage |
| 5 | Square | Welded | subassemblage |
| 6 | Square | Bolted | subassemblage |
| 7 | Square | Bolted | subassemblage |
| 8 | Square | Bolted | subassemblage |
| 9 | Square | Welded | subassemblage |

Table 3.3
Test phenomena and failure mode

| Test # | Specimen # | Test phenomena | Buckling direction |
|--------|------------|--|-------------------------------|
| 1 | PB750b1 | Fracture occurred on both ends of core plates; Casing bulged at mid-height. | Strong-axis buckling |
| 2 | PB750b2 | Fracture occurred on core plates at mid-height. | - |
| 3 | PB500b | Buckling occurred on core plates | Weak-axis buckling |
| 4 | PC750w1 | Out-of-plane buckling occurred on the top gusset plate | - |
| 5 | PW400b1 | Core plate buckled | Strong-axis buckling |
| 6 | PB315b1 | Fracture occurred on the bottom connection plate | Weak and strong-axis buckling |
| 7 | PB315b2 | BRB Failed in tension. Core plate broke at middle-height. Slightly weak axis buckling occurred. | Weak-axis buckling |
| 8 | PB315b3 | Casing bulged at the top end. There was big weak axis-buckling happened on the core plate at the top. Strong-axis buckling occurred on the rest part of the BRB. | Strong and weak-axis buckling |
| 9 | PW400b2 | Casing bulged on the bottom nearby where the connection plates stopped | Weak-axis buckling |

Table 3.4
Parameters calculated for test 1

| Step | Cycles | Tension, maximum | | | Compression, maximum | | | Energy Dissipation, kip-in | | β | ω | $\beta\omega$ | μ | η |
|------|--------|------------------|--------|----------------|----------------------|--------|----------------|----------------------------|------------|---------|----------|---------------|-------|--------|
| | | F, kips | D, in. | ϵ , % | F, kips | D, in. | ϵ , % | Per cycle | Cumulative | | | | | |
| 1 | 1 | 671 | 0.22 | 0.18 | -789 | -0.24 | -0.19 | 78 | 78 | | 0.89 | -1.04 | 0.34 | 0.34 |
| | 2 | 703 | 0.21 | 0.17 | -727 | -0.22 | -0.18 | 41 | 120 | -1.03 | 0.93 | -0.96 | 0.03 | 0.37 |
| 2 | 1 | 800 | 0.65 | 0.53 | -788 | -0.64 | -0.52 | 1182 | 1301 | | 1.06 | -1.04 | 8.35 | 8.72 |
| | 2 | 752 | 0.65 | 0.53 | -778 | -0.64 | -0.52 | 1160 | 2461 | -1.03 | 1.00 | -1.03 | 8.34 | 17.07 |
| 3 | 1 | 802 | 1.31 | 1.07 | -915 | -1.30 | -1.06 | 3167 | 5627 | | 1.06 | -1.21 | 20.92 | 37.98 |
| | 2 | 883 | 1.31 | 1.07 | -937 | -1.30 | -1.06 | 3296 | 8923 | -1.06 | 1.17 | -1.24 | 20.89 | 58.87 |
| 4 | 1 | 931 | 1.98 | 1.61 | -1023 | -1.97 | -1.60 | 5778 | 14701 | | 1.23 | -1.36 | 33.61 | 92.49 |
| | 2 | 970 | 1.98 | 1.61 | -1031 | -1.97 | -1.60 | 5912 | 20613 | -1.06 | 1.28 | -1.37 | 33.59 | 126.08 |
| 5 | 1 | 1003 | 2.63 | 2.14 | -1107 | -2.63 | -2.14 | 8611 | 29224 | | 1.33 | -1.47 | 46.11 | 172.19 |
| | 2 | 1042 | 2.64 | 2.14 | -1116 | -2.62 | -2.13 | 8793 | 38018 | -1.07 | 1.38 | -1.48 | 46.10 | 218.29 |
| 6 | 1 | 1074 | 3.52 | 2.86 | -1207 | -3.51 | -2.86 | 12805 | 50823 | | 1.42 | -1.60 | 63.02 | 281.30 |
| | 2 | 1119 | 3.52 | 2.87 | -1218 | -3.51 | -2.86 | 13118 | 63941 | -1.09 | 1.48 | -1.61 | 63.01 | 344.31 |
| 7 | 1 | 1144 | 4.43 | 3.60 | -1263 | -4.42 | -3.59 | 17286 | 81226 | | 1.52 | -1.67 | 80.29 | 424.60 |
| | 2 | 1177 | 4.43 | 3.60 | -1243 | -4.42 | -3.59 | 17104 | 98330 | -1.06 | 1.56 | -1.65 | 80.28 | 504.88 |
| 8 | 1 | 1186 | 5.14 | 4.18 | -1275 | -5.12 | -4.17 | 13895 | 112226 | | 1.57 | -1.69 | 93.71 | 598.60 |
| | 2 | 1102 | 2.38 | 1.93 | | | | 1793 | 114019 | | | | 18.63 | 617.23 |

Table 3.5
Parameters calculated for test 2

| Step | Cycle | Tension, maximum | | | Compression, maximum | | | Energy Dissipation, kip-in | | β | ω | $\beta\omega$ | μ | η |
|------|-------|------------------|--------|----------------|----------------------|--------|----------------|----------------------------|------------|---------|----------|---------------|-------|--------|
| | | F, kips | D, in. | ϵ , % | F, kips | D, in. | ϵ , % | Per cycle | Cumulative | | | | | |
| 1 | 1 | 630 | 0.27 | 0.22 | -752 | -0.30 | -0.25 | 182 | 182 | | 0.83 | -1.00 | 1.79 | 1.79 |
| | 2 | 702 | 0.27 | 0.22 | -712 | -0.29 | -0.24 | 143 | 325 | -1.01 | 0.93 | -0.94 | 1.72 | 3.51 |
| 2 | 1 | 750 | 0.65 | 0.53 | -727 | -0.65 | -0.53 | 1052 | 1376 | | 0.99 | -0.96 | 9.16 | 12.67 |
| | 2 | 718 | 0.65 | 0.53 | -728 | -0.65 | -0.53 | 1045 | 2422 | -1.01 | 0.95 | -0.96 | 9.16 | 21.83 |
| 3 | 1 | 762 | 1.31 | 1.07 | -857 | -1.31 | -1.06 | 2935 | 5357 | | 1.01 | -1.13 | 22.56 | 44.39 |
| | 2 | 843 | 1.31 | 1.07 | -883 | -1.30 | -1.06 | 3069 | 8426 | -1.05 | 1.12 | -1.17 | 22.56 | 66.95 |
| 4 | 1 | 887 | 1.98 | 1.61 | -964 | -1.97 | -1.60 | 5426 | 13853 | | 1.18 | -1.28 | 36.10 | 103.05 |
| | 2 | 926 | 1.98 | 1.61 | -981 | -1.97 | -1.60 | 5567 | 19419 | -1.06 | 1.23 | -1.30 | 36.09 | 139.14 |
| 5 | 1 | 958 | 2.63 | 2.14 | -1052 | -2.63 | -2.14 | 8154 | 27573 | | 1.27 | -1.39 | 49.42 | 188.56 |
| | 2 | 994 | 2.64 | 2.14 | -1072 | -2.63 | -2.14 | 8357 | 35930 | -1.08 | 1.32 | -1.42 | 49.42 | 237.98 |
| 6 | 1 | 1028 | 3.52 | 2.86 | -1158 | -3.51 | -2.86 | 12242 | 48172 | | 1.36 | -1.53 | 67.44 | 305.42 |
| | 2 | 1071 | 3.52 | 2.86 | -1188 | -3.51 | -2.86 | 12623 | 60795 | -1.11 | 1.42 | -1.57 | 67.44 | 372.86 |
| 7 | 1 | 1105 | 4.43 | 3.60 | -1277 | -4.42 | -3.59 | 17087 | 77882 | | 1.46 | -1.69 | 85.85 | 458.71 |
| | 2 | 1126 | 3.04 | 2.47 | | | | 3217 | 81099 | | | | 26.82 | 485.53 |

Table 3.6
Parameters calculated for test 3

| Step | Cycle | Tension, maximum | | | Compression, maximum | | | Energy Dissipation, kip-in | | β | ω | $\beta\omega$ | μ | η |
|------|-------|------------------|--------|----------------|----------------------|--------|----------------|----------------------------|------------|---------|----------|---------------|-------|--------|
| | | F, kips | D, in. | ϵ , % | F, kips | D, in. | ϵ , % | Per cycle | Cumulative | | | | | |
| 1 | 1 | 425 | 0.27 | 0.20 | -511 | -0.30 | -0.22 | 76 | 76 | | 0.83 | -1.00 | 1.49 | 1.49 |
| | 2 | 483 | 0.28 | 0.21 | -482 | -0.29 | -0.21 | 69 | 145 | -1.00 | 0.95 | -0.94 | 1.49 | 2.98 |
| 2 | 1 | 517 | 0.65 | 0.48 | -501 | -0.65 | -0.48 | 669 | 814 | | 1.01 | -0.98 | 8.52 | 11.49 |
| | 2 | 485 | 0.65 | 0.48 | -493 | -0.65 | -0.48 | 673 | 1487 | -1.01 | 0.95 | -0.97 | 8.49 | 19.98 |
| 3 | 1 | 504 | 1.31 | 0.97 | -584 | -1.31 | -0.97 | 1934 | 3421 | | 0.99 | -1.14 | 21.19 | 41.17 |
| | 2 | 565 | 1.31 | 0.97 | -598 | -1.31 | -0.97 | 2019 | 5439 | -1.06 | 1.11 | -1.17 | 21.19 | 62.36 |
| 4 | 1 | 597 | 1.98 | 1.47 | -664 | -1.97 | -1.46 | 3620 | 9060 | | 1.17 | -1.30 | 33.99 | 96.35 |
| | 2 | 624 | 1.98 | 1.47 | -670 | -1.97 | -1.46 | 3715 | 12775 | -1.07 | 1.22 | -1.31 | 33.99 | 130.34 |
| 5 | 1 | 645 | 2.63 | 1.95 | -722 | -2.63 | -1.95 | 5477 | 18252 | | 1.26 | -1.42 | 46.62 | 176.96 |
| | 2 | 670 | 2.64 | 1.95 | -731 | -2.63 | -1.95 | 5621 | 23873 | -1.09 | 1.31 | -1.43 | 46.62 | 223.58 |
| 6 | 1 | 691 | 3.52 | 2.61 | -792 | -3.52 | -2.60 | 8250 | 32123 | | 1.35 | -1.55 | 63.66 | 287.24 |
| | 2 | 722 | 3.52 | 2.61 | -805 | -3.52 | -2.60 | 8496 | 40619 | -1.11 | 1.42 | -1.58 | 63.67 | 350.90 |
| 7 | 1 | 743 | 4.43 | 3.28 | -871 | -4.42 | -3.28 | 11493 | 52112 | | 1.46 | -1.71 | 81.08 | 431.98 |
| | 2 | 770 | 4.43 | 3.28 | | | | 5420 | 57532 | | | | 38.56 | 470.55 |

Table 3.7
Parameters calculated for test 4

| Step | Cycle | Tension, maximum | | | Compression, maximum | | | Energy Dissipation, kip-in | | β | ω | $\beta\omega$ | μ | η |
|------|-------|------------------|--------|----------------|----------------------|--------|----------------|----------------------------|------------|---------|----------|---------------|-------|--------|
| | | F, kips | D, in. | ϵ , % | F, kips | D, in. | ϵ , % | Per cycle | Cumulative | | | | | |
| 1 | 1 | 744 | 0.24 | 0.19 | -748 | -0.25 | -0.20 | 75 | 75 | | 0.98 | -0.99 | 0.59 | 0.59 |
| | 2 | 727 | 0.23 | 0.18 | -717 | -0.24 | -0.20 | 42 | 117 | -0.99 | 0.96 | -0.95 | 0.44 | 1.02 |
| 2 | 1 | 847 | 0.73 | 0.60 | -852 | -0.72 | -0.59 | 1183 | 1299 | | 1.12 | -1.13 | 9.88 | 10.90 |
| | 2 | 792 | 0.73 | 0.60 | -834 | -0.72 | -0.59 | 1391 | 2690 | -1.05 | 1.05 | -1.10 | 9.87 | 20.77 |
| 3 | 1 | 855 | 1.48 | 1.21 | -995 | -1.47 | -1.20 | 3264 | 5954 | | 1.13 | -1.32 | 24.17 | 44.94 |
| | 2 | 928 | 1.48 | 1.21 | -1014 | -1.47 | -1.20 | 3940 | 9894 | -1.09 | 1.23 | -1.34 | 24.15 | 69.09 |
| 4 | 1 | 975 | 2.23 | 1.81 | -1115 | -2.22 | -1.81 | 6211 | 16105 | | 1.29 | -1.47 | 38.40 | 107.49 |
| | 2 | 1012 | 2.23 | 1.81 | -1129 | -2.22 | -1.80 | 7037 | 23142 | -1.12 | 1.34 | -1.49 | 38.38 | 145.87 |
| 5 | 1 | 1042 | 2.98 | 2.42 | -1220 | -2.97 | -2.41 | 9564 | 32706 | | 1.38 | -1.61 | 52.61 | 198.48 |
| | 2 | 1077 | 2.98 | 2.42 | -1239 | -2.97 | -2.41 | 10472 | 43177 | -1.15 | 1.42 | -1.64 | 52.62 | 251.10 |
| 6 | 1 | 1107 | 3.72 | 3.03 | -1331 | -3.71 | -3.02 | 13256 | 56433 | | 1.46 | -1.76 | 66.83 | 317.93 |
| | 2 | 1128 | 3.72 | 3.03 | -1358 | -3.72 | -3.02 | 14172 | 70605 | -1.20 | 1.49 | -1.79 | 66.87 | 384.80 |
| 7 | 1 | 1151 | 4.48 | 3.64 | -1245 | -1.48 | -1.20 | 13118 | 83723 | | 1.52 | -1.65 | 52.76 | 437.56 |

Table 3.8
Parameters calculated for test 5

| Step | Cycle | Tension, maximum | | | Compression, maximum | | | Energy Dissipation, kip-in | | β | ω | $\beta\omega$ | μ | η |
|------|-------|------------------|--------|----------------|----------------------|--------|----------------|----------------------------|------------|---------|----------|---------------|-------|--------|
| | | F, kips | D, in. | ϵ , % | F, kips | D, in. | ϵ , % | Per cycle | Cumulative | | | | | |
| 1 | 1 | 476 | 0.33 | 0.21 | -513 | -0.34 | -0.22 | 229 | 229 | | 1.17 | -1.26 | 2.34 | 2.34 |
| | 2 | 453 | 0.34 | 0.22 | -498 | -0.34 | -0.22 | 239 | 468 | -1.10 | 1.11 | -1.22 | 2.42 | 4.76 |
| 2 | 1 | 465 | 0.81 | 0.53 | -514 | -0.81 | -0.53 | 1061 | 1528 | | 1.14 | -1.26 | 11.46 | 16.22 |
| | 2 | 459 | 0.81 | 0.53 | -514 | -0.81 | -0.53 | 1032 | 2561 | -1.12 | 1.12 | -1.26 | 11.44 | 27.66 |
| 3 | 1 | 491 | 1.63 | 1.07 | -605 | -1.63 | -1.07 | 1032 | 3593 | | 1.20 | -1.48 | 27.10 | 54.76 |
| | 2 | 536 | 1.63 | 1.07 | -603 | -1.63 | -1.06 | 2676 | 6269 | -1.13 | 1.31 | -1.48 | 27.08 | 81.84 |
| 4 | 1 | 556 | 2.45 | 1.60 | -669 | -2.45 | -1.60 | 2746 | 9015 | | 1.36 | -1.64 | 42.68 | 124.52 |
| | 2 | 561 | 2.46 | 1.60 | -669 | -2.45 | -1.60 | 4667 | 13682 | -1.19 | 1.38 | -1.64 | 42.68 | 167.20 |
| 5 | 1 | 567 | 3.28 | 2.14 | -735 | -3.27 | -2.14 | 4710 | 18392 | | 1.39 | -1.80 | 58.41 | 225.61 |
| | 2 | 594 | 3.28 | 2.14 | -744 | -3.27 | -2.14 | 6785 | 25177 | -1.25 | 1.46 | -1.82 | 58.42 | 284.03 |
| 6 | 1 | 611 | 4.10 | 2.68 | -795 | -4.09 | -2.67 | 6944 | 32121 | | 1.50 | -1.95 | 73.95 | 357.98 |
| | 2 | 641 | 4.10 | 2.68 | -802 | -4.09 | -2.67 | 9193 | 41314 | -1.25 | 1.57 | -1.96 | 73.95 | 431.93 |
| 7 | 1 | 656 | 4.91 | 3.21 | -862 | -4.90 | -3.21 | 11588 | 52901 | | 1.61 | -2.11 | 89.48 | 521.41 |

Table 3.9
Parameters calculated for test 6

| Step | Cycle | Tension, maximum | | | Compression, maximum | | | Energy Dissipation, kip-in | | β | ω | $\beta\omega$ | μ | η |
|------|-------|------------------|--------|----------------|----------------------|--------|----------------|----------------------------|------------|---------|----------|---------------|-------|--------|
| | | F, kips | D, in. | ϵ , % | F, kips | D, in. | ϵ , % | Per cycle | Cumulative | | | | | |
| 1 | 1 | 370 | 0.33 | 0.21 | -339 | -0.34 | -0.22 | 160 | 160 | | 1.17 | -1.07 | 1.46 | 1.46 |
| | 2 | 348 | 0.34 | 0.22 | -320 | -0.34 | -0.21 | 166 | 326 | -0.92 | 1.10 | -1.01 | 1.51 | 2.97 |
| 2 | 1 | 357 | 0.86 | 0.55 | -345 | -0.85 | -0.54 | 798 | 1125 | | 1.13 | -1.09 | 9.96 | 12.93 |
| | 2 | 360 | 0.86 | 0.55 | -336 | -0.85 | -0.54 | 775 | 1900 | -0.94 | 1.14 | -1.06 | 9.95 | 22.88 |
| 3 | 1 | 383 | 1.72 | 1.10 | -401 | -1.71 | -1.09 | 1993 | 3893 | | 1.21 | -1.27 | 24.00 | 46.88 |
| | 2 | 409 | 1.72 | 1.09 | -411 | -1.71 | -1.09 | 2069 | 5962 | -1.00 | 1.29 | -1.30 | 23.99 | 70.87 |
| 4 | 1 | 427 | 2.59 | 1.65 | -459 | -2.58 | -1.64 | 3535 | 9497 | | 1.35 | -1.45 | 38.17 | 109.05 |
| | 2 | 440 | 2.59 | 1.65 | -474 | -2.58 | -1.64 | 3628 | 13124 | -1.08 | 1.39 | -1.50 | 38.17 | 147.21 |
| 5 | 1 | 454 | 3.44 | 2.19 | -532 | -3.44 | -2.19 | 5337 | 18462 | | 1.44 | -1.68 | 52.18 | 199.39 |
| | 2 | 472 | 3.44 | 2.19 | -558 | -3.44 | -2.19 | 5571 | 24033 | -1.18 | 1.49 | -1.77 | 52.14 | 251.53 |
| 6 | 1 | 492 | 4.53 | 2.88 | -643 | -4.52 | -2.88 | 8209 | 32242 | | 1.55 | -2.03 | 69.90 | 321.43 |
| | 2 | 525 | 4.53 | 2.89 | -627 | -4.52 | -2.88 | 8376 | 40617 | -1.19 | 1.66 | -1.98 | 69.90 | 391.34 |
| 7 | 1 | 527 | 5.18 | 3.30 | -657 | -5.17 | -3.29 | 8946 | 49564 | | 1.67 | -2.08 | 80.44 | 471.78 |

Table 3.10
Parameters calculated for test 7

| Step | Cycle | Tension, maximum | | | Compression, maximum | | | Energy Dissipation, kip-in | | β | ω | $\beta\omega$ | μ | η |
|------|-------|------------------|--------|----------------|----------------------|--------|----------------|----------------------------|------------|---------|----------|---------------|-------|--------|
| | | F, kips | D, in. | ϵ , % | F, kips | D, in. | ϵ , % | Per cycle | Cumulative | | | | | |
| 1 | 1 | 217 | 0.29 | 0.18 | -333 | -0.37 | -0.24 | 129 | 129 | | 0.69 | -1.05 | 1.38 | 1.38 |
| | 2 | 253 | 0.31 | 0.20 | -325 | -0.37 | -0.23 | 139 | 268 | -1.28 | 0.80 | -1.03 | 1.51 | 2.88 |
| 2 | 1 | 303 | 0.83 | 0.53 | -355 | -0.88 | -0.56 | 708 | 976 | | 0.96 | -1.12 | 9.96 | 12.84 |
| | 2 | 326 | 0.83 | 0.53 | -359 | -0.88 | -0.56 | 733 | 1709 | -1.10 | 1.03 | -1.14 | 9.96 | 22.79 |
| 3 | 1 | 353 | 1.69 | 1.08 | -404 | -1.74 | -1.11 | 1939 | 3647 | | 1.12 | -1.28 | 24.02 | 46.81 |
| | 2 | 378 | 1.69 | 1.08 | -410 | -1.74 | -1.11 | 2008 | 5655 | -1.08 | 1.20 | -1.30 | 24.01 | 70.83 |
| 4 | 1 | 396 | 2.56 | 1.63 | -452 | -2.61 | -1.66 | 3422 | 9077 | | 1.25 | -1.43 | 38.18 | 109.01 |
| | 2 | 413 | 2.56 | 1.63 | -466 | -2.61 | -1.66 | 3539 | 12616 | -1.13 | 1.31 | -1.47 | 38.19 | 147.19 |
| 5 | 1 | 430 | 3.41 | 2.17 | -508 | -3.47 | -2.21 | 5196 | 17812 | | 1.36 | -1.61 | 52.16 | 199.35 |
| | 2 | 450 | 3.41 | 2.17 | -520 | -3.47 | -2.21 | 5363 | 23175 | -1.15 | 1.42 | -1.64 | 52.17 | 251.52 |
| 6 | 1 | 465 | 4.50 | 2.87 | -564 | -4.55 | -2.90 | 7703 | 30878 | | 1.47 | -1.78 | 69.89 | 321.41 |
| | 2 | 486 | 4.50 | 2.87 | -604 | -4.55 | -2.90 | 8101 | 38979 | -1.24 | 1.54 | -1.91 | 69.91 | 391.32 |
| 7 | 1 | 508 | 3.46 | 2.20 | | | | 1675 | 40654 | | 1.61 | | 24.21 | 415.53 |

Table 3.11
Parameters calculated for test 8

| Step | Cycle | Tension, maximum | | | Compression, maximum | | | Energy Dissipation, kip-in | | β | ω | $\beta\omega$ | μ | η |
|------|-------|------------------|--------|----------------|----------------------|--------|----------------|----------------------------|------------|---------|----------|---------------|-------|--------|
| | | F, kips | D, in. | ϵ , % | F, kips | D, in. | ϵ , % | Per cycle | Cumulative | | | | | |
| 1 | 1 | 301 | 0.33 | 0.21 | -327 | -0.34 | -0.22 | 137 | 137 | | 0.95 | -1.04 | 1.47 | 1.47 |
| | 2 | 291 | 0.34 | 0.22 | -320 | -0.34 | -0.21 | 146 | 282 | -1.10 | 0.92 | -1.01 | 1.51 | 2.98 |
| 2 | 1 | 296 | 0.86 | 0.55 | -324 | -0.85 | -0.54 | 713 | 996 | | 0.94 | -1.02 | 9.96 | 12.94 |
| | 2 | 290 | 0.86 | 0.55 | -331 | -0.85 | -0.54 | 696 | 1692 | -1.14 | 0.92 | -1.05 | 9.96 | 22.90 |
| 3 | 1 | 323 | 1.72 | 1.09 | -386 | -1.71 | -1.09 | 1821 | 3513 | | 1.02 | -1.22 | 24.00 | 46.90 |
| | 2 | 350 | 1.72 | 1.09 | -401 | -1.71 | -1.09 | 1912 | 5425 | -1.14 | 1.11 | -1.27 | 24.01 | 70.91 |
| 4 | 1 | 366 | 2.59 | 1.65 | -435 | -2.58 | -1.64 | 3270 | 8695 | | 1.16 | -1.38 | 38.16 | 109.07 |
| | 2 | 383 | 2.59 | 1.65 | -449 | -2.58 | -1.64 | 3373 | 12068 | -1.17 | 1.21 | -1.42 | 38.18 | 147.25 |
| 5 | 1 | 396 | 3.44 | 2.19 | -485 | -3.44 | -2.19 | 4902 | 16970 | | 1.25 | -1.53 | 52.16 | 199.41 |
| | 2 | 413 | 3.44 | 2.19 | -509 | -3.44 | -2.19 | 5089 | 22059 | -1.23 | 1.31 | -1.61 | 52.16 | 251.57 |
| 6 | 1 | 428 | 4.53 | 2.88 | -5608 | -4.53 | -2.88 | 7330 | 29388 | | 1.35 | -1.77 | 69.91 | 321.48 |
| | 2 | 448 | 4.53 | 2.89 | -545 | -4.52 | -2.88 | 5741 | 35130 | -1.22 | 1.42 | -1.72 | 69.92 | 391.40 |

Table 3.12
Parameters calculated for test 9

| Step | Cycle | Tension, maximum | | | Compression, maximum | | | Energy Dissipation, kip-in | | β | ω | $\beta\omega$ | μ | η |
|------|-------|------------------|--------|----------------|----------------------|--------|----------------|----------------------------|------------|---------|----------|---------------|-------|--------|
| | | F, kips | D, in. | ϵ , % | F, kips | D, in. | ϵ , % | Per cycle | Cumulative | | | | | |
| 1 | 1 | 439 | 0.33 | 0.22 | -480 | -0.34 | -0.22 | 243 | 243 | | 1.08 | -1.18 | 2.41 | 2.41 |
| | 2 | 427 | 0.34 | 0.22 | -450 | -0.34 | -0.22 | 254 | 497 | -1.05 | 1.05 | -1.10 | 2.48 | 4.89 |
| 2 | 1 | 424 | 0.82 | 0.53 | -479 | -0.81 | -0.53 | 998 | 1496 | | 1.04 | -1.18 | 11.50 | 16.39 |
| | 2 | 454 | 0.82 | 0.53 | -482 | -0.81 | -0.53 | 1007 | 2503 | -1.06 | 1.11 | -1.18 | 11.49 | 27.88 |
| 3 | 1 | 450 | 1.64 | 1.07 | -517 | -1.63 | -1.07 | 2442 | 4945 | | 1.10 | -1.27 | 27.13 | 55.01 |
| | 2 | 492 | 1.64 | 1.07 | -528 | -1.63 | -1.07 | 2501 | 7446 | -1.07 | 1.21 | -1.29 | 27.10 | 82.11 |
| 4 | 1 | 511 | 2.45 | 1.60 | -570 | -2.45 | -1.60 | 4181 | 11627 | | 1.25 | -1.40 | 42.70 | 124.80 |
| | 2 | 527 | 2.45 | 1.60 | -589 | -2.45 | -1.60 | 4268 | 15895 | -1.12 | 1.29 | -1.44 | 42.68 | 167.49 |
| 5 | 1 | 545 | 3.28 | 2.14 | -641 | -3.27 | -2.14 | 6211 | 22107 | | 1.34 | -1.57 | 58.42 | 225.91 |
| | 2 | 565 | 3.28 | 2.14 | -662 | -3.27 | -2.14 | 6422 | 28529 | -1.17 | 1.38 | -1.62 | 58.43 | 284.34 |
| 6 | 1 | 581 | 4.10 | 2.68 | -723 | -4.09 | -2.67 | 8633 | 37162 | | 1.42 | -1.77 | 73.98 | 358.32 |
| | 2 | 604 | 4.10 | 2.68 | -771 | -4.09 | -2.67 | 8967 | 46129 | -1.28 | 1.48 | -1.89 | 73.98 | 432.30 |
| 7 | 1 | 628 | 4.91 | 3.21 | -856 | -4.91 | -3.21 | 11576 | 57705 | | 1.54 | -2.10 | 89.51 | 521.81 |
| | 2 | 656 | 4.91 | 3.21 | -613 | -4.90 | -3.20 | 8020 | 65725 | -0.94 | 1.61 | -1.50 | 89.45 | 611.26 |

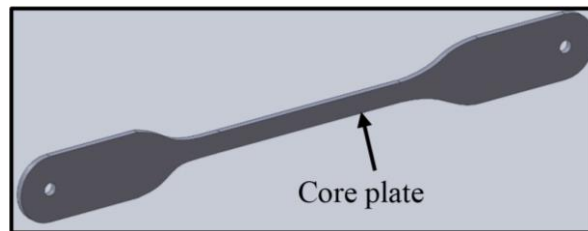


Figure 3.1 Core plates and connection plates in old BRBs

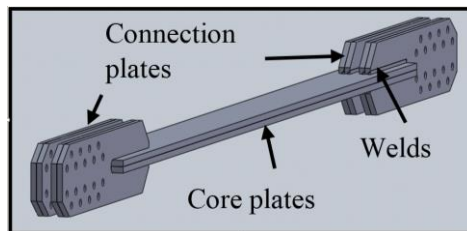


Figure 3.2 Connection plates and the core plates for new BRBs

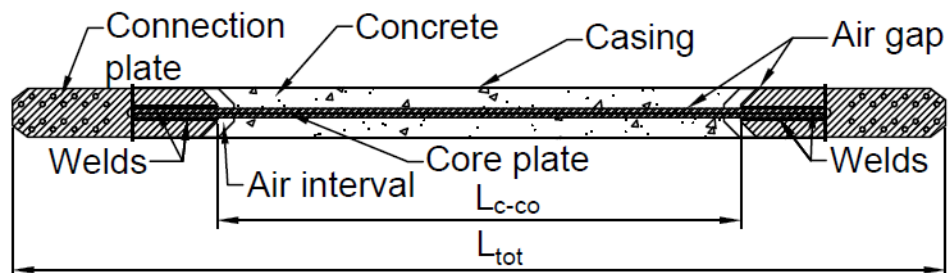


Figure 3.3 Parts of the BRB

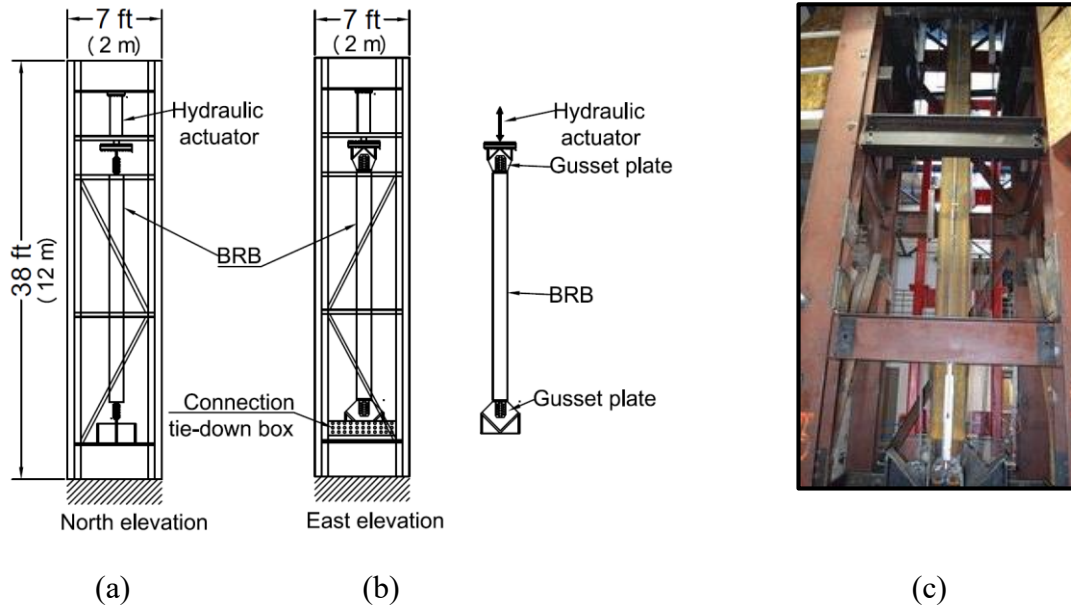


Figure 3.4 Test frame, (a) Side view, (b) Front view of frame and a BRB and (c) Photo of testing frame

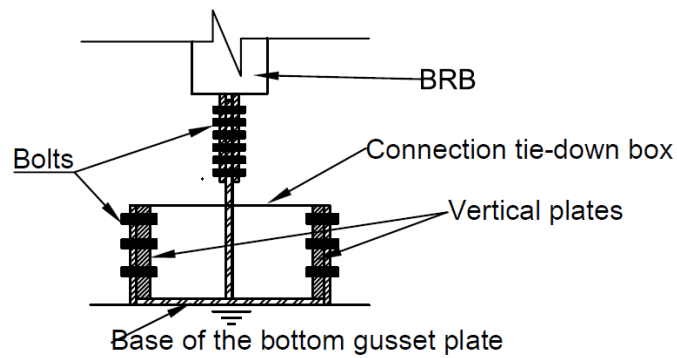


Figure 3.5 Connection details at the bottom of the BRB

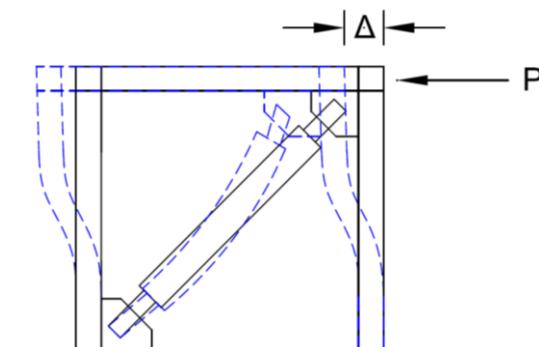


Figure 3.6 Buckling-restrained braced frame

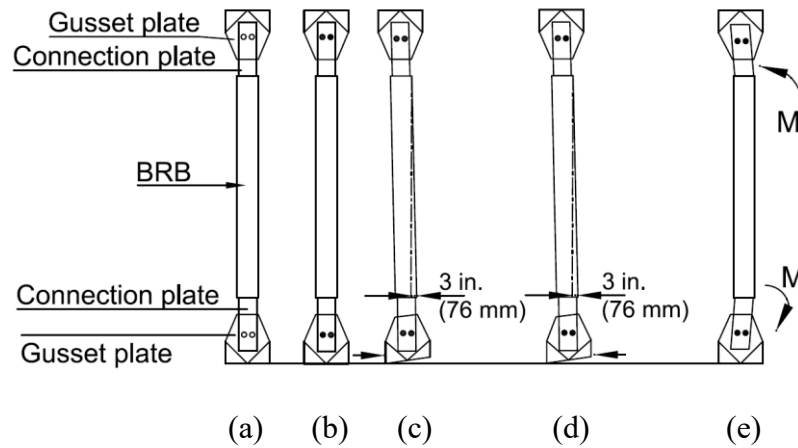


Figure 3.7 Procedure to assemble the BRB to the gusset plate, (a) The BRB is set up vertically, (b) Bolts are inserted into bolt holes, (c) Bottom gusset plate is moved to 3 in. off the vertical axis, (d) Bolts are tightened, then bottom gusset plate is moved back to vertical axis and (e) Moments are created on both ends of BRB

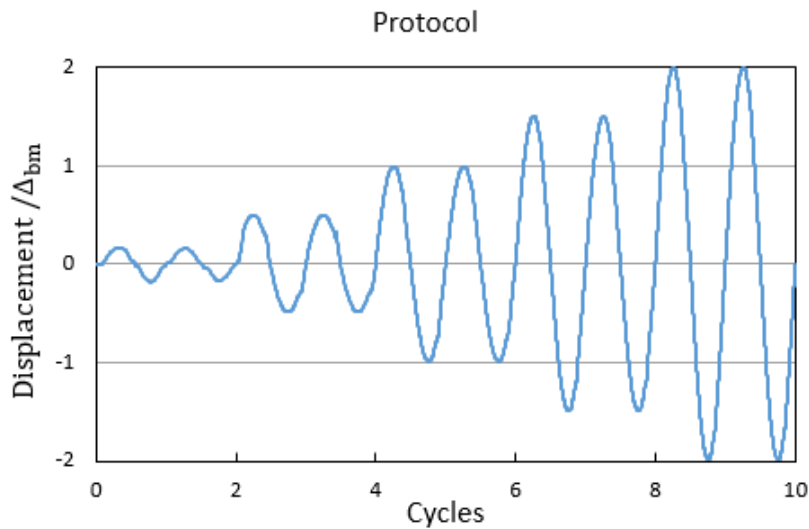


Figure 3.8 Cyclic loading protocol for the tests (Δ_{bm} is the BRB displacement at 1% inter-story drift)



(a)

(b)

(c)

(d)



(e)

(f)

(g)

(h)

(i)

Figure 3.9 Phenomena observed in the tests: (a) Test 1: strong-axis buckling, (b) Test 2: fracture on the core, (c) Test 3: weak-axis buckling, (d) Test 4: out-of-plane buckling on the top gusset plate, (e) Test 5: strong-axis buckling (f) Test 6: combination of strong- and weak-axis buckling, (g) Test 7: weak-axis buckling, (h) Test 8: combination of strong- and weak-axis buckling and (i) Test 9: weak-axis buckling

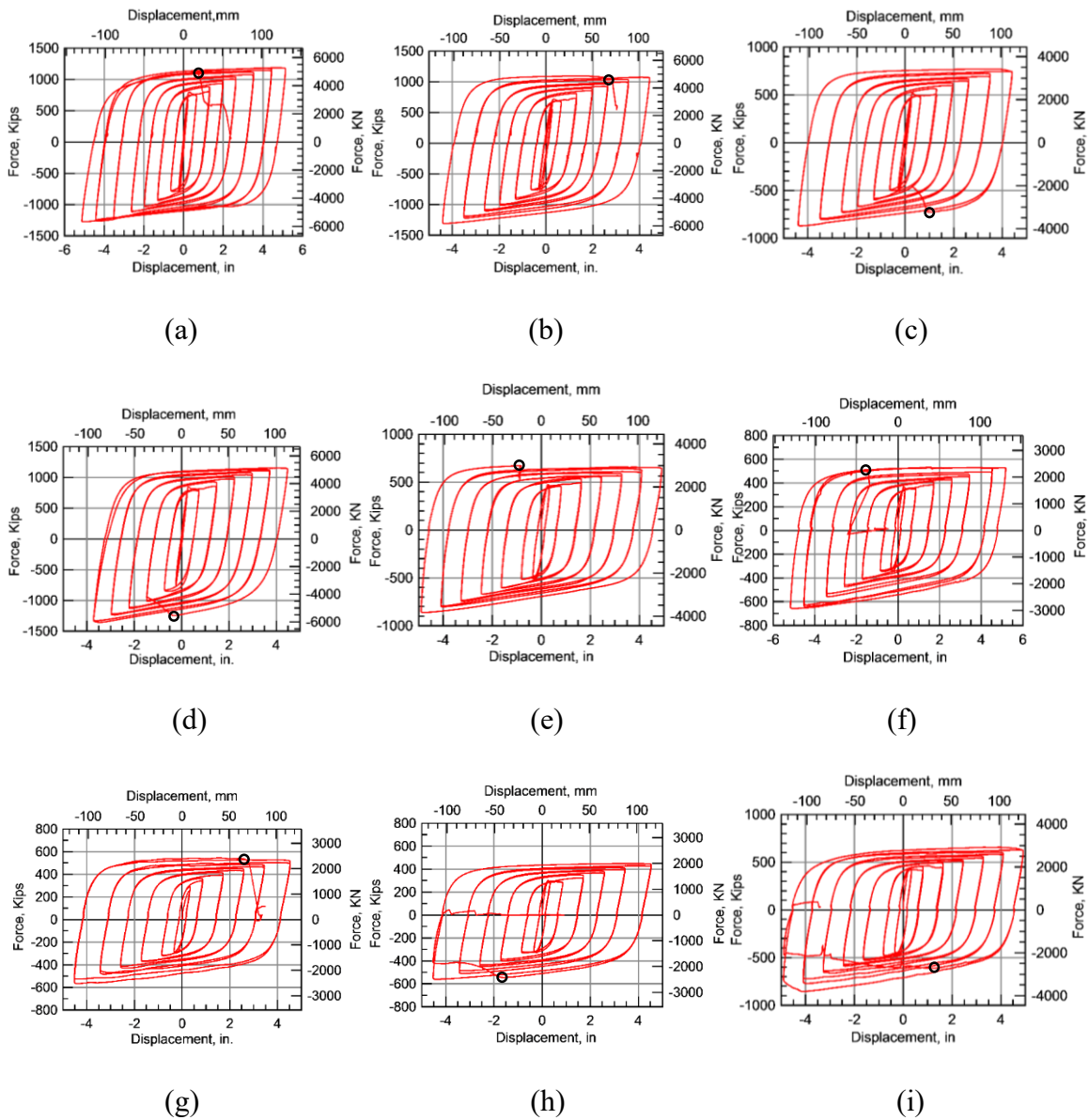


Figure 3.10 Hysteretic loops for all the tests (the moment when the BRB started to fail was circled in the figures): (a) Test 1, (b) Test 2, (c) Test 3, (d) Test 4, (e) Test 5, (f) Test 6, (g) Test 7, (h) Test 8 and (i) Test 9

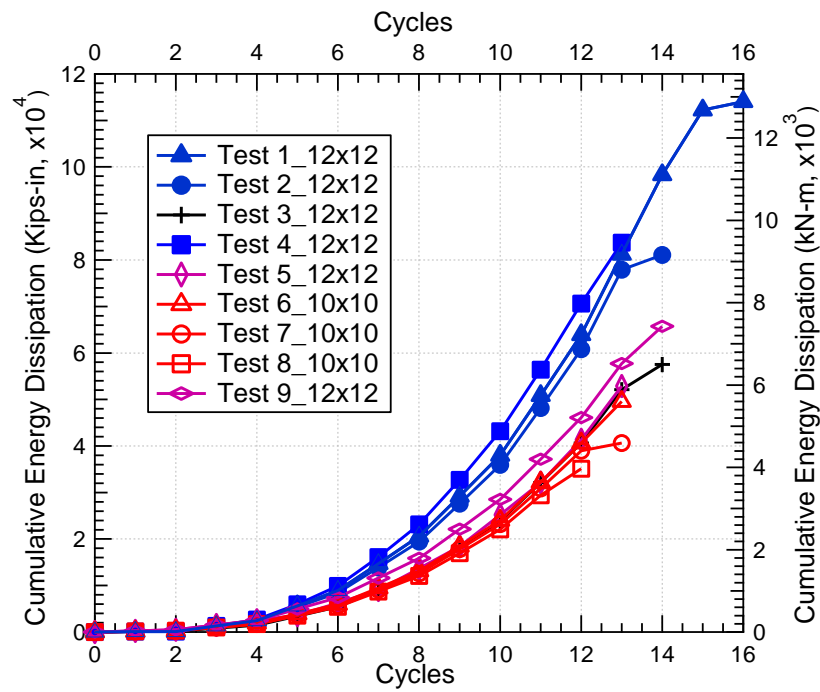


Figure 3.11 Cumulative dissipated energy for nine BRB tests

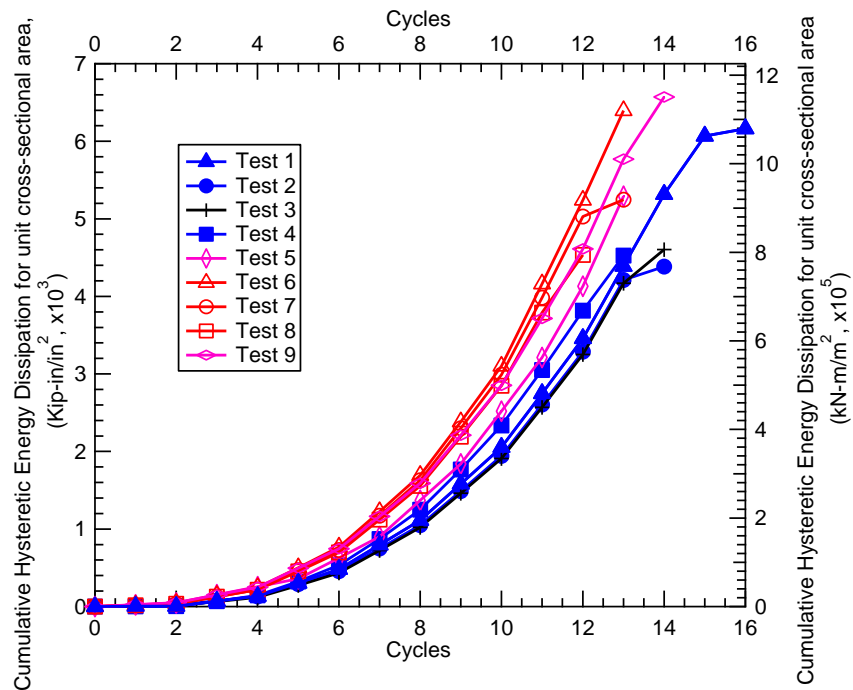


Figure 3.12 Cumulative energy dissipation for unit cross-sectional area of core plates

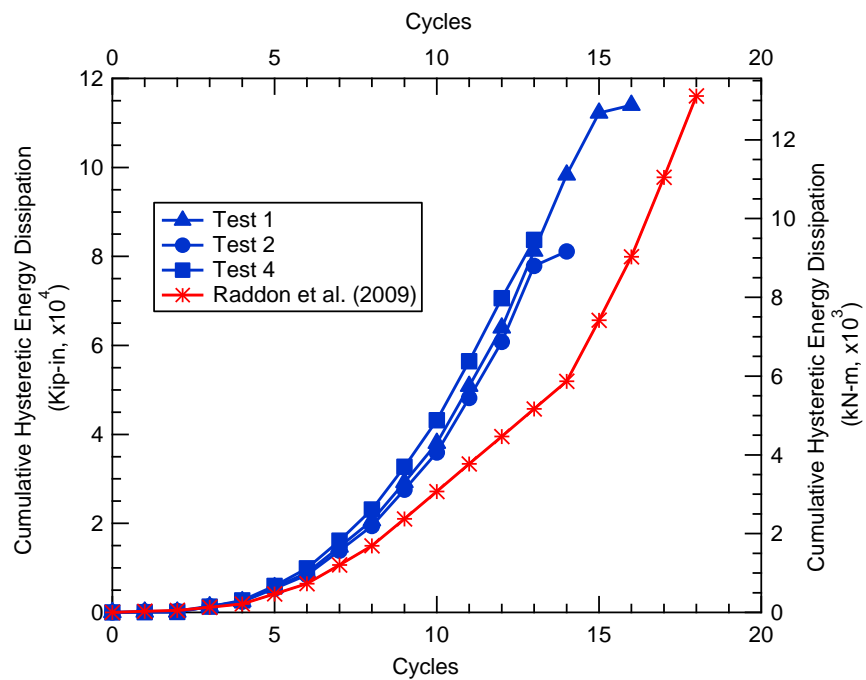


Figure 3.13 Comparison of cumulative energy dissipation for present tests and current generation BRB tested by Raddon et al. (Raddon, B., Pantelides, C., and Reaveley, L.)

CHAPTER 4

BUCKLING FORCE ON THE CORE FOR STRONG-AXIS BUCKLING

An equation for the buckling force on the single or dual core plates in the strong axis will be derived in this portion of the investigation, as well as the contact force between the core plate and the restrainer (concrete and steel casing). The axial compressive buckling force from the closed-form equation derivation will be verified with finite element simulation results, and the backbone curve obtained from the tests.

4.1 Core Buckling Force Derivation

According to the phenomena observed in test 1, shown in Figure 3.9, the core plate had a series of very small waves before the large buckling happened on it. The buckling force which caused the small buckling waves will be derived in this section.

The debonding layers between core plates and the surrounding concrete are made of a soft material, compared to the concrete and steel core; this allows the core plate to deform in the transverse direction when it is subjected to axial compression, without cracking or crushing the concrete. Therefore, the core plate can buckle about either the core plate weak axis or strong axis subjected to the axial compression. The contact force, between the core plates and concrete, is developed when the core plate pushes into the debonding layer. The number of buckling waves will increase when the axial compressive

force increases. The number of waves can be determined by using Eq. (2.4) obtained by Wu et al. (2014).

4.1.1 Assumptions of Equation Derivation

In order to derive the equation for the axial compressive buckling force on the core plate, the following assumptions will be made based on the real restraining conditions:

- (1) Bending deformations of the concrete and casing (restrainer) are ignored. Two kinds of cross-section of steel casing were used for the experiment: 10 in. \times 10 in. \times 0.25 in. and 12 in. \times 12 in. \times 0.25 in. The cross-sectional dimension of the core plates used in the specimens are 9.25 in. \times 2 in., 6.25 in. \times 2 in., 10 in. \times 1 in., and 7.75 in. \times 1 in. For a new BRB cross-section, the cross-section of the restrainer is the cross-section of BRB when the cross-section of the core plates is subtracted. It is obvious that the restrainer has a larger cross-sectional area compared to the core plates, and is stiffer; compared to the restrainer, the core plates are very flexible. Therefore, the deformation on the restrainer caused from the contact force is very small and can be ignored.
- (2) The rotational angle on both ends of core plate about weak axis is zero. For new-generation BRBs, the connection plates significantly increase the stiffness of BRB at ends of core plate to make the end section much stiffer than the middle section of the core plates. Therefore, even though core plates deform in the middle section, the ends of the core plates had very small rotation according to phenomena observed from tests, which can be ignored.
- (3) Both ends of the core plates always stay on the same side of the restrainer

- when the core plates buckle in the same direction. The core plates are originally parallel to the restrainer before loading; when loading starts, the core plates deform and even reach the restrainer under compressive load. Once the contact force between the core plates and the restrainer occurs, it pushes both ends of the core plates to approach the same side of the restrainer.
- (4) In the case of dual core, each plate shares the axial load equally. When the BRB has two core plates, the core plates always have the same dimension and the same material property. Therefore, those two plates share the axial load equally.
- (5) In the case of dual core, two core plates do not move relative to each other. According to the observation made in the experiments, dual core plates always deformed in the same direction, either buckling about the strong axis or the weak axis. The focus in this research is for the case in which the core plates do not move relative to each other.
- (6) The section of the BRB which has a connection plate will not be considered. The connection plate perpendicular to the core plates at the ends of the BRBs can significantly increase the BRB stiffness. However, in this section, the length of the BRBs considered will be only the part of the BRB between the connection plates; this is conservative.

4.1.2 Determination of Reduced Modulus of Elasticity, E_r

Three theories are usually used for inelastic buckling: tangent-modulus theory, reduced modulus theory (Timoshenko et al. 1961), and Shanley's theory (Shanley 1947). The tangent modulus theory tends to underestimate the strength of compression members, since it uses the tangent modulus once the stress on the concave side exceeds the

proportional limit, while the convex side is still below the elastic limit.

The reduced modulus theory defines a reduced Young's modulus, E_r . For a column with rectangular cross section, the reduced modulus is defined by Eq. (4.1). The reduced-modulus theory tends to overestimate the strength of the column, since it is based on stiffness reversal on the convex side of the column.

$$E_r = \frac{4EE_t}{(\sqrt{E} + \sqrt{E_t})^2} \quad (4.1)$$

where E_r is the reduced modulus of elasticity, E is the modulus of elasticity, and E_t is the tangent modulus.

Both the tangent-modulus theory and the reduced-modulus theory oversimplify the inelastic buckling by using only one tangent modulus. In reality, the tangent modulus depends on the stress, which is a function of the bending moment that varies with the displacement.

Shanley (1947) believes that the critical load of inelastic buckling is a function of transverse displacement. According to Shanley's theory, the critical load is located between the critical load predicted by the tangent-modulus theory (the lower bound) and the reduced-modulus theory (the upper bound).

To simplify the problem in this research, the reduced modulus theory is used. To compensate the overestimation given by the reduced modulus theory, tangent modulus equals 3% of Young's modulus of elasticity.

Substituting the reduced modulus of elasticity, E_t , with 3% of Young's modulus of elasticity, E , in Eq. (4.1), the relationship between E_r and E can be described by Eq. (4.2) as

$$E_r = \frac{4 \times E \times 0.03 \times E}{(\sqrt{E} + \sqrt{0.03E})^2} = 0.0872E \quad (4.2)$$

4.1.3 Equation Development for Axial Compressive Force and Contact Force

Both ends of the core plates are assumed to move towards the middle section of the BRB under the axial compressive force, P' , shown in Figure 4.1(a). As the compressive force increases, and when it reaches the critical force, P_E , the core plates buckle and the top surface of the core plates touches the top restrainer (barely touching, and contact force has not occurred yet) shown in Figure 4.1(b). The critical force, P_E , is defined by the Euler equation, Eq. (4.3). At this critical load, the point contact occurs between the core plates and the restrainer. Once the steel core plates yield, the reduced modulus will be used instead of the Young's modulus of elasticity.

$$P_E = \frac{\pi^2 E_{r-co} I_{co}}{L_{c-co}^2} \quad (4.3)$$

where E_{r-co} is the reduced modulus of elasticity of the core plates; I_{co} is the moment inertia of the core plates; L_{c-co} is the critical length of the core plate, which is the horizontal distance between the connection plates on each end.

As the axial compressive force keeps increasing beyond the critical load, the contact force, F_B , and frictional force, μF_B , begin to increase between the core plate and the restrainer. The frictional force resists the motion of the core plates so it is in a direction opposite to the direction of axial compressive force. The distribution of forces on the core plates at this moment is shown in Figure 4.1(c).

The force equilibrium diagram for the core plates is shown in Figure 4.2. When $x \leq l_{sk}/2$ (L_{sk} is the wave length for strong-axis buckling), the moment equilibrium equation for the core plate is expressed in Eq. (4.4). Since the forces are symmetric with respect to the center of the wave, the moment equilibrium equation for the other half of the wave is the same as Eq. (4.4). This is the basic equation for the following axial

compressive force and contact force derivation:

$$(P_k - \mu F_{Bk})y - F_{Bk}x + E_{r-co}I_{co} \frac{d^2y}{dx^2} = 0 \quad (4.4)$$

where P_k is the axial compressive force on the core plates after the core plates buckle, μ is the friction coefficient, E_{r-co} reduced modulus of the core plate, x is the horizontal distance, y is the vertical distance, F_{Bk} is the contact force between the concrete and steel core plates, and I_{co} is the moment of the inertia of the core plates.

As the increase of the axial compressive force after the first wave shows, the second wave will occur, then the third wave and so on. The axial compressive forces, P_k , and the contact forces, F_{Bk} , for one up to four waves on the core plate will be derived in the following section, as well as the general equations for the axial compressive force, P_k , and the contact force, F_{Bk} .

4.1.3.1 Core Plates with One Wave

For small deformations, y , the bending moment at any point on the curve shown in Figure 4.3 can be expressed in Eq. (4.5). At the point of contraflexure $\frac{d^2y}{dx^2} = 0$, so the moment at that point is zero. Therefore, the bending moment at the point A_1 in Figure 4.3, which is the point of contraflexure, can be expressed in Eq. (4.6). In this case, the buckling wave length, L_{s1} , equals the critical length of the core plate, L_{c-co} , since only one wave occurs.

$$M = E_{r-co}I_{co} \frac{d^2y}{dx^2} \quad (4.5)$$

$$M_{A_1} = P_1e - \mu F_{B1}e - F_{B1} \frac{L_{s1}}{4} \quad (4.6)$$

where E_{r-co} is the reduced modulus of the core plates; I_{co} is the moment of the inertia of the core plates; x and y are the horizontal and vertical distance from point A_1 to the initial

point on the left end, respectively; M_{A_1} is the moment at point A_1 ; P_1 is the axial compressive force on the core plates when only one wave occurs; μ is the frictional coefficient between the concrete and the core plates; F_{B1} is the contact force between the core plates and the concrete when only one wave occurs; $2e$ is the thickness of the deboning material or air gap between concrete and the core plates; and L_{s1} is the wave length of the core plates for strong-axis buckling when only one wave occurs.

Setting $M_{A_1} = 0$ in Eq. (4.6) gives

$$F_{B1} = \frac{4P_1e}{L_{s1} + 4\mu e} \quad (4.7)$$

After the first wave occurs, the axial force on the core plates is the Euler buckling force, P_E . In Figure 4.3, it can be seen the axial force is expressed in terms of $(P_1 - \mu F_{B1})$. Therefore, the force equilibrium can be obtained in Eq. (4.8):

$$P_1 - \mu F_{B1} = P_{E1} \quad (4.8)$$

where P_{E1} is Euler buckling force when only one wave occurs.

Substituting the Euler buckling force Eq. (4.3) into Eq. (4.8), the axial compressive force on the core plates can be expressed in Eq. (4.9) when only one wave occurs.

$$P_1 = \mu F_{B1} + \frac{\pi^2 E_{r-co} I_{co}}{L_{s1}^2} \quad (4.9)$$

The same method to determine contact force and axial compressive force will be used for core plates with more waves.

4.1.3.2 Core Plates with Two Waves

After one wave has formed and the axial compressive force increases, the peak of the first wave will shift to the left and the second will form. The force distribution on the

core plates is shown in Figure 4.4. Since there are two waves in the core plates, the wave length for this case, L_{S2} , will be half of the critical length of the core plates, L_{c-co} .

The bending moment at point A_2 is expressed in Eq. (4.10). The contact force, F_{B2} , between concrete and the core plate for this case is expressed in Eq. (4.11) by setting $M_{A_2} = 0$ in Eq. (4.10). The force equilibrium of the core plates in the axial direction can be expressed in Eq. (4.12). The axial compressive force, P_2 , in the core plates when two waves occur can be obtained in Eq. (4.13) by reorganizing Eq. (4.12).

$$M_{A_2} = 2F_{B2} \frac{L_{S2}}{4} + 2\mu F_{B2}e + P_2e - \mu F_{B2}e - F_{B2} \frac{3L_{S2}}{4} \quad (4.10)$$

$$F_{B2} = \frac{4P_2e}{L_{S2} - 4\mu e} \quad (4.11)$$

$$P_2 - 3\mu F_{B2} = P_{E2} \quad (4.12)$$

$$P_2 = 3\mu F_{B2} + \frac{\pi^2 E_{r-co} I_{co}}{L_{S2}^2} \quad (4.13)$$

where F_{B2} is the contact force between the concrete and the core plates when two waves occur, P_{E2} is the Euler buckling force in the core plates when two waves occur, and L_{S2} is the wave length of the core plates when two waves occur.

4.1.3.3 Core Plates with Three Waves

If the axial compressive force keeps increasing, the third wave forms in the core plate. The wave length, L_{S3} , will be one third of the critical length of the core plates, L_{c-co} . The force distribution in the core is shown in Figure 4.5. Since there are two waves in the core plates, the wave length for this case, L_{S3} , will be one third of the critical length of the core plates, L_{c-co} .

The bending moment at point A_3 is expressed in Eq. (4.14). The contact force, F_{B3} , between concrete and the core plate for this case is expressed in Eq. (4.15) by setting

$M_{A_3} = 0$ in Eq. (4.14). Force equilibrium of the core plates in the axial direction is expressed in Eq. (4.16). The axial compressive force, P_3 , in the core plates when three waves occur can be obtained in Eq. (4.17) by reorganizing Eq. (4.16).

$$M_{A_3} = -F_{B3}\mu e + P_3 e - F_{B3} \frac{5L_{S3}}{4} + 2F_{B3}\mu e + 2F_{B3} \frac{3L_{S3}}{4} - 2F_{B3}\mu e - 2F_{B3} \frac{L_{S3}}{4} \quad (4.14)$$

$$F_{B3} = \frac{4P_3 e}{L_{S3} + 4\mu e} \quad (4.15)$$

$$P_3 - 5\mu F_{B3} = P_{E3} \quad (4.16)$$

$$P_3 = 5\mu F_{B3} + \frac{\pi^2 E_{r-co} I_{co}}{L_{S3}^2} \quad (4.17)$$

where F_{B3} is the contact force between the concrete and the core plates when three waves occur in the core plates, P_{E3} is the Euler buckling force in the core plates when three waves occur, and L_{S3} is the wave length of the core plates when three waves occur.

4.1.3.4 Core Plates with Four Waves

If the axial compressive force keeps increasing, the fourth wave forms in the core plate. The wave length, L_{S4} , will be one fourth of the critical length of the core plates, L_{c-co} . The force distribution in the core is shown in Figure 4.6. The bending moment at point A_4 is expressed in Eq. (4.18). The contact force, F_{B4} , between concrete and the core plate for this case is expressed in Eq. (4.19) by setting $M_{A_4} = 0$ in Eq. (4.18). The force equilibrium of the core plates in the axial direction can be expressed in Eq. (4.20). The axial compressive force, P_4 , in the core plates when four waves occur can be obtained in Eq. (4.21) by reorganizing Eq. (4.20).

$$M_{A_4} = F_{B4}\mu e + F_{B4} \frac{7L_{S4}}{4} - P_4 e - F_{B4} \frac{5L_{S4}}{4} - 2F_{B4}\mu e + 2F_{B4}\mu e + 2F_{B4} \frac{3L_{S4}}{4} - 2F_{B4} \frac{L_{S4}}{4} - 2F_{B4}\mu \quad (4.18)$$

$$F_{B4} = \frac{4P_4 e}{L_{S4} - 4\mu e} \quad (4.19)$$

$$P_4 - 7\mu F_{B4} = P_{E4} \quad (4.20)$$

$$P_4 = 7\mu F_{B4} + \frac{\pi^2 E_{r-co} I_{co}}{L_{s4}^2} \quad (4.21)$$

where F_{B4} is the contact force between the concrete and the core plates when four waves occur in the core plates, P_{E4} is the Euler buckling force in the core plates when four waves occur, and L_{s4} is the wave length of the core plates when four waves occur.

4.1.3.5 General Equation for Contact Force and Axial Compressive Force on the Core Plates

The equations for contact force and axial compressive force on the core plates are shown in Table 4.1, in which the equations derived in the previous sections are listed and the wave number ranges from one to four. The axial compressive force in the core plates for any wave number can be simplified in Eq. (4.22):

$$P_k = (2k - 1)\mu F_{Bk} + \frac{\pi^2 E_{r-co} I_{co}}{L_{sk}^2} \quad (k = 1, 2 \dots n) \quad (4.22)$$

where k is the wave number, which is the ratio of critical length of the core to the wave length (L_{c-co}/L_{sk}); and L_{sk} is the wave length when the core plates have k waves.

The equation for the contact force for the case of even waves is different from that for the case of odd waves. When odd waves occur, the contact force, F_{Bk} , can be expressed in Eq. (4.23), which is summarized from the related equations listed in Table 4.1.

$$F_{Bk} = \frac{4P_{ke}}{L_{sk} + 4\mu e} \quad (k = 1, 3 \dots (2n-1)) \quad (4.23)$$

Substituting Eq. (4.22) into Eq. (4.23), the contact force for odd waves is obtained in Eq. (4.24), which relates to the material property and the geometry of the core plates. Substituting Eq. (4.24) back into Eq. (4.22), the axial compressive force for odd waves

can be expressed in Eq. (4.25).

$$F_{Bk} = \frac{4\pi^2 E_{r-co} I_{co} e}{\left(\frac{L_c-co}{k}\right)^2 \left(\frac{L_c-co}{k} + 8\mu e - 8k\mu e\right)} = 4P_E \left(\frac{L_c-co}{L_{sk}}\right)^2 \left[\frac{1}{\left(\frac{L_{sk}}{e}\right) + 8\mu(1-k)} \right] \quad (k=1, 3 \dots (2n-1)) \quad (4.24)$$

$$P_k = \frac{4\pi^2 E_{r-co} I_{co} e (2k-1)\mu}{\left(\frac{L_c-co}{k}\right)^2 \left(\frac{L_c-co}{k} + 8\mu e - 8k\mu e\right)} + \frac{\pi^2 E_{r-co} I_{co}}{\left(\frac{L_c-co}{k}\right)^2} = P_E \left(\frac{L_c-co}{L_{sk}}\right)^2 \left[1 + \frac{4\mu(2k-1)}{\left(\frac{L_{sk}}{e}\right) + 8\mu(1-k)} \right] \quad (k=1, 3 \dots (2n-1)) \quad (4.25)$$

When core plates buckle in even waves, the contact force, F_{Bk} , can be expressed in the Eq. (4.26), which is summarized from the related equations listed in the Table 4.1.

$$F_{Bk} = \frac{4P_k e}{L_{sk} - 4\mu e} \quad (k=2, 4 \dots 2n) \quad (4.26)$$

Substituting Eq. (4.22) into Eq. (4.26), the contact force for even waves is obtained in Eq. (4.27), which depends on the material property and the geometry of the core plates.

$$F_{Bk} = \frac{4\pi^2 E_{r-co} I_{co} e}{\left(\frac{L_c-co}{k}\right)^2 \left(\frac{L_c-co}{k} - 8k\mu e\right)} = 4P_E \left(\frac{L_c-co}{L_{sk}}\right)^2 \left[\frac{1}{\left(\frac{L_{sk}}{e}\right) + 8\mu k} \right] \quad (k=2, 4, \dots 2n) \quad (4.27)$$

Substituting Eq. (4.27) back into Eq. (4.22), the axial compressive force for odd waves can be expressed in Eq. (4.28):

$$P_k = \frac{4\pi^2 E_{r-co} I_{co} e (2k-1)\mu}{\left(\frac{L_c-co}{k}\right)^2 \left(\frac{L_c-co}{k} - 8k\mu e\right)} + \frac{\pi^2 E_{r-co} I_{co}}{\left(\frac{L_c-co}{k}\right)^2} = P_E \left(\frac{L_c-co}{L_{sk}}\right)^2 \left[1 + \frac{4\mu(2k-1)}{\left[\left(\frac{L_{sk}}{e}\right) + 8\mu k\right]} \right] \quad (k=2, 4, \dots 2n) \quad (4.28)$$

Equations (4.24), (4.25), (4.27), and (4.28) show clearly that the contact force and the postbuckling axial compressive force are a function of the critical force P_E amplified by the ratio $\left(\frac{L_c-co}{L_{sk}}\right)^2$, and the ratio $\frac{L_{sk}}{e}$, in addition to the number of the waves, k , and coefficient of friction, μ .

According to the previous research (Wu et al. 2014), the wave length of the core

plate, L_{sk} , can be calculated by using Eq. (2.4) when strong-axis buckling occurs to the core plate. The wave number, k , can be determined by the ratio of the critical length of the core plate to the wave number (L_{c-co}/L_{sk}).

4.2 Verification with Finite Element Method (FEM) Model of BRBs under Monotonic Axial Compression

The BRBs in tests 1, 5, 6, and 8 had strong-axis buckling after the cyclic loading. These BRBs are divided into three groups according to the cross-sectional dimensions of the core plates. The BRB in test 1 is the model 1, the BRB in test 5 is the model 2, and BRBs in test 6 and 8 are the model 3, which are listed in Table 4.2. These three groups of BRBs under monotonic axial compression will be simulated in a finite element program. The axial compressive forces from the simulation method will be compared with those calculated with the derived equations.

4.2.1 Calculation of Postbuckling Axial Compressive Force Using Derived Equation

Wu et al. (2014) derived the equation for the wave length when the core plates have strong-axis buckling, which is Eq. (2.4) in Chapter 2. The relationship between Young's modulus of elasticity of the core plate, E , and the yielding stress, F_y , is obtained in Eq. (4.29). The wave length of the core plates for strong-axis buckling is about 6.8 times the width of the core plates, which is expressed in Eq. (4.30).

$$\frac{E}{F_y} = \frac{29,000,000}{40900} \approx 709 \quad (4.29)$$

$$L_{sk} = \sqrt{\frac{4\pi^2(EI_s)_{eff}}{P_y}} = \sqrt{\frac{4\pi^2 \times 0.02EI_s}{F_y w_c t_c}} \sqrt{\frac{4\pi^2 \times 0.02 \times 709 \times w_c^3 t_c}{12w_c t_c}} \approx 6.8 w_c \quad (4.30)$$

The critical length of the core plate is 123 in. for test 1 (model 1); the wave

number of the core plate, k , can be determined by the Eq. (4.31).

$$k = \frac{L_{c-co}}{L_{sk}} = \frac{123}{6.8 \times 9.25} = 2 \quad (4.31)$$

Since k equals 2, Eq. (4.28) will be used to calculate the axial compressive force.

$$P_2 = \frac{4\pi^2 E_{r-co} I_{co} e(2k-1)\mu}{\left(\frac{L_{c-co}}{k}\right)^2 \left(\frac{L_{c-co}}{k} - 8k\mu e\right)} + \frac{\pi^2 E_{r-co} I_{co}}{\left(\frac{L_{c-co}}{k}\right)^2} = \frac{4 \times 3.14^2 \times 2528316 \times 123 \times 0.0625 \times (2 \times 2 - 1) \times 0.57}{\left(\frac{123}{2}\right)^2 \times \left(\frac{123}{2} - 8 \times 2 \times 0.57 \times 0.0625\right)} + \frac{3.14^2 \times 2528316 \times 131.9}{\left(\frac{123}{2}\right)^2} = 875 \times 10^3 \text{ lbf} \quad (4.32)$$

The calculations for the upper bound and lower bound of buckling force for models 2 and 3 follow the same rule as model 1. Since models 2 and 3 have no integral wave number, the upper bound of the buckling force is used as one for three waves and the lower bound of the buckling force is used as one for two waves. The buckling forces for these three models are shown in Table 4.2.

4.2.2 Finite Element (FE) Simulation of BRBs with Monotonic Axial Compression

To verify the equation derived in the last section, the finite element simulation method is adopted. The BRB without the connection plate will be simulated in ANSYS software. In the finite element simulation model, BRBs only have core plates, concrete, casing, and air gap around the core plates, which is the same as shown in Figure 4.1 (a). The length of the BRB in the simulation is the total length of the BRB minus the length of the connection plates, which equals the critical length of the core plates.

Element SOLID 186 is used for all the members of the BRB, which is a higher order three-dimensional 20-node solid element that exhibits quadratic displacement behavior. The element TARGE 170 is used to represent various three-dimensional “target” surface for the associated contact elements. The element CONTA 174 is used to

represent contact and sliding between three-dimensional “target” surfaces and a deformable surface, defined by this element. Both elements TARGE 170 and CONTA 174 are used for the air gap. The monotonic axial compressive load is applied on one end of the core plates. The other end of the core plates is fixed, which is the same as the boundary condition of core plates in the tests. Since the stress-strain curve for the core plate in the last section was considered bi-linear, a bi-linear stress-strain curve will be used for the material property of the core plates in the simulation. The normal penalty stiffness factor, FKN, which is used to determine contact stiffness and penetration, is chosen as 0.001 for the convergence, and the friction coefficient for between the concrete and steel core is taken as 0.57.

The BRB model built in Ansys is shown in Figure 4.7. Figure 4.7 (a) is a side view of the BRB along its length. The axial compressive force is applied at the top end of the core plate; the bottom end of the BRB is fixed. Figure 4.7 (b) shows a cross-sectional view of the BRB, in which the core plate is in the middle with the concrete surrounded, and the outside thin layer is the steel casing. The bar-shaped elements are the gap element between the core plates and the concrete.

The displacement-control loading method is used for the finite element simulation. The eccentricity is added to the strong axis of the core plate to help to create strong-axis buckling deformation. The axial displacement and horizontal displacement are applied on every node on the surface of the core plate at the loading end, in order to apply the axial compressive load and the eccentricity. Selection of the ratio of horizontal displacement to the axial displacement, λ , is very critical. If this ratio is too small, strong-axis buckling will not occur in the core plates. If this ratio is too large, the buckling force

obtained will be smaller than the actual value.

Figures 4.8 and 4.9 show the force versus displacement for model 1 with three different λ values, which are 0.05, 0.15, and 0.25. Figure 4.9 shows the von misses stress distribution and deformation of the core plate for the three λ values. From the plot of the force vs. displacement or the deformation of the core plates, the BRB with $\lambda=0.15$ shows clear strong-axis buckling performance. The same method is applied for the other two models: the horizontal displacements for models 1, 2, and 3 are 0.525 in., 0.8 in. and 0.4 in., respectively, as listed in Table 4.3. Strong-axis buckling deformation, wave number, and axial compressive force will be compared for the closed-form equation and finite element simulation. The cross-sectional dimensions for the simulated BRBs are listed in Table 4.3. These three BRBs are the same as those listed in Table 4.2.

The axial compressive force on the core plate vs. the axial displacement for the three models are shown in Figure 4.10. The postbuckling force for each model is marked in red circle and they are 863 kips for model 1, 421.3 kips for model 2, and 322.3 kips for model 3, respectively. The deformations of the core plates in these three models during the FE simulation are shown in Figure 4.11. It can be seen that they all have strong-axis buckling. The wave number for the strong-axis buckling on the core in model 1 is 2, for model 2 it is 1.5, and for model 3 it is 2.

The FE simulation results and the closed-form equation results are listed in Table 4.4, which include the wave number and the postbuckling load. It can be seen that the core buckled at a similar wave number as the calculation results, and the postbuckling forces from the simulation fall within the range obtained from the derived equations. Therefore, the closed-form equation solutions for the postbuckling force on the core

plates for strong-axis buckling are similar to the simulation results.

4.3 Verification of Postbuckling Forces from the Derived Equations with the Backbone Curves Obtained from the Tests

In this section, the postbuckling forces in the core plates, calculated in Section 4.2.1, from the closed-form equations, are compared with the test results. The original test results are plotted using the hysteretic loops. In order to show the elastic zone and plastic zone of the material for the braces, the backbone curves for the test results are used. The backbone curve consists of the maximum force for each loop and the corresponding displacement. The backbone curves for the three models listed in Section 4.2.1 are shown Figure 4.12.

To verify the equations derived in the last section, the closed-form equation buckling forces for the three models are plotted in the same figure with the corresponding backbone curve obtained from the tests shown in Figure 4.12.

The result for test 1 is shown in Figure 4.12 (a). From Figure 3.9 (a), it is seen that the core plate in this test buckled in two waves, which is the same as the calculated wave number. Since buckling occurs after the steel yields, it is expected that the calculated buckling force will exceed the yield postload; however, it is clear that the true postbuckling load is between $k=2$ and $k=3$.

The results for Test 5 are plotted in Figure 4.12 (b). In Figure 3.9 (e), the buckling wave number of the core plate cannot be distinguished very significantly. The reason for this might be that the test did not go far enough to reach the maximum wave number; failure of the BRB was due to another cause, such as connection plates buckling.

Therefore, the ultimate force from the test is lower than the upper bound of the buckling

force calculated with the closed-form equation, which is shown in Figure 4.12 (b).

Since tests 6 and 8 have core plates with the same cross-sectional dimension of 7.75 in. \times 1 in., they get the same result by using the derived equations to calculate the postbuckling force on the core plate. Therefore, both tests 6 and 8 are plotted in Figure 4.12 (c). The calculated wave number for these specimens is 3.0, but it is hard to determine the wave numbers of the core plates from Figure 3.9 (f) and 3.9 (h). The reason for this might be that the specimens had a weak-axis buckling and strong-axis buckling combined failure mode. Since buckling happens after the material yields, it is reasonable for the plastic zone of the material property to fall within the upper bound and the lower bound obtained from the closed-form equation solution.

From Figure 4.12, it can be seen that for all the lower bound solutions, the closed-form equations are lower than the yielding force obtained from the tests. In the BRB tests buckling usually happens after the material yields. This means that the results calculated using the closed-form equations are conservative. This is not surprising because of the assumptions made in the derivation equations, for example, that the section of the BRB which has a connection plate was not considered in the closed-form solution or the FE simulation.

Table 4.1
The contact force and axial compressive force on the core for different waves

| Wave number | Contact force, B | Axial compressive force, P |
|-------------|---|--|
| 1 | $F_{B1} = \frac{4P_1 e}{L_{s1} + 4\mu e}$ | $P_1 = \mu F_{B1} + \frac{\pi^2 E_{r-co} I_{co}}{L_{s1}^2}$ |
| 2 | $F_{B2} = \frac{4P_2 e}{L_{s2} - 4\mu e}$ | $P_2 = 3\mu F_{B2} + \frac{\pi^2 E_{r-co} I_{co}}{L_{s2}^2}$ |
| 3 | $F_{B3} = \frac{4P_3 e}{L_{s3} + 4\mu e}$ | $P_3 = 5\mu F_{B3} + \frac{\pi^2 E_{r-co} I_{co}}{L_{s3}^2}$ |
| 4 | $F_{B4} = \frac{4P_4 e}{L_{s4} - 4\mu e}$ | $P_4 = 7\mu F_{B4} + \frac{\pi^2 E_{r-co} I_{co}}{L_{s4}^2}$ |

Table 4.2
The upper bound and lower bound of the buckling force for three models

| Model # | Core plate size, in. | Test No. | E/F_y | Wave length, in. | Calculated wave number | Actual wave number | Calculated Axial postbuckling load, Kips | |
|---------|----------------------|----------|---------|------------------|------------------------|--------------------|--|-------------|
| | | | | | | | Upper bound | Lower bound |
| 1 | 9.25x2x123 | 1 | 709 | 62.3 | 2.0 | 2 | 1993 | 876 |
| 2 | 10x1x153 | 5 | 709 | 67.4 | 2.2 | - | 903 | 398 |
| 3 | 7.75x1x157 | 6&8 | 709 | 52.2 | 3.0 | - | 421 | 185 |

Table 4.3
Simulation models in Ansys

| Model # | Core plate size, in. | Casing size, in. | Horizontal displacement, in. | λ |
|---------|----------------------|------------------|------------------------------|-----------|
| 1 | 9.25x2x123 | 12x12x0.25 | 0.525 | 0.15 |
| 2 | 10x1x153 | 12x12x0.25 | 0.8 | 0.32 |
| 3 | 7.75x1x157 | 10x10x0.25 | 0.4 | 0.2 |

Table 4.4
Comparison of the simulation results with calculation results

| | Model number | Simulation result | Equation calculation result | |
|-------------------------|--------------|-------------------|-----------------------------|-------------|
| Buckling direction | 1 | Strong | Strong | |
| | 2 | Strong | Strong | |
| | 3 | Strong | Strong | |
| Wave number | 1 | 2 | 2 | |
| | 2 | 1.5 | 2.2 | |
| | 3 | 2 | 3.0 | |
| Axial compressive force | | kips | Upper bound | Lower bound |
| | 1 | 863 | 1993 | 876 |
| | 2 | 421.3 | 903 | 398 |
| | 3 | 322.3 | 421 | 185 |

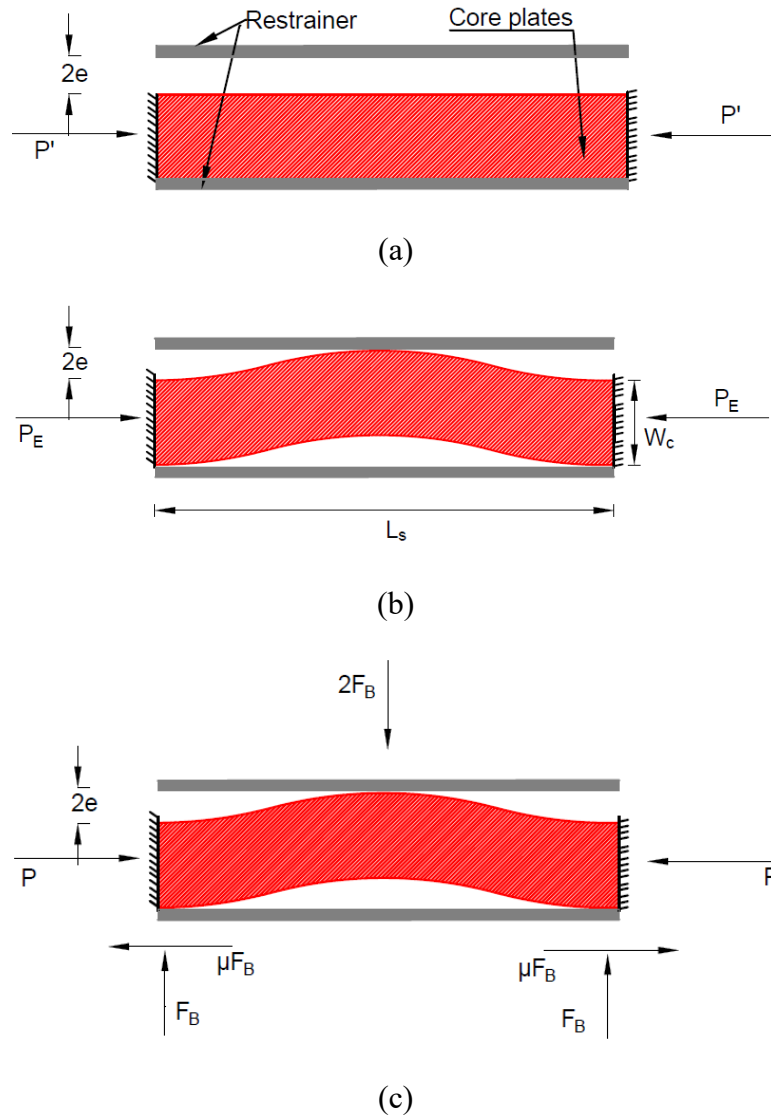


Figure 4.1 Deformation of the core plate under axial compression: (a) The initial status of the core plates, (b) Core plates buckle with axial compressive load and (c) The force on the core plates after they buckle

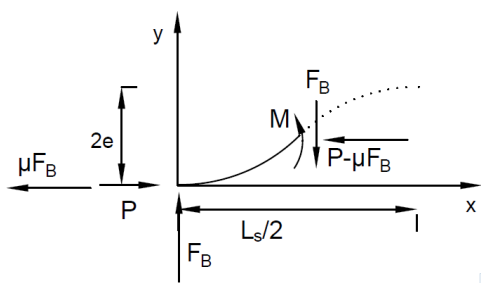


Figure 4.2 Force equilibrium diagram for the top core plate

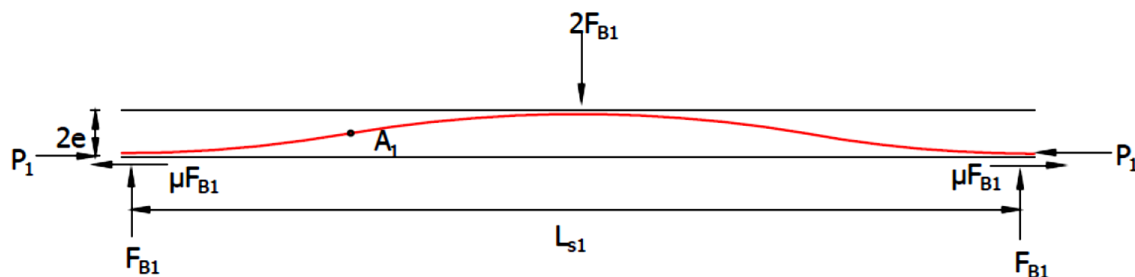


Figure 4.3 Force distribution on the core plate when it has one wave

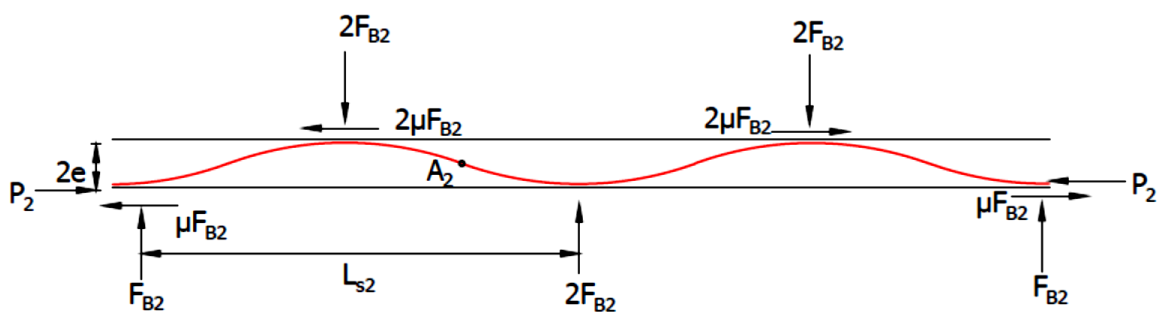


Figure 4.4 Force distribution on the core plate when it has two waves

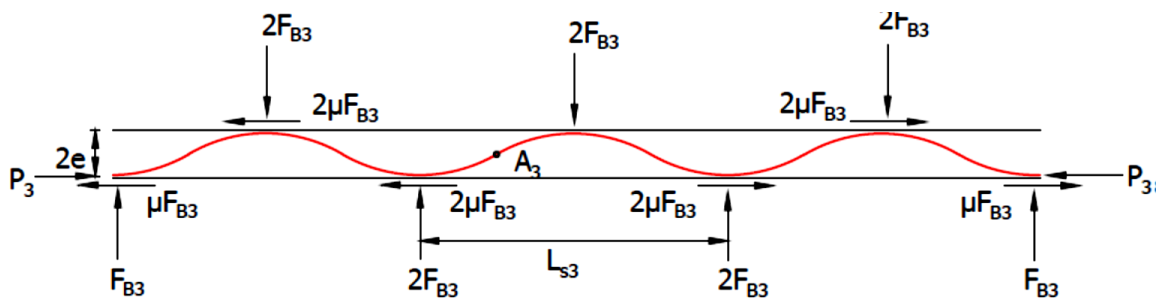


Figure 4.5 Force distribution on the core plates when they have three waves

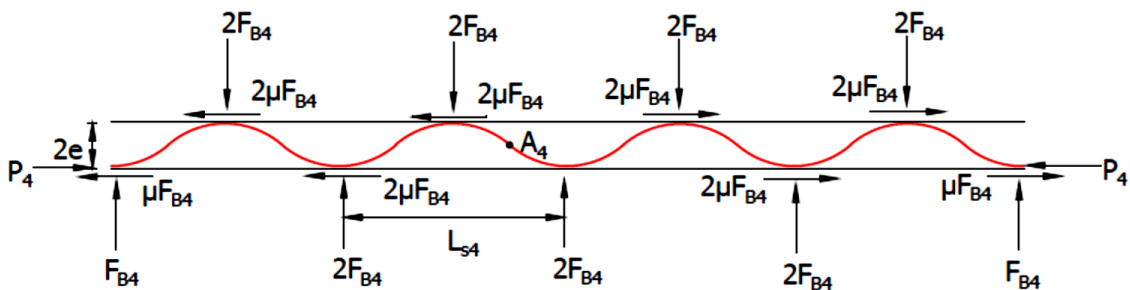


Figure 4.6 Force distribution on the core plates when they have four waves

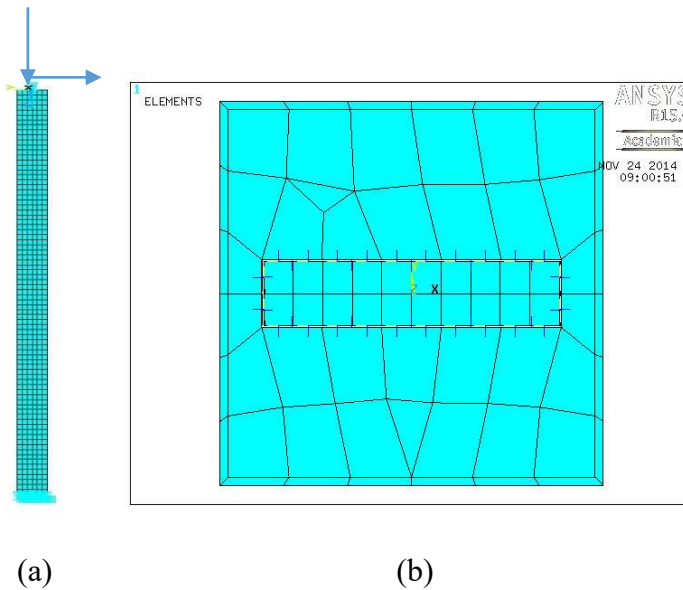


Figure 4.7 BRB model #1 built in Ansys: (a) Side view of the BRB and (b) Cross-section of the BRB

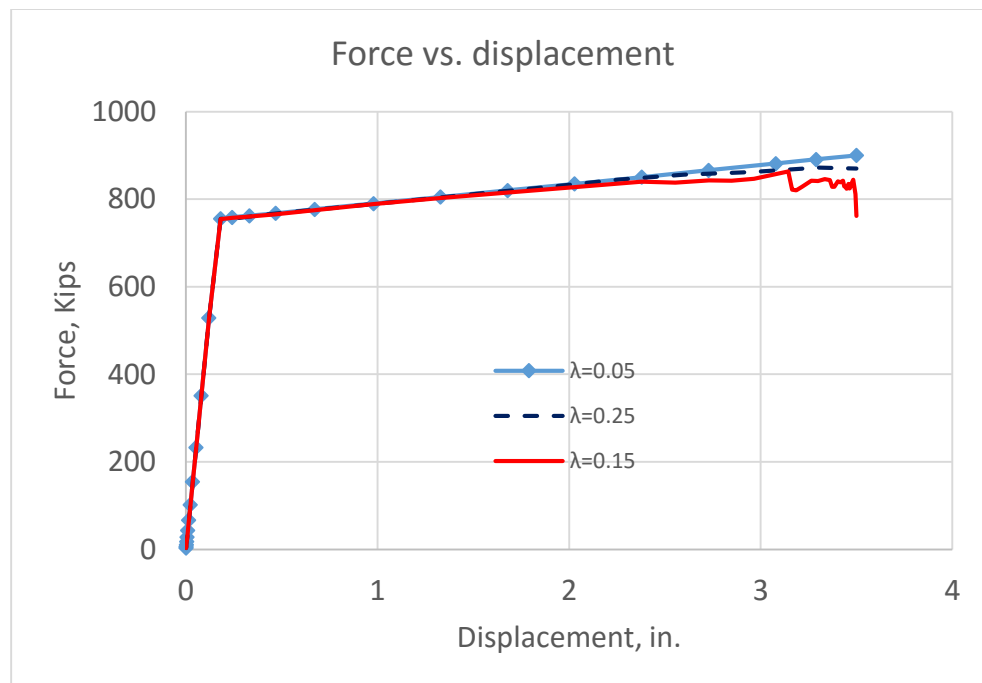
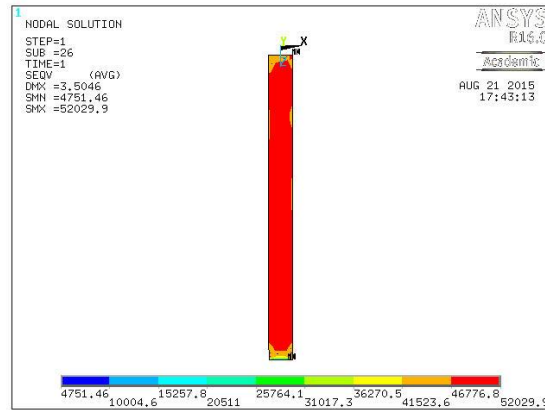
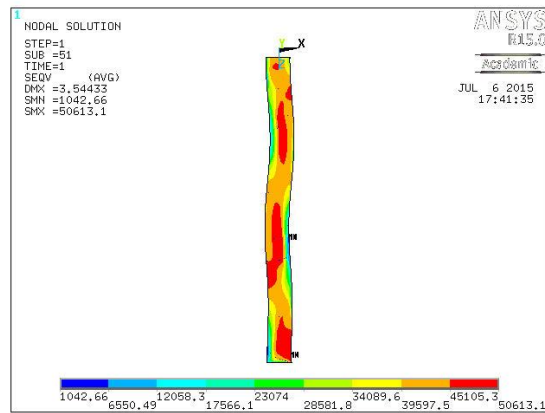


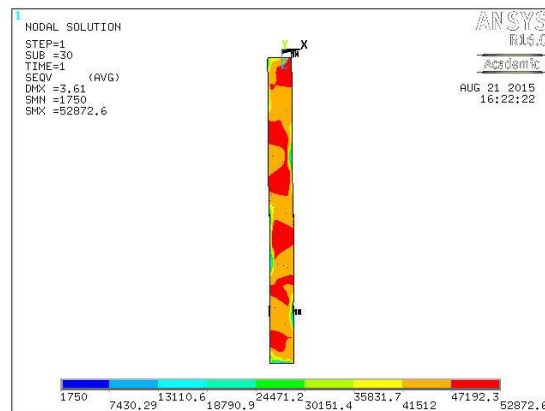
Figure 4.8 Force vs. displacement for the same model with different value of λ



(a)



(b)



(c)

Figure 4.9 Von misses stress distribution and the deformation on the core plates with different value of λ : (a) $\lambda = 0.05$, (b) $\lambda = 0.15$ and (c) $\lambda = 0.25$

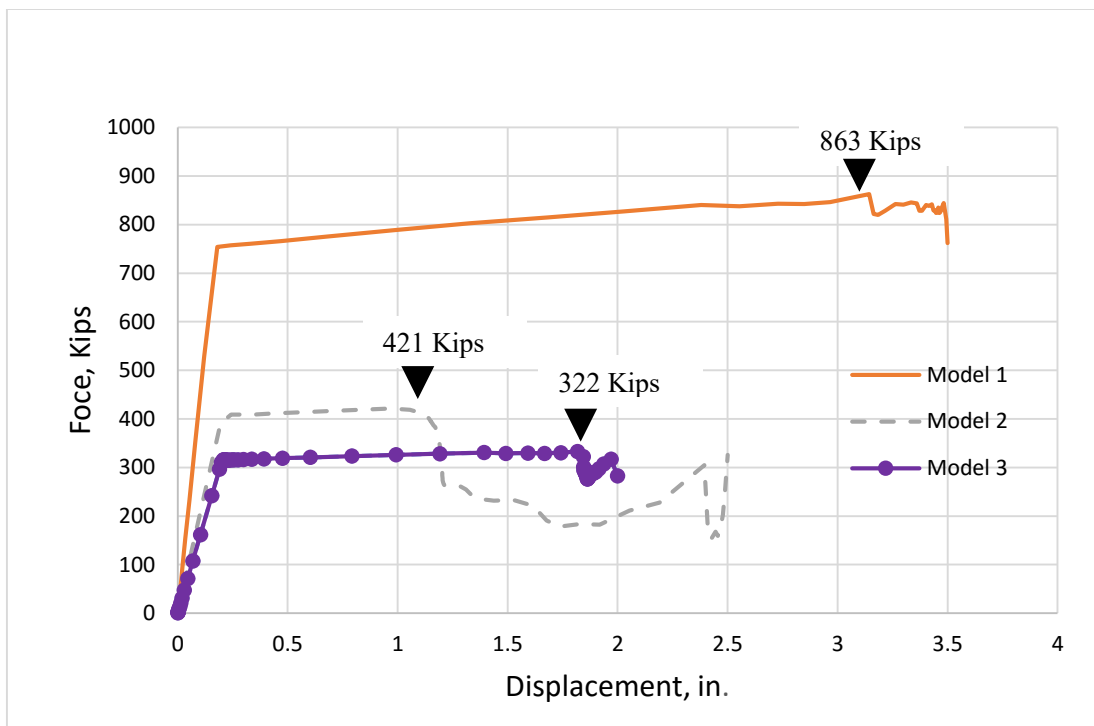
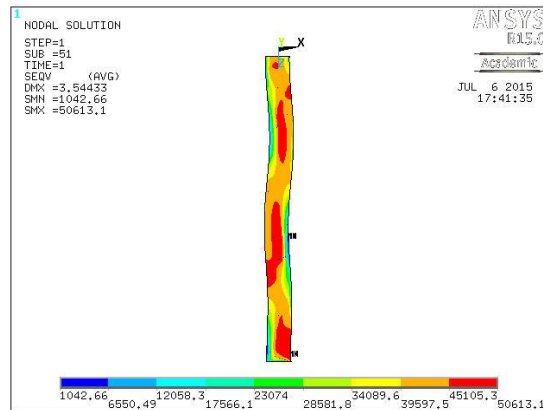
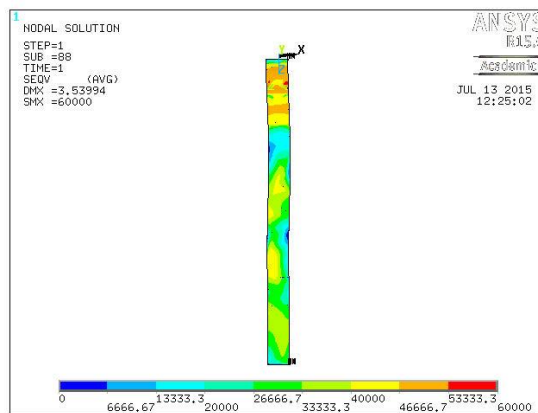


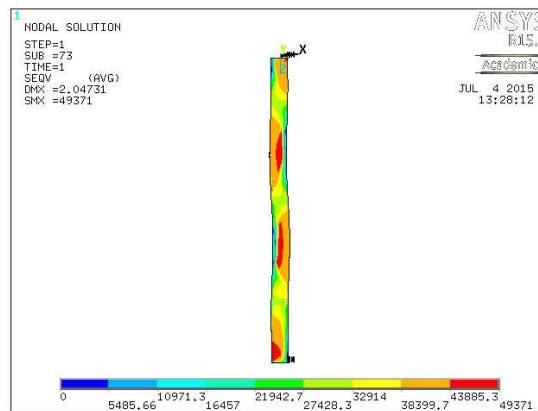
Figure 4.10 Axial compressive force vs. the displacement for three models



(a)

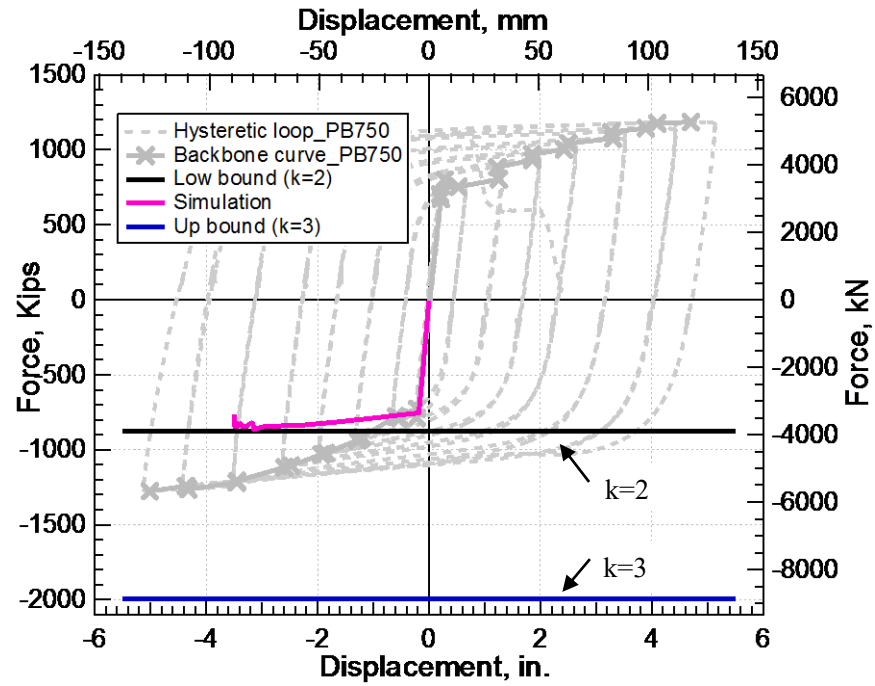


(b)

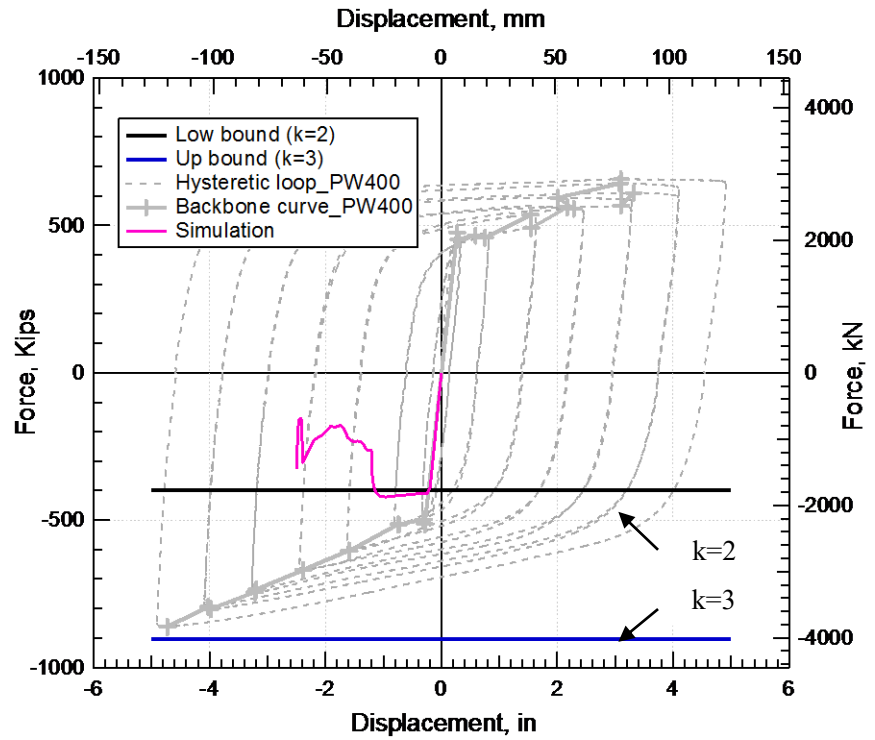


(c)

Figure 4.11 Deformation of the core in the three models: (a) Deformation of the core in model 1 (2 waves), (b) Deformation of the core in model 2 (1.5 waves) and (c) Deformation of the core in model 3 (2 waves)

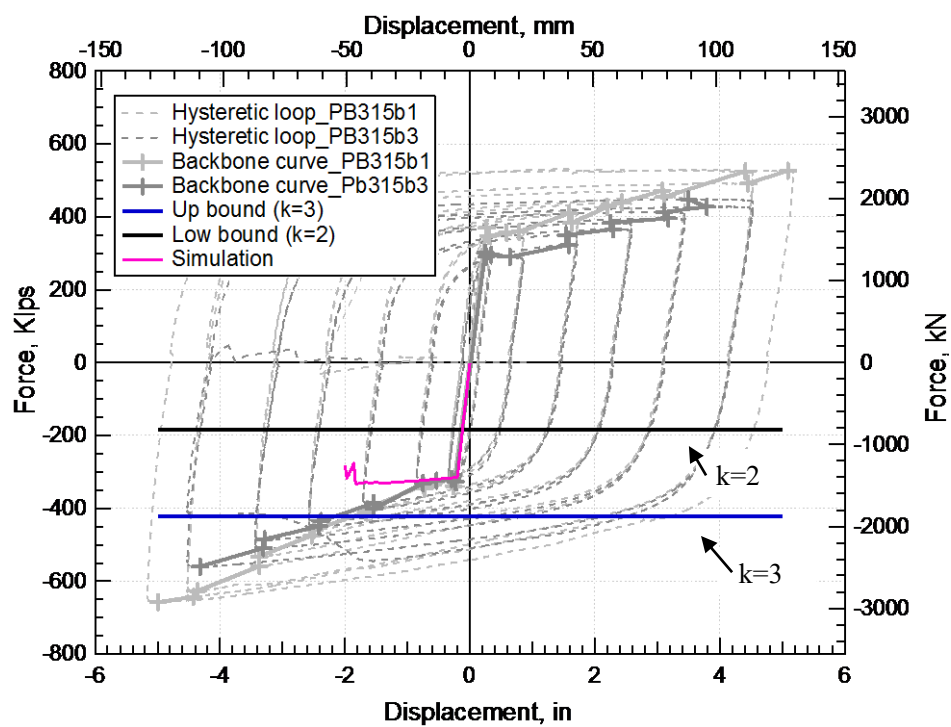


(a)



(b)

Figure 4.12 Comparison of test result with calculation and simulation result (k is the wave number): (a) Test 1, (b) Test 5 and (c) Tests 6 and 8



(c)

Figure 4.12 Continued

CHAPTER 5

STRUT-AND-TIE MODEL FOR THE CROSS-SECTION OF THE BRBS

In some of the experiments, BRBs had the core plates buckling in the strong-axis, as shown in Figures 3.9 (a), (e), (f) and (h), while some BRBs had the core plates buckling in the weak-axis, as shown in Figures. 3.9 (c) and (g). Once concrete crushes, concrete powder falls due to the gravity. The space occupied by concrete will be available for core plates to deform. Core plates in all BRBs are flat, which means that the width of core plates is much larger than the thickness. Since the cross-section of the BRB is square-shaped, the concrete cover in the strong axis of core plates is much thinner than the concrete cover in the weak axis of core plates. Therefore, compared to weak-axis buckling, the strong-axis buckling of core plates has a great potential to cause bulging and subsequent local buckling of the steel casing. The bulging on the casing in test 1 is shown in Figure 5.1, which was caused by the strong-axis buckling of the core plates.

This section aims to use the strut-and-tie model (STM) to find the critical angle between the strut and tie to prevent the local buckling of the steel casing.

5.1 Theory of STM

Zsarnoczay (2013) suggested that the lower bound of the ratio of width to thickness of the core plates should not be smaller than 2 to avoid strong-axis buckling. In

the present experiments, the ratio of the width to the thickness of the core plates ranges from 3.125 to 10. The ratios of the width to the thickness of the core plates in all specimens are greater than the lower bound suggested by Zsarnoczay (2013), but the strong-axis buckling still occurs. Therefore, a new theory is needed to explain this phenomenon.

Since the debonding material or the air gap between the concrete and the core plates are very thin, the core plates will easily contact and compress the concrete under cyclic loading when they buckle. When the contact force, which is applied on concrete from core plates, reaches the compressive strength of concrete, concrete starts to crack. The steel casing works as confinement to hold the concrete together, even as the concrete cracks. Along with increasing axial compressive force on the core, the core deforms and produces greater compressive forces on the concrete. This compressive force is transferred through the concrete to the steel casing. When the compressive force from the core reaches a critical value, the steel casing bulges, which usually happens when the core buckles.

The STM is a truss idealization of composite members consisting of steel ties and concrete struts. The STM approach has evolved as one of the most useful design methods for shear critical structures, such as deep beam analysis, beam column joints, and for other disturbed regions in concrete structures. The STM theory is used to explain why the strong-axis buckling or weak-axis buckling occurs for a given BRB.

5.2 Strut-and-Tie Model Built in BRB Cross-Section

The STM method is a conceptual framework where the stress distribution in a structure is idealized as a system of struts, ties and nodes. A strut is a compression

member which consists of concrete and carries compressive forces. A tie is a tension member which consists of the steel reinforcement and carries tension forces. A node is the connection between a strut and a tie, which consists of concrete.

5.2.1 The STM for the Cross-Section of a BRB

The cross-section of a BRB is shown in Figure 5.2 (a). In the cross-section of a BRB, the node is located in the concrete, right next to the core; the tie is the steel casing; and the struts represent the concrete between the core and the casing. The simplified STM for the left part of the cross-section of a BRB is shown in Figure 5.2 (b). The compressive force on the node applied by the core plates is the contact force, $2F_B$, which was obtained in Chapter 4. According to force equilibrium in the horizontal direction, the tensile force in the tie is B due to the geometric symmetry of the STM.

If the core plates buckle in the strong-axis direction, the node certainly cracks first. Therefore, the failure mode of the model is either concrete strut cracking or tension tie yielding.

5.2.2 Determination of the Width and Thickness of the Strut and the Tie

The STM is a three-dimensional model. The three-dimensional view of the STM on the left side of the core plates is shown in Figure 5.2 (c). This figure shows the STM for the BRB in one perpendicular dimension along the length of the BRB.

The perpendicular dimension of the strut or tie is perpendicular to its axis and the plane of the truss model. In this case, the half buckling wavelength of the core plates will be used as the perpendicular dimension of the strut or tie, shown in Figure 5.3. Figure 5.3 (a) shows the overall view of a core plate, in which the solid-red-colored face is

perpendicular to the weak axis of the core plate, and the pattern-green-colored face is perpendicular to the strong axis of the core plate. Figure 5.3 (b) shows one wavelength and half wavelength for strong-axis buckling, which are L_s and $L_s/2$, respectively.

Figure 5.2 (b) shows the plan view of the STM for the cross-section of the BRB. Lines DE, AD, AO are tensile ties in the steel casing. Points A and D are cross points for these three axial lines. They are also the nodes for the strut-and-tie model. The two core plates apply a compressive force, $2F_B$, on the concrete in the direction of the arrow. This force is considered as a concentrated force and the loading point is at the midpoint along the thickness of the core plates, which is point C in this figure.

One edge of the strut is obtained by drawing a line parallel to line DC from the corner of the core plate (point F), and this line crosses the casing at point G. The other edge of the strut (line JK) is obtained by mirroring line FG about line CD. The other strut (AC) is obtained by using the same method.

Therefore, the triangle ADC is the simplified strut-and-tie model for the cross section of the BRB. The points A, D, and C are the nodal points; w_t and w_s are the width of the tie and the strut, respectively.

5.3 General Equation for the Critical Angle

5.3.1 Strength of the Tie

In the cross-section of the BRB, the tie is the steel casing. The tensile force, F_t , in the tie can be expressed in Eq. (5.1). Since the steel casing may not yield when the concrete strut cracks, the tensile stress of the steel, f_s , is used here.

$$F_t = A_s f_s \quad (5.1)$$

where A_s is the cross-sectional area of the tie (in this case the cross-sectional area of one

of the four sides of the steel casing), which is the product of the tie thickness and the perpendicular dimension of the tie, $L_s/2$. An expression for A_s is shown in Eq. (5.2). The tensile force in the tie, F_t , is expressed in Eq. (5.3) by substituting A_s from Eq. (5.2) in Eq. (5.1):

$$A_s = w_t (L_s/2) \quad (5.2)$$

$$F_t = w_t f_s (L_s/2) \quad (5.3)$$

where w_t is the width of the tie or thickness of the steel casing wall, L_s is the wavelength when the core plate buckles in the strong axis, and $L_s/2$ is the perpendicular dimension for the STM when the core plates buckle in the strong axis.

5.3.2 Strength of the Strut

According to the ACI Building Code 318 (2014), the compressive force in the strut can be expressed using Eq. (5.4):

$$F_{ns} = 0.85 f'_c \beta_s A_c \quad (5.4)$$

where F_{ns} is the nominal compressive strength of the strut; f'_c is the compressive strength of the concrete; A_c is the cross-sectional area of the strut, which is the product of the width, w_s , and the perpendicular dimension of the strut, $L_s/2$, as shown in Figure 5.3; For a strut of uniform cross-sectional area over its length, the value of β_s equals 1.0; and A_c is expressed in Eq. (5.5):

$$A_c = w_s (L_s/2) \quad (5.5)$$

From Figure 5.2 (a), the width of the strut, w_s , is equal to NH. Because line FH is parallel to line DA, the angle between line HF and FN is equal to the angle between line CA and line AD, θ . In the right-angle triangle HNF, the length of line NH can be obtained from Eq. (5.6). Substituting Eq. (5.6) into Eq. (5.5), the cross-sectional area of the strut,

A_c , can be expressed in Eq. (5.7). Therefore, the nominal compressive strength of the strut can be expressed as Eq. (5.8) by substituting Eq. (5.7) into Eq. (5.4).

$$w_s = L_{NH} = t_c \sin\theta \quad (5.6)$$

$$A_c = t_c \sin\theta (l_s/2) \quad (5.7)$$

$$F_{ns} = 0.85 f'_c \beta_s (t_c \sin\theta) (L_s/2) \quad (5.8)$$

where w_s is the width of the strut, L_{NH} is the length of the line NH, t_c is the total thickness of the core plates, and θ is the angle between the strut and the tie.

5.3.3 Strength of the Nodal Zones

Both nodes and struts are composed of concrete. Once the nodes crush, the cracks originating from the nodes will propagate into the struts. Struts crossed by cracks inclined to the axis of the strut are weakened by the cracks. Therefore, the stability of nodes affects the stability of the struts. For nodal zones, the nominal compressive strength of a strut, F_{nn} , is expressed in Eq. (5.9):

$$F_{nn} = f_{cu} A_n \quad (5.9)$$

where F_{nn} is the strength of the nodal zone; A_n is the area of face of the node that the strut or tie acts on, perpendicular to the axis of strut and tie, so it equals either A_c or A_t ; and f_{cu} is the effective compressive strength of the concrete and is expressed in Eq. (5.10). Substituting Eq. (5.10) into Eq. (5.9), the nominal compressive strength of the nodal zone can be expressed in Eq. (5.11).

$$f_{cu} = 0.85 \beta_n f'_c \quad (5.10)$$

$$F_{nn} = 0.85 \beta_n f'_c A_n \quad (5.11)$$

where the value of β_n equals 1.0 in nodal zones bounded on all sides by struts or bearing areas, or both.

5.4 Evaluation of the Nodal Zones

When strong-axis buckling occurs, the nodal zone is cracked and the struts may or may not crush. Therefore, the stress in the nodal zones will be checked to get the critical angle between the strut and tie, which determines the buckling direction of the core plates for a given BRB.

5.4.1 Node C

The compressive force from the core plates, $2F_B$, is applied to Node C; compressive forces from the struts, F_n , are also applied to Node C, which is a compression-compression-compression node (C-C-C), and is shown in Figure 5.4.

5.4.1.1 Stress on the Right Surface of Node C

The right surface of node C is subjected to a compressive force, $2F_B$, which is the contact force between the concrete and core plates. The stress on the right surface of node C equals the force over the area of contact surface between the concrete and core plates, expressed in Eq. (5.12).

$$f(\text{right}) = \frac{2F_B}{A_{co}} = \frac{2F_B}{t_c L_s / 2} \quad (5.12)$$

where A_{co} is the area of contact surface between the concrete and core plates, F_B is the compressive force on the node, t_c is total thickness of the core plates, and $L_s/2$ is the perpendicular dimension of the STM.

In Chapter 4, it was discussed that the contact force, F_B , varies for the odd waves and the even waves on the core plate, as expressed in Eqs. (4.24) and (4.27). Substituting Eqs. (4.24) and (4.27) into Eq. (5.12), respectively, and the stress on the right surface of node C can be obtained in Eqs. (5.13) and (5.14). Theoretically, to ensure

the integrity of node C, the stress on the right surface of node C cannot be greater than the nominal compressive stress, f_{nn} .

$$f(\text{right}) = \frac{16\pi^2 E_{r-co} I_{co} e}{t_c L_s \left(\frac{L_c - c_0}{k}\right)^2 \left(\frac{L_c - c_0}{k} + 8\mu e - 8k\mu e\right)} \leq f_{nn} \quad (k=1, 3, 5 \dots) \quad (5.13)$$

$$f(\text{right}) = \frac{16\pi^2 E_{r-co} I_{co} e}{t_c L_s \left(\frac{L_c - c_0}{k}\right)^2 \left(\frac{L_c - c_0}{k} - 8k\mu e\right)} \leq f_{nn} \quad (k=2, 4, 6 \dots) \quad (5.14)$$

where E_{r-co} is the reduced modulus of the core plate, I_{co} is the moment of the inertia of the core plate, μ is the frictional coefficient between core plate and the concrete, e is the thickness of the air gap, and k is the amount of the waves on the core plates.

5.4.1.2 Stress on the Left Surface (Top and Bottom) on the Node C

The force distribution and cross-sectional area on the left surfaces of node C are the same. Therefore, only one surface is used for the calculation of the angle between the strut and the tie.

From force equilibrium in the horizontal direction of node C in Figure 5.5, Eq. (5.15) can be obtained.

$$F_n = \frac{F_B}{\sin\theta} \quad (5.15)$$

The left surface of node C maintains its integrity if $F_{nn} \geq F_n$. This equation can be revised as Eq. (5.16) by substituting Eqs. (5.15) and (5.11). Moving all terms with θ to the left side of the equation, Eq. (5.16) is transformed into Eq. (5.17).

$$F_{nn} = F_{nn} = 0.85\beta_n f'_c A_n = 0.85\beta_n f'_c t_c \sin\theta L_s / 2 \geq \frac{F_B}{\sin\theta} \quad (5.16)$$

$$\sin\theta^2 \geq \frac{2F_B}{0.85f'_c \beta_n t_c L_s} \quad (5.17)$$

where A_n is the area of the face of the node that the strut acts on, perpendicular to the axis of strut and tie.

When odd waves occur in the core plate, Eq. (4.24) is substituted into Eq. (5.17) to get Eq. (5.18). The angle between concrete and the core plate can be expressed in Eq. (5.19) for an odd number of waves.

$$\sin\theta^2 \geq \frac{8\pi^2 E_{r-co} I_{co} e}{0.85 f'_c \beta_n t_c L_s \left(\frac{L_c-co}{k}\right)^2 \left(\frac{L_c-co}{k} + 8\mu e - 8k\mu e\right)} \quad (k=1, 3, 5\dots) \quad (5.18)$$

$$\theta \geq \arcsin \sqrt{\frac{8\pi^2 E_{r-co} I_{co} e}{0.85 f'_c \beta_n t_c L_s \left(\frac{L_c-co}{k}\right)^2 \left(\frac{L_c-co}{k} + 8\mu e - 8k\mu e\right)}} \quad (k=1, 3, 5\dots) \quad (5.19)$$

For an even number of waves, the contact force, F_B , is expressed in Eq. (4.27). Substituting Eq. (4.27) into Eq. (5.17), it can be transformed into Eq. (5.20). Simplifying Eq. (5.18), the angle between strut and tie can be found in Eq. (5.21) when even number of the waves occur.

$$\sin\theta^2 \geq \frac{8\pi^2 E_{r-co} I_{co} e}{0.85 f'_c \beta_n t_c L_s \left(\frac{L_c-co}{k}\right)^2 \left(\frac{L_c-co}{k} - 8k\mu e\right)} \quad (k=2, 4, 6\dots) \quad (5.20)$$

$$\theta \geq \arcsin \sqrt{\frac{8\pi^2 E_{r-co} I_{co} e}{0.85 f'_c \beta_n t_c L_s \left(\frac{L_c-co}{k}\right)^2 \left(\frac{L_c-co}{k} - 8k\mu e\right)}} \quad (k=2, 4, 6\dots) \quad (5.21)$$

From Eqs. (5.19) and (5.21), it can be seen that the angle between strut and tie is inversely proportional to concrete compression strength. If other factors remain the same, increasing concrete compression strength can reduce the angle to prevent the local buckling of the steel casing.

5.4.2 Nodes A and D

Since the STM geometry is symmetric and the strut forces are assumed to be equal, only a node D is analyzed. Node D is subjected to tensile forces from two ties and a compressive force from one strut, as shown in Figure 5.5, and is a compression-tension-tension node (C-T-T).

5.4.2.1 Stress on Right Surface of Node D

The right top surface of node D resists a tensile force with the value of contact force, F_B , which is obtained from the force equilibrium in the horizontal direction for the whole strut and tie model in Figure 5.2(b). Therefore, the stress on this surface of the node is the contact force over the cross-sectional area of the tie, which is expressed in Eqs. (5.22) and (5.23). Eq. (5.22) shows the case when the core plates have odd waves and Eq. (5.23) when the core plates have even waves.

$$f(\text{right top}) = \frac{F_B}{A_t} = \frac{8\pi^2 E_r - c o l c o e}{w_t L_s \left(\frac{L_c - c o}{k}\right)^2 \left(\frac{L_c - c o}{k} + 8\mu e - 8k\mu e\right)} \leq f_y \quad (k=1, 3, 5 \dots) \quad (5.22)$$

$$f(\text{right top}) = \frac{F_B}{A_t} = \frac{8\pi^2 E_r - c o l c o e}{w_t L_s \left(\frac{L_c - c o}{k}\right)^2 \left(\frac{L_c - c o}{k} - 8k\mu e\right)} \leq f_y \quad (k=2, 4, 6 \dots) \quad (5.23)$$

When strong-axis buckling occurs in the core plates, they compress the concrete to the left or right side along the width direction of the core plate. Node C crushes first, while struts may or may not crush, which depends on how much the core plates deform. After the struts crush, the core plates deform more in the horizontal direction in Figure 5.2; the left and right walls of the steel casing will have a chance to yield, and even budge rather than the top and bottom walls of the steel casing. Therefore, the stress on this surface of the node might be smaller than the yielding stress of the steel casing ($f_y=60\text{ksi}$).

5.4.2.2 Stress on the Bottom Surface of Node D

This surface is subjected to the tensile force from tie, F_t . From the force equilibrium on node D in Figure 5.5, F_t can be expressed as

$$F_t = F_B / \tan\theta \quad (5.24)$$

Contact force, F_B , is expressed in Eqs. (4.24) and (4.27), which is substituted in

Eq. (5.24) for the calculation of θ . When the core plate has an odd number of waves, the stress in the tie can be expressed in Eq. (5.25).

The tie does not yield in the early stages when the strong-axis buckling occurs in the core plates. When the core plates deform at large scale, the core plates crush the strut and bear on the steel casing, causing it to yield. Therefore, at the beginning of core plate buckling about the strong axis, the stress in the steel casing is less than the yield stress. When the strong-axis buckling of the core plates starts, the tie on the left or the right walls of the steel casing has not yielded yet. The relationship between the stress in the tie and the yield stress of the steel casing is expressed in Eq. (5.26). The angle between the strut and tie from this limitation is expressed in Eq. (5.27). When the core plate has an even number of waves, stress in the tie can be expressed in Eq. (5.28). The angle between the strut and tie from this limitation is expressed in Eq. (5.29).

$$f(\text{bottom}) = \frac{F_t}{A_t} = \frac{F_B}{w_t \left(\frac{L_s}{2}\right) \tan \theta} = \frac{\frac{4\pi^2 E_{r-co} I_{co} e}{\left(\frac{L_c - c_0}{k}\right)^2 \left(\frac{L_c - c_0}{k} + 8\mu e - 8k\mu e\right)}}{\frac{w_t L_s}{2} \tan \theta} \quad (5.25)$$

$$f(\text{bottom}) = \frac{8\pi^2 E_{r-co} I_{co} e}{w_t L_s \tan \theta \left(\frac{L_c - c_0}{k}\right)^2 \left(\frac{L_c - c_0}{k} + 8\mu e - 8k\mu e\right)} \leq f_y \quad (k=1, 3, \dots, (2n-1)) \quad (5.26)$$

$$\theta \geq \arctan\left(\frac{8\pi^2 E_{r-co} I_{co} e}{f_y w_t L_s \left(\frac{L_c - c_0}{k}\right)^2 \left(\frac{L_c - c_0}{k} + 8\mu e - 8k\mu e\right)}\right) \quad (k=1, 3, \dots, (2n-1)) \quad (5.27)$$

$$f(\text{bottom}) = \frac{4\pi^2 E_{r-co} I_{co} e}{w_t (L_s/2) \tan \theta \left(\frac{L_c - c_0}{k}\right)^2 \left(\frac{L_c - c_0}{k} - 8k\mu e\right)} \leq f_y \quad (k=2, 4, 6, \dots) \quad (5.28)$$

$$\theta \geq \arctan\left(\frac{8\pi^2 E_{r-co} I_{co} e}{f_y w_t L_s \left(\frac{L_c - c_0}{k}\right)^2 \left(\frac{L_c - c_0}{k} - 8k\mu e\right)}\right) \quad (k=2, 4, 6, \dots) \quad (5.29)$$

where F_t is the tensile force in the tie, A_t is the area of the cross section of the tie, $2F_B$ is the contact force on the concrete from the steel core plates, w_t is the width of the tie, $L_s/2$ is the perpendicular dimension of the tie, θ is the angle between the strut and the

tie, E_{r-co} is the reduced modulus of the core plate, I_{co} is the moment of the inertia of the core plate, μ is the frictional coefficient between the core plate and the concrete, e is the thickness of the air gap, and k is the amount of the waves.

5.4.3 The Critical Angle between the Strut and Tie, θ_{cr}

Only Eqs. (5.19), (5.21), (5.27), and (5.29), obtained in Sections 5.4.1.2, and 5.4.2.2, involve θ . Therefore, these four equations are used to find the critical angle between the strut and the tie, θ_{cr} .

The wavelength of the core plates, L_{sk} , can be obtained by dividing the critical length of the core plates, L_{c-co} , by the wave number, k , which is expressed in Eq. (5.30):

$$L_{sk} = \frac{L_{c-co}}{k} \quad (5.30)$$

The critical angle between the strut and the tie is chosen as the maximum value of all the minimum angles obtained in the previous section by replacing L_{sk} with (L_{c-co}/k) . Therefore, the critical angle between strut and tie will be expressed as Eq. (5.31) for the case when odd waves occur in the core plates, and Eq. (5.32) for the case when even waves occur in the core plates.

$$\theta_{cr} = \max \left\{ \begin{array}{l} \arctan \left[\frac{8\pi^2 E_{r-co} I_{co} e}{f_y w_t \left(\frac{L_{c-co}}{k}\right)^3 \left(\frac{L_{c-co}}{k} + 8\mu e - 8k\mu e\right)} \right], \\ \arcsin \sqrt{\frac{8\pi^2 E_{r-co} I_{co} e}{0.85 f_c' \beta_s t_c \left(\frac{L_{c-co}}{k}\right)^3 \left(\frac{L_{c-co}}{k} + 8\mu e - 8k\mu e\right)}} \end{array} \right\} \quad (k=1, 3, 5\dots) \quad (5.31)$$

$$\theta_{cr} = \max \left\{ \begin{array}{l} \arctan \left[\frac{8\pi^2 E_{r-co} I_{co} e}{f_y w_t \left(\frac{L_{c-co}}{k}\right)^3 \left(\frac{L_{c-co}}{k} - 8k\mu e\right)} \right], \\ \arcsin \sqrt{\frac{8\pi^2 E_{r-co} I_{co} e}{0.85 f_c' \beta_s t_c \left(\frac{L_{c-co}}{k}\right)^3 \left(\frac{L_{c-co}}{k} - 8k\mu e\right)}} \end{array} \right\} \quad (k=2, 4, 6\dots) \quad (5.32)$$

From both equations above, it can be seen that the critical angle between strut and

tie is inversely proportional to the thickness of steel casing. Increasing thickness of steel casing can reduce the value of critical angle. In other words, increasing the thickness of the steel casing wall, w_t , and keeping the rest part of BRBs the same, can help prevent the local buckling of the steel casing.

5.5 Calculation of Critical Angle for the Specimens Tested in the Laboratory

Assuming that all nine specimens had strong-axis buckling, critical angles, θ_{cr} , are calculated for these specimens. The parameters needed for the calculation are listed in Table 5.1. The predicted critical angle based on the STM model, θ_{cr} , will be compared with the real angle between the strut and tie in the specimens.

In Table 5.1, I_{co} is the moment of the inertia for the core plate, L_{c-co} is the critical length of the core plate, and k is the calculated wave number. Since the wave number has to be an integer for the purpose of choosing the equation for calculation, the wave number was chosen by a rounding-off method. These wave numbers are listed as k_{even} or k_{odd} ; t_c is the total thickness of the core plates; μ is the frictional coefficient between the concrete and the steel core plates; e is the air gap size; E_{r-co} is the reduced the modulus for the steel core, which was calculated in Chapter 4; w_t is the width of the tie; θ_1 is the angle between strut and tie obtained from Eq. (5.21); θ_2 is the angle between strut and tie obtained from Eq. (5.29); θ_3 is the angle between strut and tie obtained from Eq. (5.19); θ_4 is the angle between strut and tie obtained from Eq. (5.27); the critical angle θ_{cr} is obtained by choosing the maximum value of the two angles in Eqs. (5.21) and (5.29) or Eqs. (5.19) and (5.27). The actual angle between the strut and tie, θ_{actual} , is obtained from the geometry of the BRB cross-section.

When the value of the actual angle is close to the value of the critical angle, the core plates of the BRB buckle in the strong axis or a combination of strong axis and weak axis. However, when the actual angle between the strut and tie is much larger than the critical angle, weak-axis buckling occurs.

Table 5.1
The critical angles for each specimen to determine if strong-axis buckling occurs

| Parameters | Test1 | Test3 | Test5 | Test6 | Test7 | Test8 | Test9 |
|---------------------------|-------------|-------------|------------|----------------|-------------|----------------|------------|
| I_{co}, in^4 | 131.9 | 40.7 | 83.3 | 38.8 | 38.8 | 38.8 | 83.3 |
| L_{c-co}, in | 123 | 135 | 153 | 157 | 157 | 157 | 153 |
| k | 1.96 | 3.18 | 2.25 | 2.98 | 2.98 | 2.98 | 2.25 |
| k_{even} | 2 | - | 2 | - | - | - | 2 |
| k_{odd} | - | 3 | - | 3 | 3 | 3 | - |
| t_c, in | 2 | 2 | 1 | 1 | 1 | 1 | 1 |
| μ | 0.57 | 0.57 | 0.57 | 0.57 | 0.57 | 0.57 | 0.57 |
| e, in | 0.063 | 0.063 | 0.063 | 0.063 | 0.063 | 0.063 | 0.063 |
| E_{r-co}, psi | 2528316 | 2528316 | 2528316 | 2528316 | 2528316 | 2528316 | 2528316 |
| w_t, in | 0.25 | 0.25 | 0.25 | 0.25 | 0.25 | 0.25 | 0.25 |
| $(L_s/2)_{even}, in$ | 30.8 | - | 38.3 | - | - | - | 38.3 |
| $(L_s/2)_{odd}, in$ | - | 22.5 | - | 26.2 | 26.2 | 26.2 | - |
| $\theta_1, ^\circ$ | 7.5 | - | 5.4 | - | - | - | 5.4 |
| $\theta_2, ^\circ$ | 0.4 | - | 0.1 | - | - | - | 0.1 |
| $\theta_3, ^\circ$ | - | 7.7 | - | 7.9 | 7.9 | 7.9 | - |
| $\theta_4, ^\circ$ | - | 0.5 | - | 0.2 | 0.2 | 0.2 | - |
| $\theta_{cr}, ^\circ$ | 7.5 | 7.7 | 5.4 | 7.9 | 7.9 | 7.9 | 5.4 |
| Casing size, in | 12x12 | 12x12 | 12x12 | 10x10 | 10x10 | 10x10 | 12x12 |
| Width of the core, in | 9.25 | 6.25 | 10 | 7.75 | 7.75 | 7.75 | 10 |
| $\theta_{actual}, ^\circ$ | 13.3 | 28.9 | 8.1 | 11.6 | 11.6 | 11.6 | 8.1 |
| Real buckling direction | S | W | S | W and S | W | W and S | W |

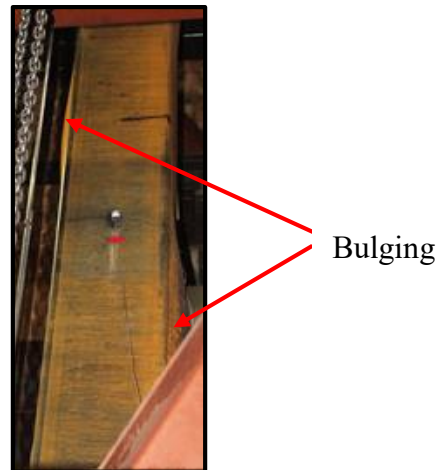
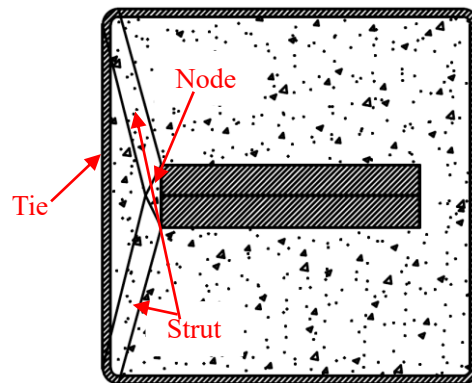
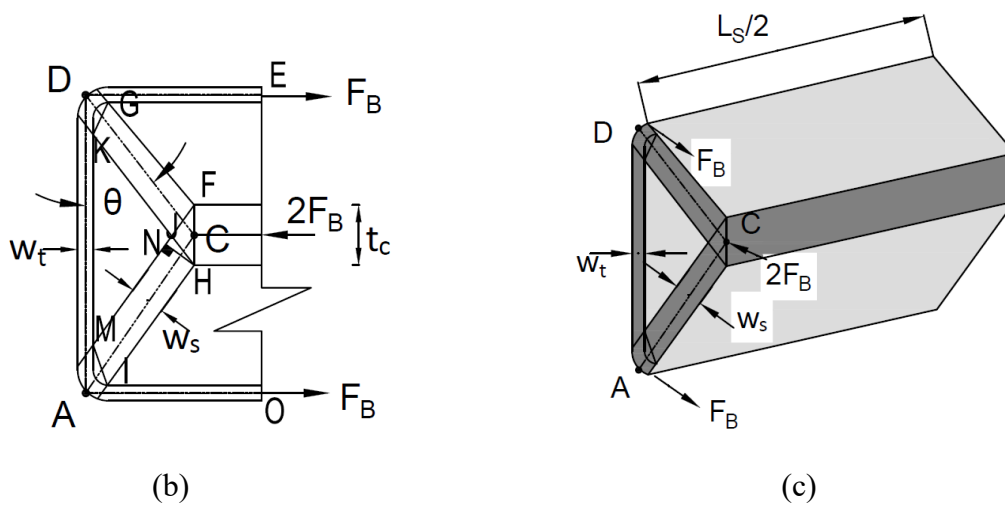


Figure 5.1 Bulging on the steel casing during test 1



(a)



(b)

(c)

Figure 5.2 Built-up of strut-and-tie model: (a) Cross-section of BRB in test 1, (b) Plain view of STM and (c) Three-dimensional view of STM

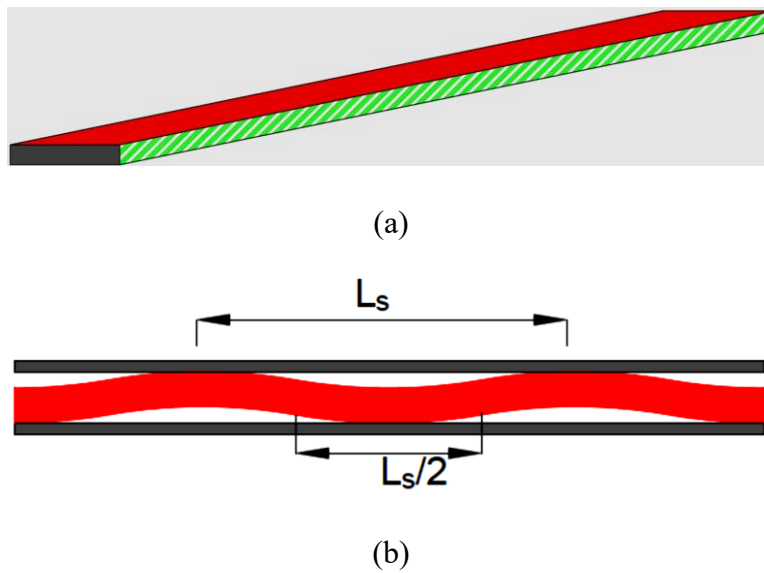


Figure 5.3 Definition of wavelength for strong-axis buckling on the core: (a) Overall view of the core and (b) One wavelength and half wavelength

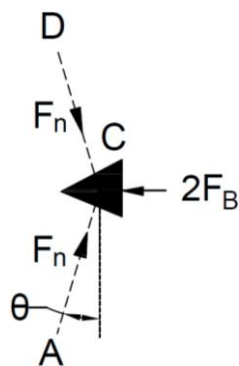


Figure 5.4 Forces distribution on node C

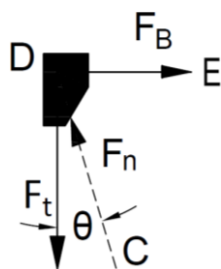


Figure 5.5 Force distribution on node D

CHAPTER 6

ANALYTICAL SIMULATION OF BRBS AND CASING

THICKNESS REQUIRED FOR LONG BRBS

Testing full-size BRBs in the laboratory is costly and time consuming. Under optimal conditions, it takes four weeks to build and test one BRB. Analyzing BRBs can help reduce testing time and financial costs significantly. In addition, different parameters can be modeled and investigated to simulate BRBs of various core plate areas and lengths.

In this section, simulation of nine BRB tests will be carried out using a general finite element program, Ansys. After the parameters of the material property for the BRB are determined by comparing the simulation results with the corresponding test results, the BRB model will be used to determine a relationship between BRB length and the casing thickness when the cross-sectional dimensions of the BRB and the steel core are given. The code requirements for the BRB casing design adopted in AISC 360 (2010) is used to help determine the initial thickness of the steel casing for the simulation.

6.1 Material Property Determination for BRB Models in ANSYS

6.1.1 Modeling

When steel material is loaded, the axial stress keeps increasing until the material yields. If the load is continuously applied on the steel material, the axial stress will move

out of the yielding surface to the plastic range. When plasticity occurs under cyclic loads, two types of material hardening models are involved: isotropic hardening and kinematic hardening. The isotropic hardening causes plastic homogeneousness in the material behavior, while the kinematic hardening causes plastic anisotropy in the material behavior.

In the simulation, the model is simplified by only considering the BRB from connection plate to connection plate. Therefore, only the steel core plate, concrete, gap, and steel casing are involved in the finite element model. Element SOLID186 is used for the concrete, the steel core, and the steel casing, which is a higher order three-dimensional 20-node solid element that exhibits quadratic displacement behavior. The element TARGE 170 is used to represent various three-dimensional “target” surfaces for the associated contact elements. The element CONTA 174 is used to represent contact and sliding between three-dimensional “target” surfaces and a deformable surface, defined by this element. The gap between the concrete and the steel core is simulated by using elements TARGE 170 and CONTAC 174. The friction coefficient between the concrete and steel is assumed as 0.57 (Rabbat, et al. 1985). The normal penalty stiffness factor (FKN) varies in the different models, which is used to determine contact stiffness and penetration. The material property for each BRB component is listed in Table 6.1. Bilinear isotropic hardening material property is used for the concrete, and steel casing. The combination of multilinear isotropic and nonlinear kinematic models is used for the steel core. The nine BRBs tested are simulated in Ansys. The geometries for the nine BRB models are listed in Table 6.2.

6.1.2 Effect of FKN on the Hysteretic Loops

FKN is the normal penalty stiffness factor, which is used to determine contact stiffness and penetration. The value FKN not only affects the convergence of the simulation, but also affects the shape of the hysteretic loop. The simulations are run with three different values of FKN: 0.01, 0.05, and 1 for the same model. The rest of the parameters are kept the same for the three simulations. The hysteretic loops for these three initial simulations for model C1 are shown in Figure 6.1. The hysteretic loops for FKN=0.01 are shown using a red dotted line. The hysteretic loops for FKN=0.05 are shown using a blue dashed line and the hysteretic loops for FKN=1 are shown using a solid brown line. It can be seen that the smaller the value of FKN, the squarer the hysteretic loops. The hysteretic loops get higher in the first and third quadrants and lower in the second and forth quadrants, as the value of FKN increases.

6.1.3. Effect of the Stress-Strain Curve for Multilinear Isotropic Hardening Material on the Shape of the Hysteretic Loops

The stress-strain curve for the core plate was provided by coupon tests from the manufacturer, but the ultimate strain was not provided. From the full-scale BRB test results, the strain in the core plates ranged from 2.9% to 4.2%. Therefore, the effect of the stress-strain curve of the core plates on the hysteretic loops is investigated.

Two stress-strain curves for the core plates are shown in Figure 6.2. One is higher, as shown by the dotted line, and the other is lower, as shown by the solid line. The hysteretic loops for the BRBs obtained by using the two stress-strain curves are shown in Figure 6.3. The hysteretic loops from the low stress-strain curve is a solid line and those from the high stress-strain curve is a dotted line. It is obvious that the hysteretic loops are

high and narrow when the stress-strain curve of the multilinear isotropic material property is high. The hysteretic loops are low and wide when the stress-strain curve of the multilinear isotropic material property is low.

6.1.4 The Effect of the Parameters for the Nonlinear Kinematic Hardening Material Property on the Shape of the Hysteretic Loop

In a nonlinear kinematic hardening material model, C_i is the tangent modulus for the i th kinematic model, and γ_i is the decay for the i th kinematic model. Figure 6.4 shows the hysteretic loops obtained by running the same model with different values of C_1 . The hysteretic loops with $C_1 = 4025900$ are shown by the solid line and the hysteretic loops with $C_1 = 6025900$ are shown by the dotted line. It can be seen that the hysteretic loops with a large value of C_1 are higher than the hysteretic loop with small value of C_1 in the first and third quadrant of the hysteresis.

Figure 6.5 shows the hysteretic loops obtained by running the same model with two different values of r_1 . The hysteretic loops with $r_1=500$ are shown using a solid line and the hysteretic loops with $r_1=1000$ are shown using a dotted line. It is obvious that the smaller the r_1 value, the higher the hysteretic loops. The inner corners of the hysteretic loops in the second and fourth quadrants are smaller when r_1 is larger.

6.2 Comparison of the Simulation Results with Corresponding Test Results

To obtain the proper parameters for the nine BRB models, the parameters are adjusted for the simulation according to the effects of those parameters on the shape of the hysteretic loops. Again, it is important to be able to model higher maximum compression than maximum tension in the models. The parameters are listed in Tables

6.3 through 6.11, which are used for the multilinear isotropic and nonlinear kinematic hardening material models for the core plates in the nine models. The FKN values used for each model are listed in the tables as well. From the comparison of the parameters for the specimens in Tables 6.3 through 6.11, the FKN is 0.05 for the BRBs with dual core plates. For the BRB with single core plate, FKN is 0.1 for the BRBS with core plates of 10 in. x 1 in., and FKN is 0.2 for the BRB with core plates of 7.75 in. x 1 in. It can be seen that the smaller the cross-sectional area of core plate is, the higher FKN is. The hysteretic loops and the hysteretic energy dissipation obtained from the simulation are compared with those obtained from the corresponding tests to confirm that the selected parameters are appropriate.

6.2.1 Comparison of the Hysteretic Loops

The hysteretic loops from the simulation and tests of the nine specimens are shown in Figure 6.6. The hysteretic loops from the simulation and corresponding ones from the tests are plotted in the same figure. All simulation results are shown in blue and the test results are shown in red. It can be seen that the shapes of the hysteretic loops from the simulations are very close to the test results.

6.2.2 Comparison of Energy Dissipation

The hysteretic energy dissipation from the simulations is compared with the corresponding test results. Tables 6.12 through 6.15 show the comparison of hysteretic energy dissipation, in which the hysteretic energy dissipation is computed for every two cycles. The difference between the simulation results and the test results is calculated by using Eq. (6.1).

$$Difference = \frac{E_{sim} - E_{test}}{E_{test}} \times 100\% \quad (6.1)$$

where E_{sim} is the hysteretic energy dissipation for every two cycles for the simulation, and E_{test} is the hysteretic energy dissipation for every two cycles for the test.

The difference in the cumulative hysteretic energy dissipation between simulation and test is below 6%. The hysteretic energy dissipation for the first two cycles obtained from the simulation is different from the corresponding test result because the hysteretic dissipation energy for the first two cycles is very small. The hysteretic models cannot predict all the failure modes you can have in a BRB, only the plastification of the core, so the hysteretic loops obtained from the simulation are not close to those obtained from the tests. Therefore, the hysteretic energy dissipation between the simulation and the test for the last two cycles shows a large difference as well. For the rest of the cycles, the hysteretic energy dissipation for the simulation is very close to that for the test result, and most of the differences between the simulation and the tests are below 10%.

The hysteretic energy dissipation for each loading step (two loading cycles) is compared between simulation and test results in Figure 6.7. It can be seen that hysteretic energy dissipation obtained from the simulations is very close to that obtained from the tests for each cycle.

By comparing the hysteretic loops and the hysteretic energy dissipation obtained from the simulation with those obtained from the tests, it can be seen that the parameters chosen for the simulation models are compatible. Those parameters will be used for the simulation of critical thickness of the casing for different length of BRBs.

6.3 Relationship between Thickness of Casing and BRB Length

In this section, BRB models with the parameters chosen in Section 6.2 are simulated to find out a relationship between the thickness of the steel casing and the length of the BRB.

From Tables 6.3 through 6.11, it can be seen that even when the geometry of the BRB is the same, the parameters for the simulation models are different to achieve better fit to the test results, e.g, parameters for model C5 and C9. This is due to the many factors that are not known precisely and cannot be modeled, such as small differences in material properties such as concrete strength or steel yield stress, which vary from specimen to specimen; true thickness and extent of the debonding layer; as well as variations in boundary conditions. Therefore, the average of the parameters for the same geometry and configuration of the BRBs should be used for further BRB casing thickness simulations.

To make sure only one type of buckling model occurs in the core plates, strong-axis or weak-axis buckling, a 6.25 in. \times 2 in. dual steel core is used for the cross-sectional dimension for the core plates in the simulation to make sure that only weak-axis buckling occurs to the BRBs. Hollow structural steel (HSS) square tubes are used for the steel casing. The cross-sections of 12 in. \times 12 in., 14 in. \times 14 in., and 16 in. \times 16 in. HSS square steel tubes are used. The available thickness for HSS sections listed in the AISC code is used in the simulation. Therefore, the thickness of the casing for the cross-sectional dimension of the 12 in. \times 12 in. HSS steel tube casing are 5/8 in., 1/2 in., 3/8 in., 5/16 in., 1/4 in., and 3/16 in. The thickness of the casing for the cross-sectional dimension of the 14 in. \times 14 in. and 16 in. \times 16 in. HSS steel tubes are 5/8 in., 1/2 in., 3/8 in., 5/16 in. The length of the steel casing for a 20-ft.-, 25-ft.-, 30-ft.-, 40-ft.-, 50-ft.-,

and 60-ft.-long BRBs are simulated. The 84 combinations of casing cross-sectional dimension, casing thickness, and the length of the steel casing are simulated.

The FEM model uses the simplified geometry of the BRB, which consists of the steel core plates, and steel casing filled with concrete. Element SOLID 186 is used for the concrete, the steel core, the steel casing, and the connection plates. The gap between the concrete and the steel core is simulated by using elements TARGE 170 and CONTAC 174. The material properties of the concrete, core plates, and the steel casing are the same as those used in simulation C3 in Section 6.1. The normal penalty stiffness factor, FKN, and friction coefficient are the same as those used in simulation C3 as well.

To evaluate the thickness of the casing, monotonic loading simulation is used for this part of the research. Since the buckling of the casing only happens when the BRB is under compression, the monotonic compressive loading is applied on one end of the core plates and the other end is fixed. The displacement-control mode is used in the simulation. Both axial displacement and lateral displacement perpendicular to the longitudinal axis of BRB are applied on one end of the core plates.

A typical BRB frame before loading is shown in Figure 6.8(a). The interstory height is H_b and the bay width is W_b . When a horizontal displacement Δ_m is applied to the BRB frame, as shown in Figure 6.8 (b), the corresponding perpendicular displacement on the top end of the BRB is Δ_{bm} ; the perpendicular ratio ($\Delta_{bm}/\sqrt{W_b^2 + H_b^2}$) is expressed in Eq. (6.2) in terms of the horizontal interstory drift ratio, defined as the ratio of the horizontal displacement over the interstory height (Δ_m/H_b). AISC-341 (2010) requires the BRB to withstand the displacement which results from a 2% interstory drift ratio (Δ_m/H_b). Assuming that the bay width and the bay

height are the same, the perpendicular ratio on the top end of the BRB in Eq. (6.2) is 0.01 when the interstory story drift ratio (Δ_m/H_b) is 2%.

$$\frac{\Delta_{bm}}{\sqrt{W_b^2 + H_b^2}} = \left(\frac{\Delta_m}{H_b}\right) \left[\frac{1}{1 + \left(\frac{W_b}{H_b}\right)^2} \right] \quad (6.2)$$

This perpendicular ratio on the top end of the BRB is the lateral displacement applied on the core plate in the simulation, which is along the weak axis of the core plates. The lateral displacement applied on the model with the length of 20 ft., 25 ft., 30 ft., 40 ft., 50 ft., and 60 ft. was 2.4 in., 3 in., 3.6 in., 4.8 in., 6.0 in. and 7.2 in., respectively.

Watanabe et al. (1988) suggested that the buckling force resisted by the casing should be greater than 1.5 times the yield force of the core plate, to prevent global buckling of the casing. Therefore, the axial displacement which can make the axial force of the BRB 1.5 times the yield force of the core plates is applied on each BRB. The BRB model was simulated with 1.5 times the yield force for the core plates to obtain the axial displacement. The axial displacement applied on the model with the length of 20 ft., 25 ft., 30 ft., 40 ft., 50 ft., and 60 ft. was 8.4 in., 10.5 in., 12.6 in., 16.8 in., 21.0 in., and 25.2 in., respectively.

The ratio of horizontal force to axial force on the loading surface of the core plate is considered a form of eccentricity. The eccentricity versus the BRB length for casing cross-sections of 12 in. \times 12 in., 14 in. \times 14 in., and 16 in. \times 16 in. are plotted in Figures 6.9 through 6.11, respectively. Tables 6.16 through 6.18 list the corresponding data for Figures 6.9 through 6.11. The wall thicknesses of 3/16 in., 1/4 in., 5/16 in., and 3/8 in. for the 12 in. \times 12 in. casing are not working for BRB length of 60 ft. since the

corresponding models always buckle before the simulations end. The plot of force vs. displacement and the deformation are shown in Figure 6.12 for the 60-ft-long BRB with a cross-sectional dimension of 12 in. \times 12 in. \times 0.1875 in. for the casing. For the same reason, the wall thickness of 3/16 in. for 12 in. \times 12 in. casing is not working for 50-ft.-long BRB. From Figures 6.9 through 6.11, it can be seen that the eccentricity that can be tolerated decreases as the length of BRB increases. For BRBs with the same length and same cross-section of the casing, the tolerable eccentricity increases when the wall thickness increases. From the relationship between the eccentricity and the length of BRB, the minimum wall thickness of casing can be found for certain length of BRB without global buckling occurring on the casing when the performance of BRB is required to meet the 2% of interstory drift requirement of AISC-341 (2010).

The relationship between the casing wall thickness and the BRB length according to Watanabe et al. (1988) is plotted in Figure 6.13. 12 in. \times 12 in., 14 in. \times 14 in., and 16 in. \times 16 in. are used for the cross-section of the casing. According to AISC, wall thicknesses of HSS for the cross-section of 12 in. \times 12 in. are 3/16 in., 1/4 in., 5/16 in., 3/8 in., 1/2 in., and 5/8 in., and wall thicknesses of HSS for the cross-section of the 14 in. \times 14 in. and 16 in. \times 16 in. are 5/16 in., 3/8 in., 1/2 in., and 5/8 in., respectively. Therefore, any thicknesses below 3/16 in. and above 5/8 in. for casing cross-section of 12 in. \times 12 in. are plotted in dotted line, and any thicknesses below 5/16 in. and above 5/8 in. for casing cross-section of 14 in. \times 14 in. and 16 in. \times 16 in. are plotted in dotted line as well.

For example, when the BRB is 40 ft. long, and the cross-section of the casing is 12 in. \times 12 in., the required wall thickness is 1/4 in. according to the simulation result but

5/8 in. according to Watanabe et al. (1988). It can be seen that compared to the wall thickness obtained in the simulation and that obtained from Watanabe et al. (1988), BRBs with a given length need thinner steel casing according to the simulation result, and thicker steel casing according to Watanabe et al. (1988). Therefore, the theory of Watanabe et al. (1988) about the wall thickness of steel casing is more conservative.

Table 6.1
The material property for each BRB component

| Parts | Material property |
|--------------|--|
| Concrete | Bilinear isotropic hardening, E=3605 ksi, Tangent modulus is 0 |
| Core | Combination of the multilinear isotropic and the nonlinear kinematic |
| steel casing | Bilinear isotropic hardening, E=29 msi, Tangent modulus is 210ksi. |

Table 6.2
The simulation models

| Model # | Test # | Casing size, in. | Core plate, in. |
|---------|--------|------------------|-----------------|
| C1 | Test1 | 12x12x0.25 | 9.25x2x123 |
| C2 | Test2 | 12x12x0.25 | 9.25x2x123 |
| C3 | Test3 | 12x12x0.25 | 6.25x2x135 |
| C4 | Test4 | 12x12x0.25 | 9.25x2x123 |
| C5 | Test5 | 12x12x0.25 | 10x1x153 |
| C6 | Test6 | 10x10x0.25 | 7.75x1x157 |
| C7 | Test7 | 10x10x0.25 | 7.75x1x157 |
| C8 | Test8 | 10x10x0.25 | 7.75x1x157 |
| C9 | Test9 | 12x12x0.25 | 10x1x153 |

Table 6.3
The parameters for combination of multilinear isotropic and nonlinear kinematic in model C1

| Nonlinear kinematic | | | | Multilinear isotropic | | | |
|----------------------|---------|------------|-------|-----------------------|-------|--------------|-------|
| $\sigma_y=30600$ psi | | | | $\sigma_y=30600$ psi | | | |
| parameters | Value | parameters | value | parameters | value | parameters | value |
| C_1 | 4025900 | r_1 | 500 | σ_1 | 30600 | ϵ_1 | 0 |
| C_2 | 3545700 | r_2 | 375 | σ_2 | 37800 | ϵ_2 | 0.05 |
| C_3 | 1602900 | r_3 | 120 | σ_3 | 41800 | ϵ_3 | 0.1 |
| C_4 | 305610 | r_4 | 25 | σ_4 | 59800 | ϵ_4 | 1 |
| C_5 | 43510 | r_5 | 0 | FKN= | 0.05 | | |

Table 6.4
The parameters for combination of multilinear isotropic and nonlinear kinematic in model C2

| Nonlinear kinematic | | | | Multilinear isotropic | | | |
|----------------------|---------|------------|-------|-----------------------|-------|-----------------|-------|
| $\sigma_y=29000$ psi | | | | $\sigma_y=29000$ psi | | | |
| parameters | value | parameters | value | parameters | value | parameters | value |
| C_1 | 4025900 | r_1 | 500 | σ_1 | 29000 | ε_1 | 0 |
| C_2 | 3545700 | r_2 | 375 | σ_2 | 39000 | ε_2 | 0.05 |
| C_3 | 1602900 | r_3 | 120 | σ_3 | 41800 | ε_3 | 0.1 |
| C_4 | 305610 | r_4 | 25 | σ_4 | 59800 | ε_4 | 1 |
| C_5 | 43510 | r_5 | 0 | FKN= | 0.05 | | |

Table 6.5
The parameters for combination of multilinear isotropic and nonlinear kinematic in model C3

| Nonlinear kinematic | | | | Multilinear isotropic | | | |
|----------------------|---------|------------|-------|-----------------------|-------|-----------------|-------|
| $\sigma_y=33000$ psi | | | | $\sigma_y=33000$ psi | | | |
| parameters | Value | parameters | value | parameters | value | parameters | value |
| C_1 | 4025900 | r_1 | 500 | σ_1 | 30600 | ε_1 | 0 |
| C_2 | 3545700 | r_2 | 375 | σ_2 | 37800 | ε_2 | 0.05 |
| C_3 | 1602900 | r_3 | 120 | σ_3 | 41800 | ε_3 | 0.1 |
| C_4 | 305610 | r_4 | 25 | σ_4 | 59800 | ε_4 | 1 |
| C_5 | 43510 | r_5 | 0 | FKN= | 0.05 | | |

Table 6.6
The parameters for combination of multilinear isotropic and nonlinear kinematic in model C4

| Nonlinear kinematic | | | | Multilinear isotropic | | | |
|----------------------|---------|------------|-------|-----------------------|-------|-----------------|-------|
| $\sigma_y=29000$ psi | | | | $\sigma_y=29000$ psi | | | |
| parameters | value | parameters | value | parameters | value | parameters | value |
| C_1 | 4025900 | r_1 | 500 | σ_1 | 29000 | ε_1 | 0 |
| C_2 | 3545700 | r_2 | 375 | σ_2 | 39000 | ε_2 | 0.05 |
| C_3 | 1602900 | r_3 | 120 | σ_3 | 41800 | ε_3 | 0.1 |
| C_4 | 305610 | r_4 | 25 | σ_4 | 59800 | ε_4 | 1 |
| C_5 | 43510 | r_5 | 0 | FKN= | 0.05 | | |

Table 6.7
The parameters for combination of multilinear isotropic and nonlinear kinematic in model C5

| Nonlinear kinematic | | | | Multilinear isotropic | | | |
|----------------------|---------|------------|-------|-----------------------|-------|-----------------|-------|
| $\sigma_y=40000$ psi | | | | $\sigma_y=40000$ psi | | | |
| parameters | Value | parameters | value | parameters | value | parameters | value |
| C_1 | 4025900 | r_1 | 500 | σ_1 | 40000 | ε_1 | 0 |
| C_2 | 3545700 | r_2 | 375 | σ_2 | 46000 | ε_2 | 0.05 |
| C_3 | 1602900 | r_3 | 120 | σ_3 | 50000 | ε_3 | 0.1 |
| C_4 | 505610 | r_4 | 25 | σ_4 | 70000 | ε_4 | 1 |
| C_5 | 53510 | r_5 | 0 | FKN= | 0.1 | | |

Table 6.8
The parameters for combination of multilinear isotropic and nonlinear kinematic in model C6

| Nonlinear kinematic | | | | Multilinear isotropic | | | |
|----------------------|---------|------------|-------|-----------------------|-------|-----------------|-------|
| $\sigma_y=36000$ psi | | | | $\sigma_y=36000$ psi | | | |
| parameters | Value | parameters | value | parameters | value | parameters | value |
| C_1 | 4025900 | r_1 | 500 | σ_1 | 36000 | ε_1 | 0 |
| C_2 | 3545700 | r_2 | 375 | σ_2 | 44000 | ε_2 | 0.05 |
| C_3 | 1602900 | r_3 | 120 | σ_3 | 48000 | ε_3 | 0.1 |
| C_4 | 505610 | r_4 | 25 | σ_4 | 70000 | ε_4 | 1 |
| C_5 | 53510 | r_5 | 0 | FKN= | 0.2 | | |

Table 6.9
The parameters for combination of multilinear isotropic and nonlinear kinematic in model C7

| Nonlinear kinematic | | | | Multilinear isotropic | | | |
|----------------------|---------|------------|-------|-----------------------|-------|-----------------|-------|
| $\sigma_y=36000$ psi | | | | $\sigma_y=36000$ psi | | | |
| parameters | Value | parameters | value | parameters | value | parameters | value |
| C_1 | 4025900 | r_1 | 500 | σ_1 | 36000 | ε_1 | 0 |
| C_2 | 3545700 | r_2 | 375 | σ_2 | 44000 | ε_2 | 0.05 |
| C_3 | 1602900 | r_3 | 120 | σ_3 | 48000 | ε_3 | 0.1 |
| C_4 | 505610 | r_4 | 25 | σ_4 | 70000 | ε_4 | 1 |
| C_5 | 53510 | r_5 | 0 | FKN= | 0.2 | | |

Table 6.10
The parameters for combination of multilinear isotropic and
nonlinear kinematic in model C8

| Nonlinear kinematic | | | | Multilinear isotropic | | | |
|----------------------|---------|------------|-------|-----------------------|-------|-----------------|-------|
| $\sigma_y=30600$ psi | | | | $\sigma_y=30600$ psi | | | |
| parameters | Value | parameters | value | parameters | value | parameters | value |
| C_1 | 4025900 | r_1 | 500 | σ_1 | 30600 | ε_1 | 0 |
| C_2 | 3545700 | r_2 | 375 | σ_2 | 38000 | ε_2 | 0.05 |
| C_3 | 1602900 | r_3 | 120 | σ_3 | 41800 | ε_3 | 0.1 |
| C_4 | 305610 | r_4 | 25 | σ_4 | 59800 | ε_4 | 1 |
| C_5 | 43510 | r_5 | 0 | FKN= | 0.2 | | |

Table 6.11
The parameters for combination of multilinear isotropic and
nonlinear kinematic in model C9

| Nonlinear kinematic | | | | Multilinear isotropic | | | |
|----------------------|---------|------------|-------|-----------------------|-------|-----------------|-------|
| $\sigma_y=30600$ psi | | | | $\sigma_y=30600$ psi | | | |
| parameters | Value | parameters | value | parameters | value | parameters | value |
| C_1 | 4025900 | r_1 | 500 | σ_1 | 30600 | ε_1 | 0 |
| C_2 | 3545700 | r_2 | 375 | σ_2 | 38000 | ε_2 | 0.05 |
| C_3 | 1602900 | r_3 | 120 | σ_3 | 41800 | ε_3 | 0.1 |
| C_4 | 305610 | r_4 | 25 | σ_4 | 59800 | ε_4 | 1 |
| C_5 | 43510 | r_5 | 0 | FKN= | 0.1 | | |

Table 6.12
The energy dissipation for the BRB obtained in the
simulation and in the tests1, 2 and 4

| Step | Test1 PB750 | Sim.C1 | Diff.% | Test2 PB750 | Sim. | Diff.% | Test4 PW750 | Sim. | Diff. % |
|--------------|----------------|---------------|----------|----------------|--------------|----------|----------------|--------------|------------|
| 1 | 120 | 132 | 10 | 325 | 359 | 10 | 117 | 197 | 68 |
| 2 | 2341 | 2041 | -13 | 2097 | 2073 | -1 | 2573 | 2482 | -4 |
| 3 | 6462 | 6376 | -1 | 6005 | 6504 | 8 | 7204 | 7738 | 7 |
| 4 | 11690 | 11825 | 1 | 10993 | 11900 | 8 | 13249 | 13810 | 4 |
| 5 | 17405 | 17326 | 0 | 16511 | 17354 | 5 | 20035 | 20128 | 0 |
| 6 | 25923 | 25169 | -3 | 24865 | 25234 | 1 | 27428 | 27199 | -1 |
| 7 | 34390 | 34349 | 0 | 20097 | 20022 | 0 | 11960 | 9006 | -25 |
| 8 | 15688 | 22031 | 40 | | | | | | |
| total | 114019 | 119249 | 5 | 80893 | 83446 | 3 | 82566 | 80560 | -2 |

Table 6.13
The energy dissipation for the BRB
obtained in the simulation
and the test 3

| Step | Test3 PB500 | Sim.C2 | Diff.% |
|--------------|----------------|-----------------|-----------|
| 1 | 145 | 224 | 54 |
| 2 | 1342 | 1442 | 7 |
| 3 | 3952 | 4363 | 10 |
| 4 | 7336 | 8014 | 9 |
| 5 | 11098 | 11696 | 5 |
| 6 | 16746 | 16990 | 1 |
| 7 | 16488 | 11411 | -31 |
| total | 57107 | 54139.89 | -5 |

Table 6.14
The energy dissipation for the BRB obtained in
the simulation and the tests 5 and 9

| Step | Test5 PW400 | Sim.C3 | Diff.% | Test9 PW400 | Sim.C3 | Diff.% |
|--------------|----------------|--------------|-----------|----------------|--------------|-----------|
| 1 | 468 | 199 | -58 | 497 | 288 | -42 |
| 2 | 2093 | 1749 | -16 | 2005 | 1608 | -20 |
| 3 | 5421 | 5279 | -3 | 4943 | 4696 | -5 |
| 4 | 9378 | 9432 | 1 | 8450 | 8329 | -1 |
| 5 | 13729 | 13885 | 1 | 12634 | 12193 | -3 |
| 6 | 18650 | 18725 | 0 | 17600 | 16538 | -6 |
| 7 | 11588 | 11405 | -2 | 16345 | 15203 | -7 |
| total | 61327 | 60674 | -1 | 62474 | 58855 | -6 |

Table 6.15
The energy dissipation for the BRB obtained in the
simulation and the tests 6 through 8

| Step | Test6 PB315 | Sim. | Diff. % | Test7 PB315 | Sim. | Diff. % | Test8 PB315 | Sim. | Diff. % |
|--------------|----------------|--------------|------------|----------------|--------------|------------|----------------|--------------|------------|
| 1 | 326 | 192 | -41 | 268 | 279 | 4 | 282 | 222 | -21 |
| 2 | 1573 | 1418 | -10 | 1441 | 1431 | -1 | 1410 | 1340 | -5 |
| 3 | 4062 | 4271 | 5 | 3947 | 4273 | 8 | 3733 | 3904 | 5 |
| 4 | 7163 | 7639 | 7 | 6961 | 7639 | 10 | 6643 | 6915 | 4 |
| 5 | 10908 | 11256 | 3 | 10559 | 11256 | 7 | 9991 | 10080 | 0 |
| 6 | 16585 | 16301 | -2 | 15804 | 16301 | 3 | 11836 | 12238 | -4 |
| 7 | 8946 | 9139 | 2 | 1675 | 1561 | -7 | | | |
| total | 49563 | 50215 | 1 | 40654 | 42741 | 5 | 33895 | 34697 | 2 |

Table 6.16.
The ratio of lateral force to axial capacity of BRB for casing
cross-sectional dimension of 12 in. × 12 in.

| Wall thickness, in. | Length of BRB, ft. | Lateral force, Kips | BRB Capacity, Kips | Ratio of lateral force to BRB Capacity, (%) |
|---------------------|--------------------|---------------------|--------------------|---|
| 3/16 | 20 | 0.115 | 621.845 | 0.019 |
| | 25 | 0.053 | 621.632 | 0.008 |
| | 30 | 0.026 | 621.440 | 0.004 |
| | 40 | | | - |
| | 50 | | | - |
| | 60 | | | - |
| 1/4 | 20 | 0.385 | 620.165 | 0.062 |
| | 25 | 0.063 | 619.946 | 0.010 |
| | 30 | 0.033 | 619.850 | 0.005 |
| | 40 | 0.013 | 619.666 | 0.002 |
| | 50 | 0.006 | 619.501 | 0.001 |
| | 60 | | | - |
| 5/16 | 20 | 1.112 | 627.357 | 0.177 |
| | 25 | 0.074 | 627.130 | 0.012 |
| | 30 | 0.041 | 627.033 | 0.006 |
| | 40 | 0.015 | 626.855 | 0.002 |
| | 50 | 0.007 | 626.486 | 0.001 |
| | 60 | | | - |
| 3/8 | 20 | 1.945 | 628.631 | 0.309 |
| | 25 | 0.088 | 628.397 | 0.014 |
| | 30 | 0.048 | 628.296 | 0.008 |
| | 40 | 0.018 | 628.090 | 0.003 |
| | 50 | 0.008 | 628.040 | 0.001 |
| | 60 | | | - |
| 1/2 | 20 | 3.491 | 634.122 | 0.550 |
| | 25 | 0.120 | 633.884 | 0.019 |
| | 30 | 0.061 | 633.779 | 0.010 |
| | 40 | 0.022 | 633.615 | 0.004 |
| | 50 | 0.010 | 633.586 | 0.002 |
| | 60 | 0.006 | 633.322 | 0.001 |
| 5/8 | 20 | 5.133 | 629.154 | 0.816 |
| | 25 | 8.859 | 628.899 | 1.409 |
| | 30 | 0.072 | 628.791 | 0.011 |
| | 40 | 0.026 | 628.580 | 0.004 |
| | 50 | 0.012 | 628.569 | 0.002 |
| | 60 | 0.006 | 628.447 | 0.001 |

Table 6.17
 The ratio of lateral force to axial capacity of BRB for casing
 cross-sectional dimension of 14 in. × 14 in.

| Wall thickness, in. | Length of BRB, ft. | Lateral force, Kips | BRB Capacity, Kips | Ratio of lateral force to BRB Capacity, (%) |
|---------------------|--------------------|---------------------|--------------------|---|
| 5/16 | 20 | 7.011 | 633.884 | 1.106 |
| | 25 | 1.766 | 633.607 | 0.279 |
| | 30 | 0.093 | 633.479 | 0.015 |
| | 40 | 0.034 | 633.289 | 0.005 |
| | 50 | 0.016 | 633.308 | 0.002 |
| | 60 | 0.008 | 632.962 | 0.001 |
| 3/8 | 20 | 8.484 | 634.081 | 1.338 |
| | 25 | 2.642 | 633.794 | 0.417 |
| | 30 | 0.111 | 633.660 | 0.017 |
| | 40 | 0.040 | 633.463 | 0.006 |
| | 50 | 0.018 | 633.453 | 0.003 |
| | 60 | 0.009 | 633.273 | 0.001 |
| 1/2 | 20 | 8.012 | 635.226 | 1.261 |
| | 25 | 4.311 | 634.918 | 0.679 |
| | 30 | 0.848 | 634.776 | 0.008 |
| | 40 | 0.051 | 634.571 | 0.000 |
| | 50 | 0.022 | 634.548 | 0.003 |
| | 60 | 0.012 | 634.443 | 0.002 |
| 5/8 | 20 | 13.886 | 637.960 | 2.177 |
| | 25 | 5.977 | 637.639 | 0.937 |
| | 30 | 1.877 | 637.492 | 0.295 |
| | 40 | 0.062 | 637.284 | 0.010 |
| | 50 | 0.026 | 637.265 | 0.004 |
| | 60 | 0.015 | 637.143 | 0.002 |

Table 6.18
The ratio of lateral force to axial capacity of BRB for casing
cross-sectional dimension of 16 in. \times 16 in.

| Wall thickness, in. | Length of BRB, ft. | Lateral force, Kips | BRB Capacity, Kips | Ratio of lateral force to BRB Capacity, (%) |
|---------------------|--------------------|---------------------|--------------------|---|
| 5/16 | 20 | 15.837 | 633.422 | 2.500 |
| | 25 | 7.263 | 633.093 | 1.147 |
| | 30 | 2.710 | 632.941 | 0.428 |
| | 40 | 0.069 | 632.726 | 0.011 |
| | 50 | 0.030 | 632.725 | 0.005 |
| | 60 | 0.017 | 632.574 | 0.003 |
| 3/8 | 20 | 18.116 | 629.012 | 2.880 |
| | 25 | 7.263 | 633.093 | 1.147 |
| | 30 | 3.686 | 628.535 | 0.586 |
| | 40 | 0.078 | 628.321 | 0.012 |
| | 50 | 0.035 | 628.340 | 0.006 |
| | 60 | 0.019 | 628.237 | 0.003 |
| 1/2 | 20 | 22.415 | 626.746 | 3.576 |
| | 25 | 11.541 | 626.403 | 1.842 |
| | 30 | 5.598 | 626.252 | 0.894 |
| | 40 | 0.298 | 626.028 | 0.048 |
| | 50 | 0.046 | 626.003 | 0.007 |
| | 60 | 0.023 | 625.910 | 0.004 |
| 5/8 | 20 | 26.548 | 607.150 | 4.373 |
| | 25 | 17.903 | 607.234 | 2.948 |
| | 30 | 7.670 | 605.883 | 1.266 |
| | 40 | 1.127 | 605.452 | 0.186 |
| | 50 | 0.054 | 605.545 | 0.009 |
| | 60 | 0.026 | 605.441 | 0.004 |

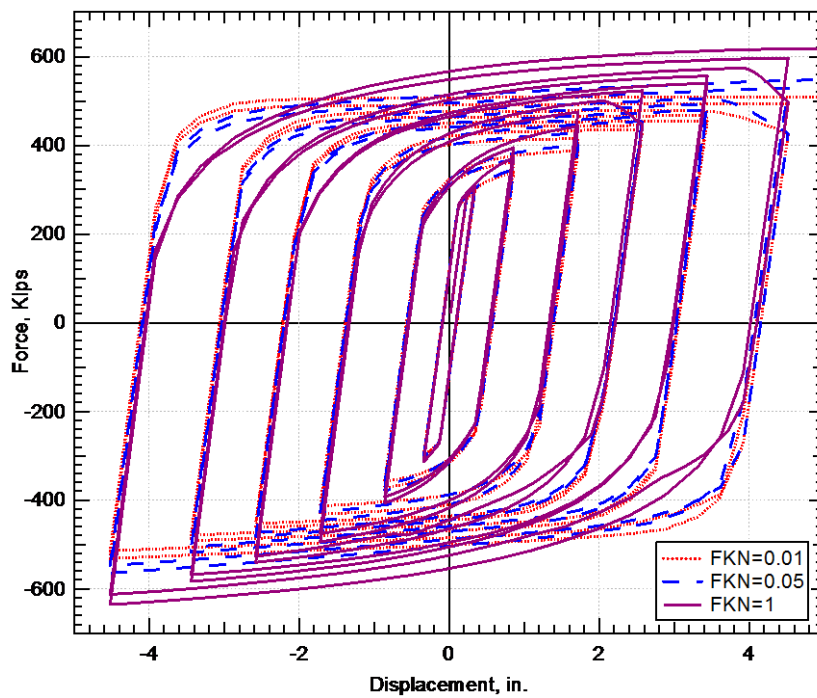


Figure 6.1 Effect of FKN on the shape of the hysteretic loops

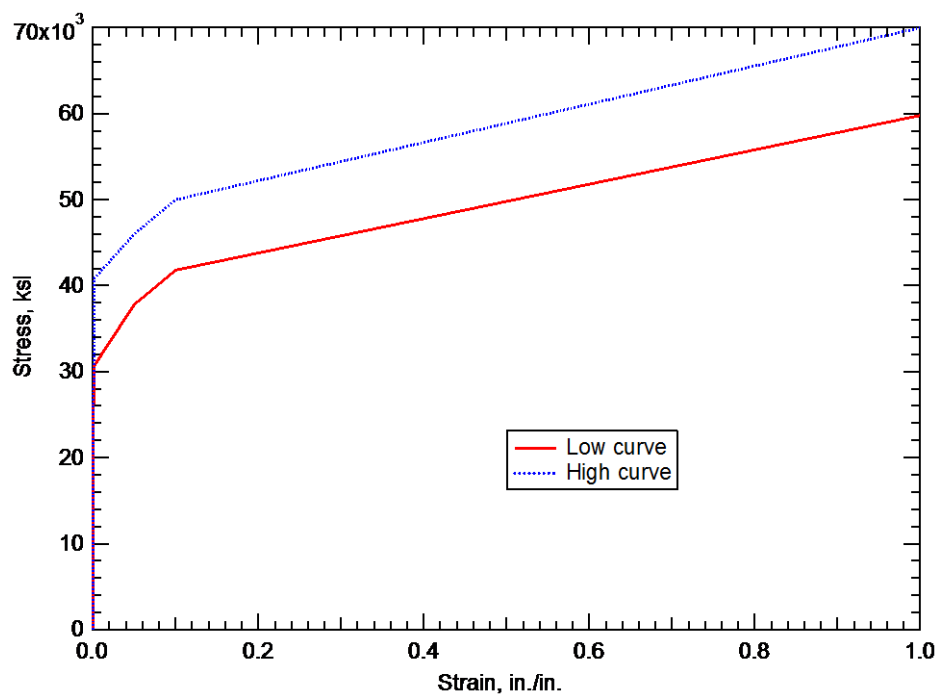


Figure 6.2 Stress-strain curves for isotropic multilinear material property

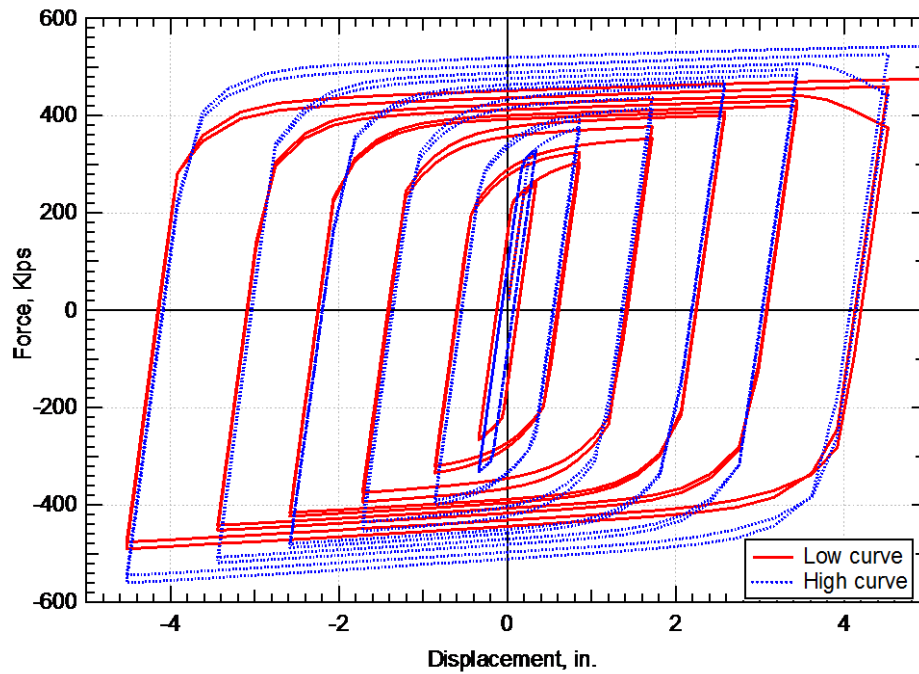


Figure 6.3 Hysteretic loops with two different stress strain curves of multilinear material property

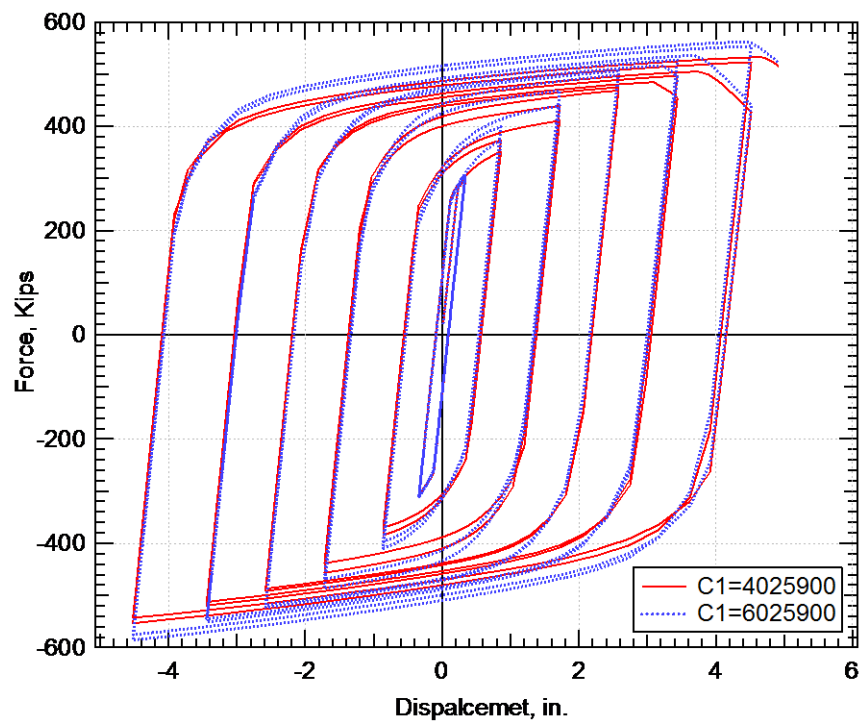


Figure 6.4 Effect of C on the hysteretic loops

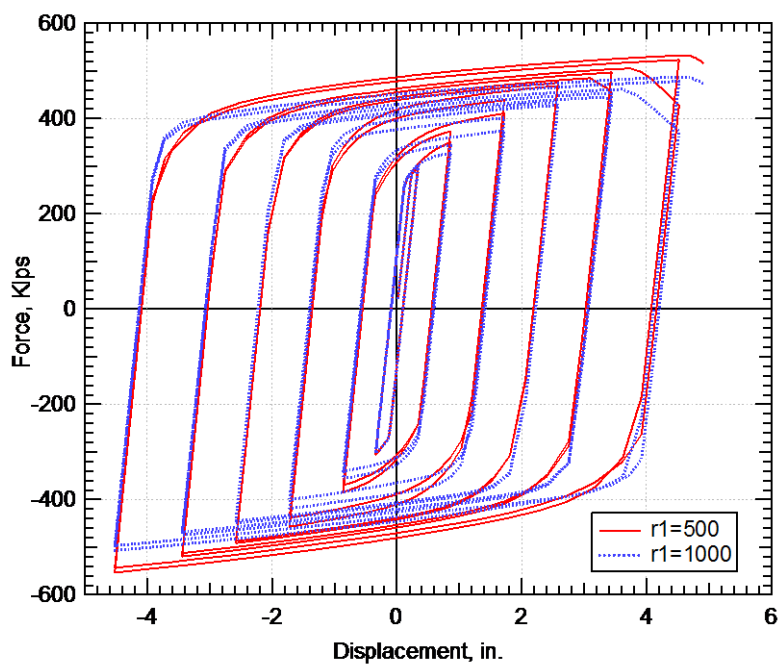


Figure 6.5 Effect of γ on the hysteretic loops

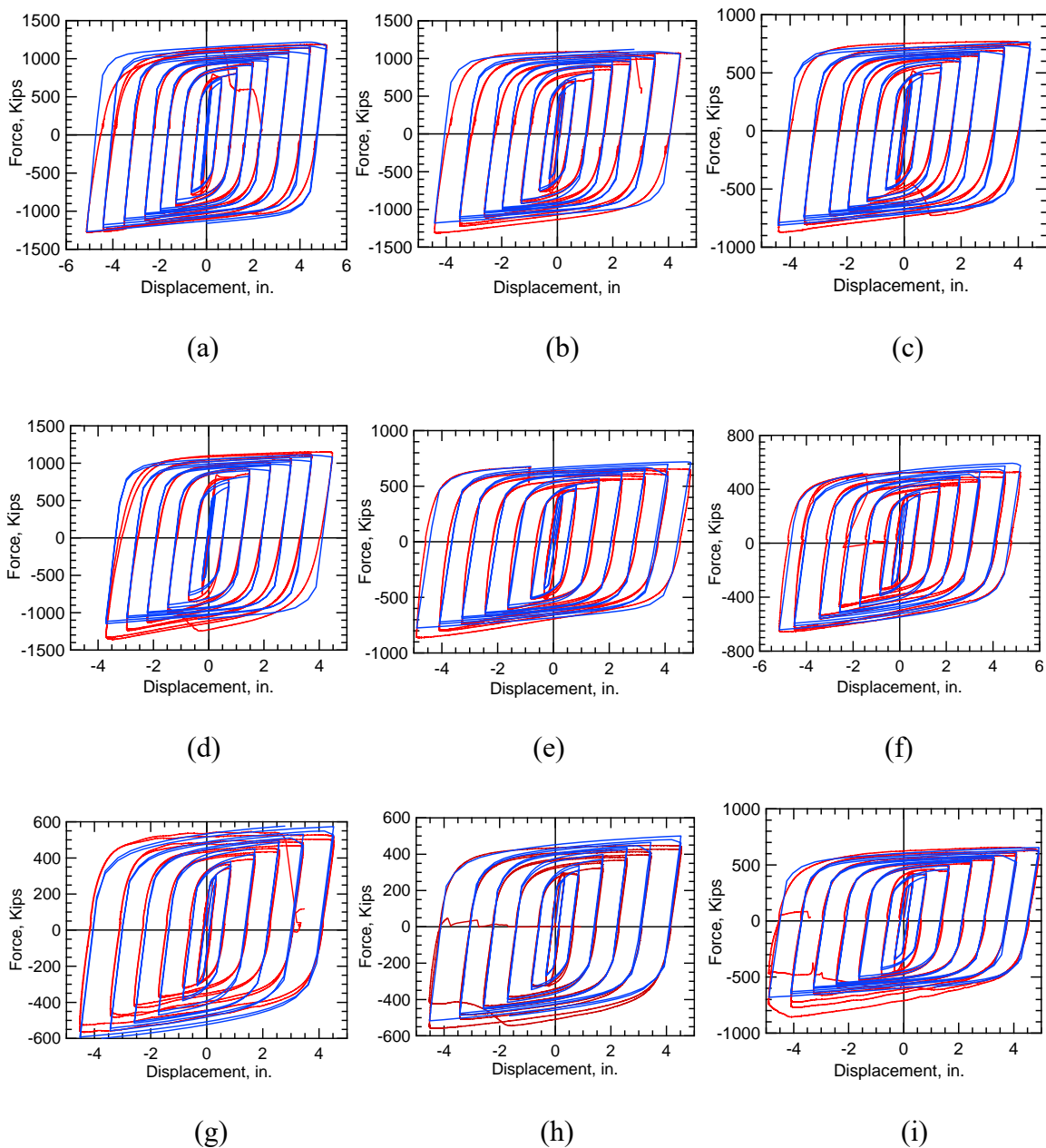
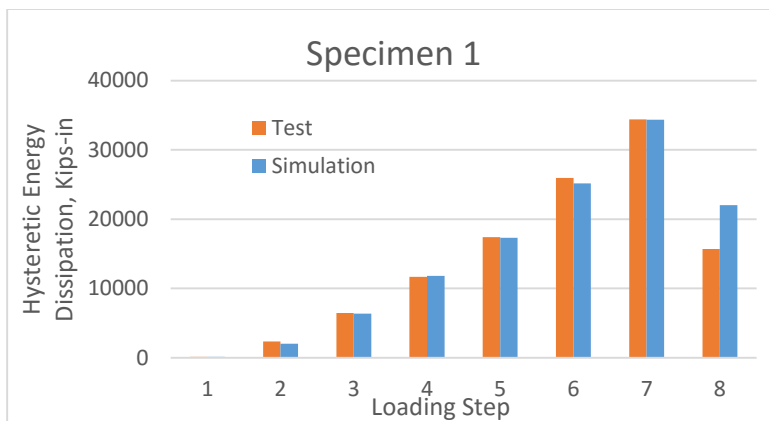
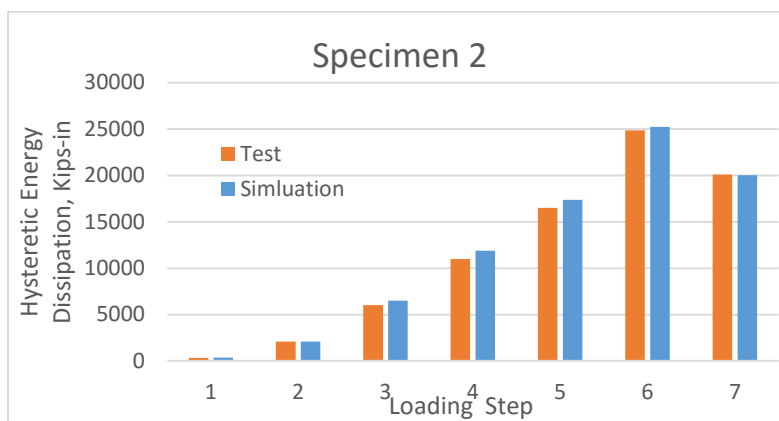


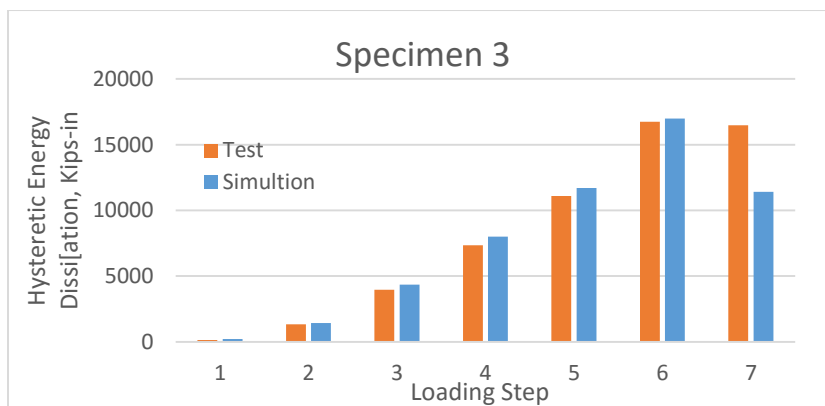
Figure 6.6 Comparison of the hysteretic loops for the simulation and the test results (simulation is in blue and test is in red): (a) Test 1, (b) Test 2, (c) Test3, (d) Test 4, (e) Test 5, (f) Test 6, (g) Test 7, (h) Test 8 and (i) Test 9



(a)

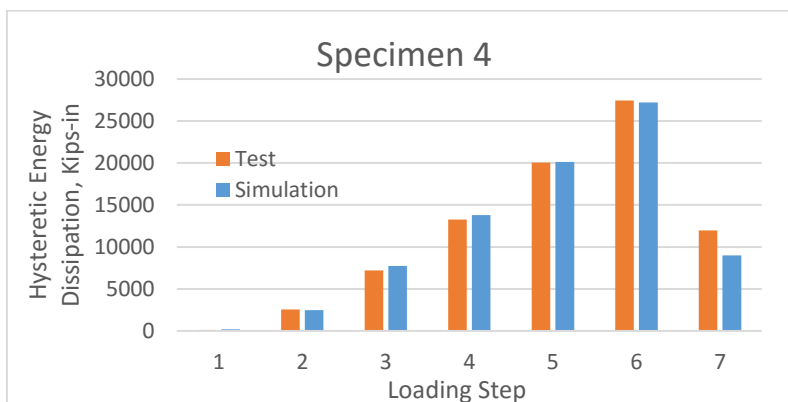


(b)

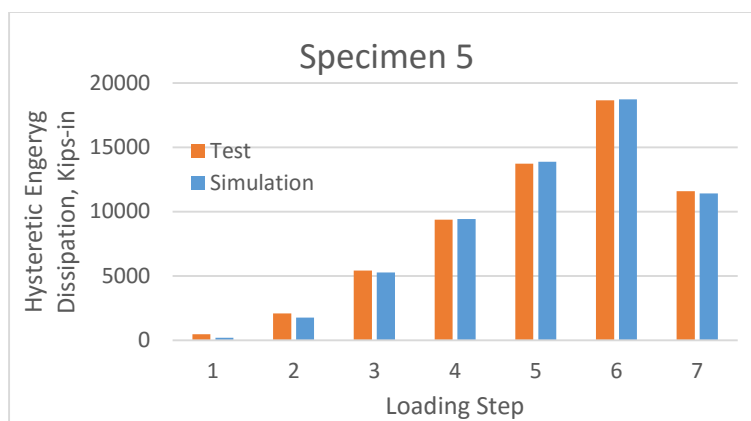


(c)

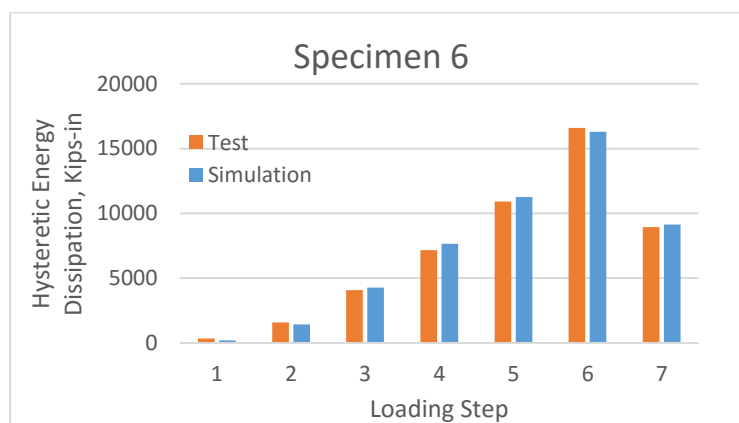
Figure 6.7 Hysteretic energy comparison for simulation result and test result by loading step for the 9 tests: (a) Test 1, (b) Test 2, (c) Test3, (d) Test 4, (e) Test 5, (f) Test 6, (g) Test 7, (h) Test 8 and (i) Test 9



(d)

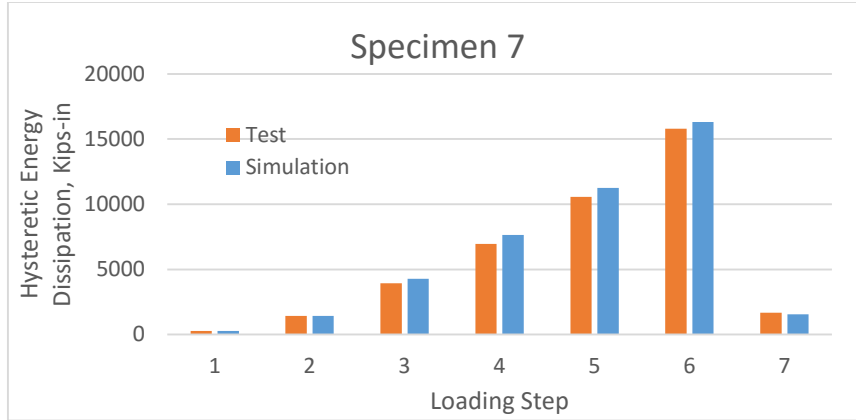


(e)



(f)

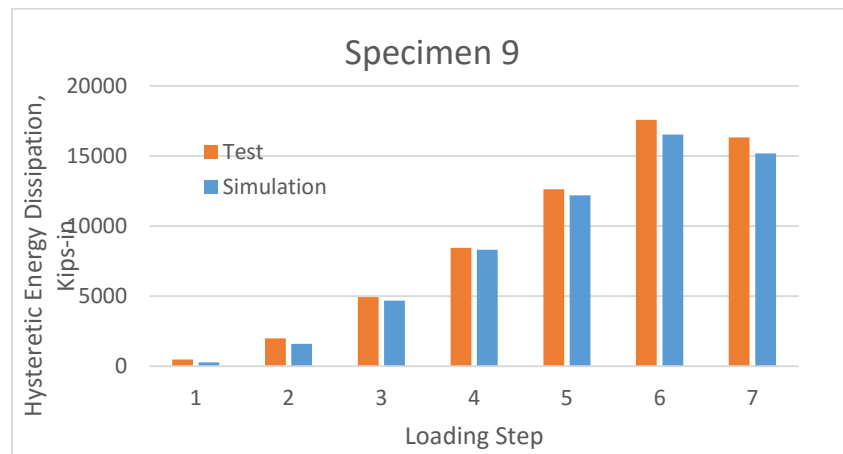
Figure 6.7 Continued



(g)



(h)



(i)

Figure 6.7 Continued

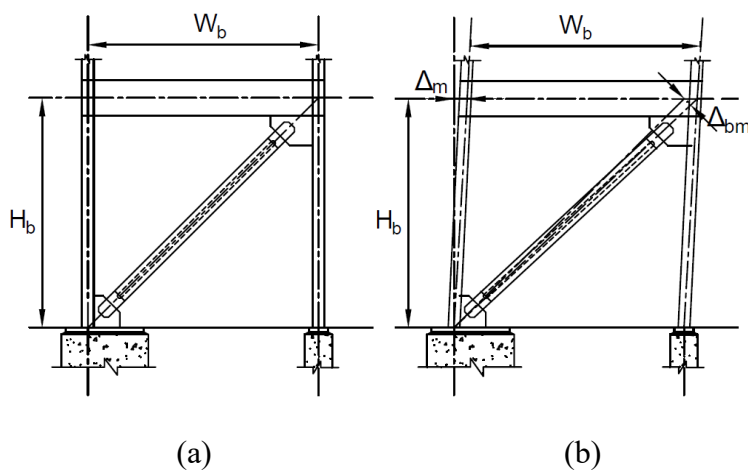


Figure 6.8 Drift of a representative BRB frame:
 (a) Before loading and (b) After loading

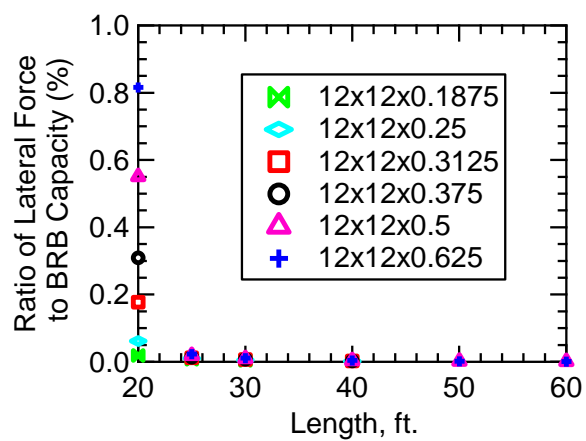


Figure 6.9 Ratio of lateral force to BRB capacity vs. casing length for the BRB with cross-section of 12 in. \times 12 in.

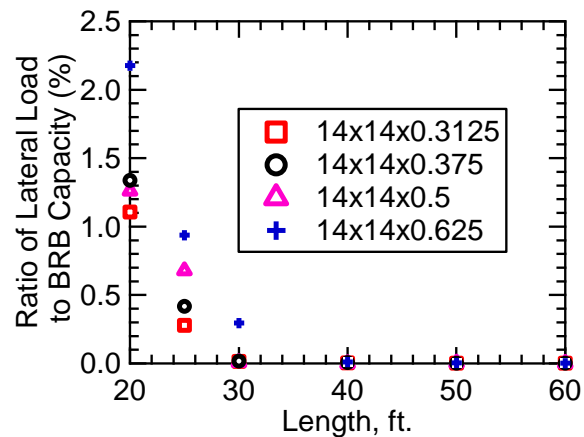


Figure 6.10 Ratio of lateral force to BRB capacity vs. casing length for the BRB with cross-section of 14 in. \times 14 in.

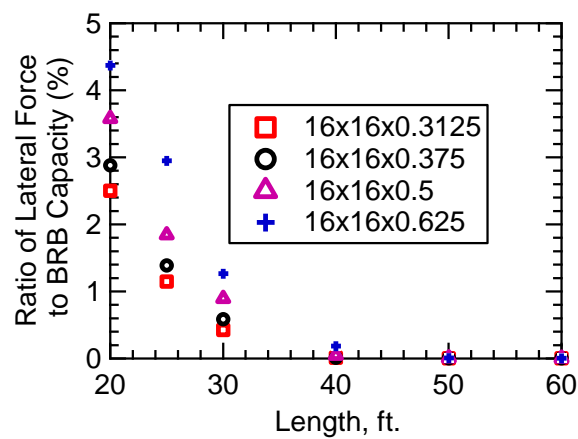
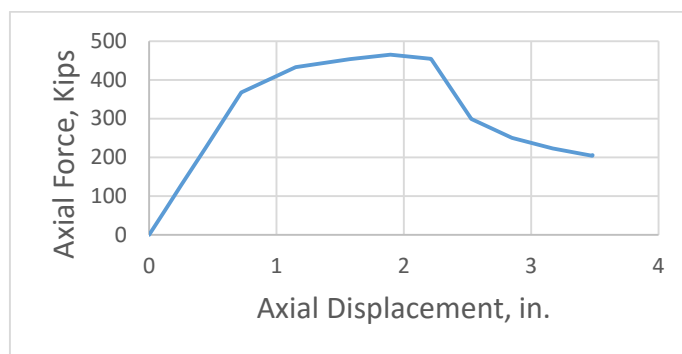
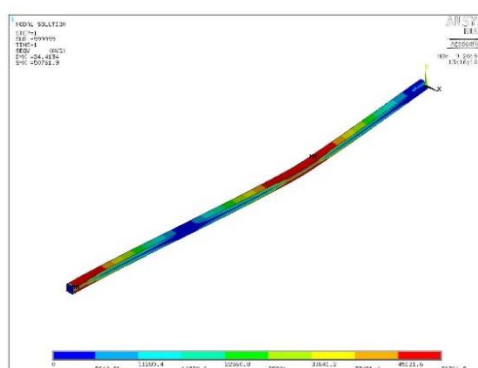


Figure 6.11 Ratio of lateral force to BRB capacity vs. casing length for the BRB with cross-section of 16 in. \times 16 in.



(a)



(b)

Figure 6.12 Buckling performance of a BRB with casing of 60 ft. \times 12 in. \times 12 in. \times 0.1875 in.: (a) Plotting of axial force vs. axial displacement and (b) Deformation and Von misses stress distribution

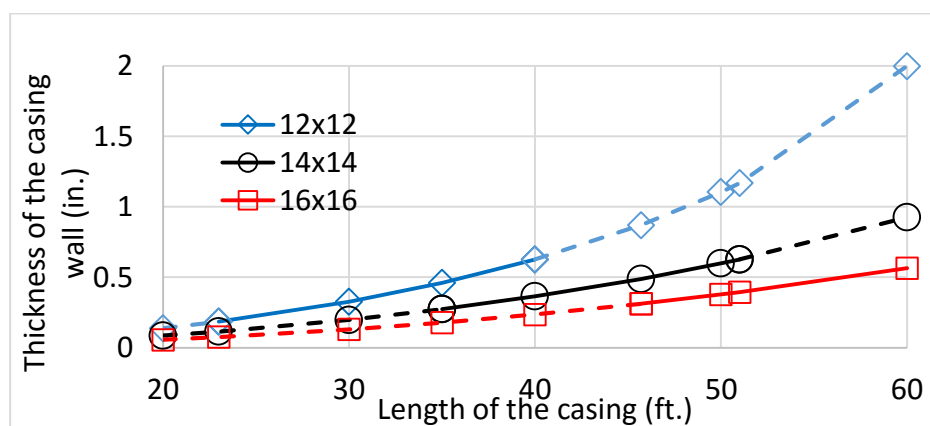


Figure 6.13 Relationship between wall thickness of casing and the BRB length (Watanabe et al. 1988)

CHAPTER 7

ANALYSIS OF GUSSET PLATES

In the laboratory tests, the BRBs were connected to the load frame by using gusset plates. The nine tests were carried out to find the performance of the BRBs with connection plates perpendicular to the core plates. To allow the BRBs to perform to their capacity, the gusset plates and loading frame should not buckle before the BRB fails. During test 4, one top gusset plate buckled in the out-of-plane direction as shown in Figure 3.9 (d). Since the gusset plate buckled, the system failed before the BRB itself reached its capacity.

In actual buildings, BRBs cannot play the role of a “fuse” to protect the frame during an earthquake if the gusset plates fail before the BRBs. Therefore, designing the gusset plate plays an important role in making sure that the BRBs can fully function to their full capacity during an earthquake.

Two different dimensions of gusset plates were used in the laboratory tests. The first set of gusset plates are called “large gusset plates” and the second set are called “small gusset plates” due to the difference in their dimensions. Large gusset plates were used for tests 1 through 4. The top large gusset plates buckled in test 4. After this event, small gusset plates were used for the remaining five tests. Due to this fact, tests 3, 4, and 5 are chosen for further study.

In this section, the load capacity of the two sets of gusset plates is analyzed

following AISC (2011). The design load capacity of the gusset plates is compared to the applied load, which is the maximum tension and maximum compression obtained during the tests. The safety factor for each gusset plate during tests 3, 4, and 5 is calculated. In addition, the finite element method is implemented to analyze the deformation of the gusset plates during tests 3, 4, and 5.

7.1 Code Requirements for Gusset Plate Design

According to the AISC-325 (2011), gusset plates shall be able to resist tension, shear, block shear rupture, compression yielding, and compression buckling. During the tests, only tensile and compressive forces, and moment were applied. Therefore, only the tensile and compressive capacity of the gusset plates is calculated in this section. The calculation method for both design strength (LRFD) and allowable strength (ASD) is described in this section.

7.1.1 Gusset Plates in Tension

Gusset plates subjected to axial tension shall be investigated for two conditions: yielding of the gross section and fracture of the net section. The factored resistance, R_r , for gusset plates in tension shall be taken as the least of the values given by yielding and fracture resistance.

For tensile yielding of gusset plates

$$R_r = \phi_y F_y A_g \quad (7.1)$$

For tensile rupture of gusset plates

$$R_r = \phi_u F_u A_n U \quad (7.2)$$

where ϕ_y is the resistance factor for tension yielding, $\phi_y = 0.9$ (LRFD) and $\phi_y =$

$1/1.67$ (*ASD*); F_y is the yield strength of the plates; A_g is the gross cross-sectional area of the gusset plates; ϕ_u is the resistance factor for tension fracture, $\phi_u = 0.75$ (*LRFD*) and $\phi_u = 1/2$ (*ASD*); F_u is the tensile strength of the gusset plates; A_n is the net cross-sectional area of the gusset plates, which is defined in the AISC specification; U is the shear lag factor, which is determined in AISC (2011) Table D3.1; $U = 1$ for all tension members where the tension load is transmitted directly to each of the cross-sectional elements by fasteners or welds;

For the determination of the gross and net section areas, the effective gross width of the gusset plate in tension may be determined by the Whitmore method. In this method, the effective width is measured across the last row of bolts, which is furthest away from the core, in the gusset plates under consideration. The effective width is bound on either side by the closer of the nearest adjacent plate edges or lines constructed starting from the external fasteners within the first row and extending from these bolts at an angle of 30 degrees with respect to the line of action of the axial force. Figure 7.1 provides an example for determining the effective width in tension in accordance with the Whitmore section method.

7.1.2. Strength of Gusset Plates in Compression

To resist compression yielding and buckling, the strength of the gusset plates in compression has to be calculated. The factored resistance, R_r , for gusset plates in compression shall be taken as the least of the values given by yielding and buckling resistance.

The factored resistance, R_r , can be calculated by using Eq. (7.3) for $KL/r \leq 25$; when $KL/r > 25$, the provisions of Chapter E of AISC-325 (2011) apply.

$$R_r = \phi_c F_y A_g \quad (7.3)$$

where ϕ_c is the resistance factor for compression, $\phi_c = 0.9(LRFD)$ and $\phi_c = 1/1.67(ASD)$.

The effective width of the idealized compression member may be determined in accordance with the Whitmore method. The unbraced length, L , may be determined as the average of three distances (L_1, L_2, L_3). L_1 and L_3 are the distances from each of the ends of the Whitmore width to the first row of fasteners in the closest adjacent member, measured parallel to the line of action of the compressive axial force. When the Whitmore width enters into the adjacent member, the associated distance at that end should be set to zero. L_2 is the distance from the last row of fasteners in the compression member under consideration to the first row of fasteners in the closest adjacent member, measured along the line of action of the compressive axial force. Figure 7.2 gives an example of determining L_1, L_2, L_3 and the effective width for a gusset plate in compression.

The effective length factor, K , can be determined according to Table 7.1. When lateral sway of gusset plates is possible, the value of K can be taken from Table 7.1 case (d), (e) or (f), depending on the buckling shape. When lateral sway of gusset plates is not possible, the effective length factor, K , for gusset plates can be taken from Table 7.1 for cases (a), (b), or (c).

7.2 Calculation of the Design Strength (LRFD) and Allowable Strength (ASD) on the Gusset Plates

There are two dimensions for the gusset plates involved in the tests, as shown in Figure 7.3. The larger gusset plate as shown in Figure 7.3(a) is used for the calculation

example. The calculation for the small gusset plate as shown in Figure 7.3 (b) is attached in the Appendix.

7.2.1 Calculation of the Tensile Yielding Resistance of the Large Gusset Plate

Figure 7.4 shows the effective Whitmore width for the large gusset plate. Since the ideal Whitmore width is larger than the width of the gusset plate, the effective Whitmore width is only taken as the section inside the actual gusset plate provided (Ibrahim 2009), as shown by the red arrow in Figure 7.4.

The width of the widest section of the gusset plate is the summation of $8\frac{13}{16}$ in., $12\frac{1}{8}$ in., and $8\frac{13}{16}$ in., which is 29.75 in. The distance between the widest section of the gusset plate and the bottom row of the bolts is the difference between $(8 \times 2.5 + 2)$ in. and $18\frac{7}{16}$ in., which is 3.5625 in. Therefore, the distance between the effective Whitmore length and the bottom of the gusset plate is $(14\frac{3}{16} - 3.5625)$, which is 10.625 in. Because the two triangles on the bottom of the figure are similar triangles, the edges of these two triangles are proportional. The effective Whitmore length can be obtained by Eq. (7.4).

$$\frac{\text{effective Whitmore length}}{29\frac{3}{4}} = \frac{10.625}{14\frac{3}{16}} \quad (7.4)$$

So the effective Whitmore length = 22.28 in.

The yield strength of the gusset plates is 50 *ksi*. The thickness of the gusset plate is 1.5 in. Therefore, the gross area of the gusset plate subject to tension and the tensile yielding capacity of the gusset plates are calculated as follows:

$$A_g = 1.5 \times 22.28 = 33.42 \text{ in.}^2 \quad (7.5)$$

$$R_r(LRFD) = \phi_y F_y A_g = 0.9 \times 50 \times 33.42 = 1503.9 \text{ kips} \quad (7.6)$$

$$R_r(ASD) = \phi_y F_y A_g = \frac{1}{1.67} \times 50 \times 33.42 = 1000.6 \text{ kips} \quad (7.7)$$

The data obtained in Eqs. (7.6) and (7.7) are listed in the first row of Table 7.2.

7.2.2 Calculation of the Tensile Rupture Resistance of the Large Gusset Plate

The tensile rupture resistance of the gusset plate can be calculated using Eq. (7.2).

The net width of gusset plate for rupture is the effective Whitmore length deducting the total width of the bolt holes. In the tests, $1\frac{1}{8}$ in. diameter bolts were used. The ultimate strength of the gusset plate is 65 *ksi*. The net area of the gusset plate subjected to tensile rupture and the tensile rupture resistance of the gusset plate can be calculated as follows:

$$A_n = 1.5 \times \left[22.28 - 2 \times \left(1 + \frac{1}{8} \right) \right] = 1.5 \times 20.03 = 30.045 \text{ in}^2 \quad (7.8)$$

$$R_r(LRFD) = \phi_u F_u A_n U = 0.75 \times 65 \times 30.045 \times 1 = 1464.69 \text{ kips} \quad (7.9)$$

$$R_r(ASD) = \phi_u F_u A_n U = \frac{1}{2} \times 65 \times 30.045 \times 1 = 976.46 \text{ kips} \quad (7.10)$$

The data obtained in Eqs. (7.9) and (7.10) are listed in the second row of Table 7.2.

7.2.3 Calculation of the Compression Resistance of the Large Gusset Plate

One end of the gusset plate was fixed and the other end of the gusset plate was connected with the connection plates. And the system of the BRB and gusset plates were tested vertically in the lab. According to the observation during test 4, the deformation of the gusset plate under compression is shown in Figure 7.5, which is similar to the deformation when the column is in compression. In this case, the effective length factor *k* value for design should be chosen as 1.2, according to Table 7.1.

Since both ends of the Whitmore width extend outside the gusset plate, the associated distance at both ends should be set to zero. Therefore, $L_1 = L_3 = 0$, as shown in Figure 7.6. The distance from the last row of the bolts in to the bottom of the gusset plate, L_2 , is 10.625 in., which was obtained in Section 7.2.1. The slenderness of the gusset plate, KL/r , can be calculated as follows:

$$r = \sqrt{\frac{I_g}{A_g}} = \sqrt{\frac{22.28 \times 1.5^3 / 12}{22.28 \times 1.5}} = 0.433 \quad (7.11)$$

$$L = \frac{L_1 + L_2 + L_3}{3} = \frac{0 + 10.625 + 0}{3} = 3.54 \text{ in.} \quad (7.12)$$

$$\frac{KL}{r} = \frac{1.2 \times 3.54}{0.433} = 9.81 \quad (7.13)$$

Since $KL/r \leq 25$, the compressive resistance of the gusset plate subjected to yielding and buckling can be calculated by using Eq. (7.3). The compressive resistance of the gusset plate is calculated as follows:

$$R_r(LRFD) = \phi_c F_y A_g = 0.9 \times 50 \times 22.28 \times 1.5 = 1503.9 \text{ kips} \quad (7.14)$$

$$R_r(ASD) = \phi_c F_y A_g = \frac{1}{1.67} \times 50 \times 22.28 \times 1.5 = 1000.62 \text{ kips} \quad (7.15)$$

Data obtained in Eqs. (7.14) and (7.15) are listed in the third row of Table 7.2. Similar calculations for the small gusset plates are shown in the Appendix. A comparison of the resistance of the large gusset plate and the applied load for tests 3 and 4 is listed in Table 7.2. A comparison of the resistance of the small gusset plate and the applied load for test 5 is listed in Table 7.3. The applied loads for tension and compression are the maximum tension and compression obtained during the tests, respectively. The safety factor is the ratio of the resistance to the applied load. It can be seen that the safety factor of the large gusset plate in test 3 is larger than 1.00. The safety factor of the large gusset plate in test 4 and that of the small gusset plate in test 5 are similar and are less than 1.00

for tensile yielding, tensile rupture, and compression. The small gusset plate in test 5 even has a smaller safety factor in compression than the large gusset plate in test 4. However, the large gusset plate in test 4 buckled, while the small gusset plate in test 5 was stable. Further research using the finite element method is done to explain this phenomenon.

7.3 FEM Simulation of the Top Gusset Plate with Connection Plates in ANSYS

Due to the out-of-plane buckling which occurred at the top gusset plate in test 4, the top gusset plate with partial connection plates is the focus of this section.

The gusset plate and connection plates for tests 3, 4, and 5 are simulated using FEM with ANSYS. In tests 3 and 4 the large gusset plate was used, and in test 5 the small gusset plate was used. The dimensions of the large and small gusset plates are shown in Figure 7.3. The element SOLID 186 is used for both connection plates and gusset plates. Bilinear isotropic hardening material properties are used for both the gusset plate and connection plates.

The connection plates and the gusset plate share the same nodes where they come into contact because there was no relative movement between the gusset plate and connection plates during the tests. The bolts or welds are ignored since the boundary conditions between the gusset plates and connection plates are simplified. The connection plates are simplified as rectangular plates in the model. The details of the models for the combination of the gusset plate and connection plates are listed in Table 7.4.

During the tests, axial cyclic loading was applied to the BRBs through the actuator and load cell to the gusset plates. Theoretically, the whole BRB system,

including the load cell, gusset plate, and BRB, experienced the same amount of load as recorded by the data acquisition system. This cyclic load is applied on the gusset plate in the simulation as the input load. A value of 1% of the axial load will also be applied on the gusset plate in the weak-axis direction as eccentricity. The three models for tests 3, 4, and 5 with the load applied are shown in Figure 7.7.

7.4 Comparison among the Simulation Results

The deformation of the gusset plate and the connection plates for the three models is shown in Figure 7.8. The Von Misses stress distributions for these three models are shown in Figure 7.9. The deflections of the gusset plate are -0.055 in, -0.178 in., and 0.018 in. in the simulation for tests 3, 4, and 5, respectively. In the simulation, stress concentration occurred on the top of the connection plate in the model #GC2 of test 4 and the connection plates deformed significantly.

The actual test load (1357.66 kip) applied to the model for test 4 was applied much greater than that for the model of test 3 (870.82 kips) and test 5 (861.67 kips); this is one of the reasons why the model for test 4 has larger deflection than the other two models. Besides the load, the model for test 4 has 0.75-in.-thick connection plates, the model for test 3 has 1.5-in.-thick connection plates, and the model for test 6 has 1-in.-thick connection plates. This is another reason why the model for test 4 has the largest deflection and the gusset/connection plates failure compared to the other two models. Comparing the safety factor listed in Tables 7.2 and 7.3, it can be seen that even though the small gusset plate used in test 5 had the smallest safety factor for compression resistance, the deflection of this model during the simulation had the smallest deflection. When calculating the resistant capacity of the gusset plates, only the geometry of the

gusset plates was considered. However, in the simulation, both connection plates and the gusset plate are involved. That means that geometry of the connection plates has an influence on the stiffness of the gusset/connection plate end system of load transferred to the BRB.

To obtain the effect of the connection plates on the compression resistance of the gusset/connection plate end system, a gusset plate with a larger thickness is simulated. Based on the connection plate for test 4, a 1.5-in.-thick connection plate is used instead of the 0.75-in.-thick connection plate, and the remaining dimensions of the connection plates remain the same. Therefore, the dimensions of the connection plates for the new model are 1.5 in. \times 10 in. \times 24 in. The same load is used for this model as that for the previous model for test 4. The deformation of the gusset plate and connection plates for this model is shown in Figure 7.10. The deflection of the gusset plate for this model is – 0.063 in., which is one third of deflection of the gusset plate in the model which has 0.75-in.-thick connection plates, and the connection plate does not buckle in the simulation.

From the simulation results, it can be seen that the dimensions of both the gusset plate and the connection plates determine the out-of-plane buckling behavior of the gusset plate. When the applied load is smaller than or equal to the capacity of the gusset plate, the gusset plate can resist the deflection by itself. When the applied load is larger than the capacity of the gusset plate, the connection plates can help to increase the effective stiffness of the gusset plate to reduce the deflection and prevent out-of-plane buckling.

Table 7.1
The effective length factor, K (Table C-A-7.1. ANSI/AISC 360-10 2010)







| Buckled shape | (a) | (b) | (c) | (d) | (e) | (f) |
|---------------------|---|---|---|--|---|---|
| |  |  |  |  |  |  |
| Theoretical K value | 0.5 | 0.7 | 1.0 | 1.0 | 2.0 | 2.0 |
| Design K value | 0.65 | 0.80 | 1.0 | 1.2 | 2.1 | 2.0 |

Table 7.2
The safety factors for large gusset plates

| | Resistance | | Test3 | Test4 | | | | |
|------------------|---------------|--------------|----------------------------------|--------------------------|-------------------------|----------------------------------|--------------------------|-------------------------|
| | LRFD (kip) | ASD (kip) | Maximum Applied load (kip) | Safety Factor LRFD | Safety Factor ASD | Maximum Applied load (kip) | Safety Factor LRFD | Safety Factor ASD |
| Tensile yielding | 1503.9 | 1000.6 | 769.8 | 2.0 | 1.3 | 1151.0 | 1.3 | 0.9 |
| Tensile rupture | 1464.7 | 976.5 | 769.8 | 1.9 | 1.3 | 1151.0 | 1.3 | 0.9 |
| Compression | 1503.9 | 1000.6 | 870.8 | 1.7 | 1.2 | 1357.7 | 1.1 | 0.7 |

Table 7.3
The safety factors for small gusset plate

| | Resistance | | Test 5 | | |
|------------------|---------------|--------------|-----------------------|-----------------------|----------------------|
| | LRFD (kip) | ASD (kip) | Applied load (kip) | Safety Factor LRFD | Safety Factor ASD |
| Tensile yielding | 865.7 | 576.0 | 656.4 | 1.3 | 0.9 |
| Tensile rupture | 801.0 | 534.0 | 656.4 | 1.2 | 0.8 |
| Compression | 865.7 | 576.0 | 861.7 | 1.0 | 0.7 |

Table 7.4
Details of the models simulated for the gusset plate and connection plate combination

| Model No. | Dimension for gusset plate | Dimension for connection plate t × w × L, in. | Deflection on the top of the gusset plate, in. |
|-----------|-------------------------------|--|---|
| GC#1 | Large | 1.5×11.375×19 | -0.055 |
| GC#2 | Large | 0.75×10×24 | -0.178 |
| GC#3 | Small | 1×9×13 | 0.018 |

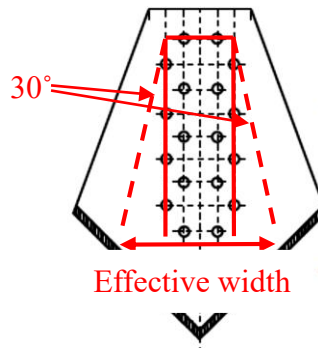


Figure 7.1 Example for using Whitmore method to determine the effective width in tension

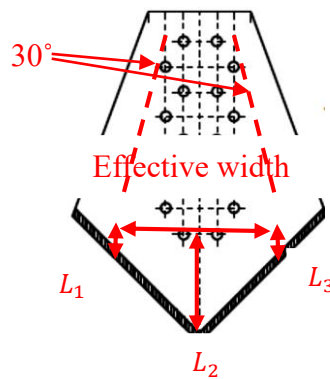


Figure 7.2 Example for showing L1, L2, L3 and the effective width when the gusset plate is in compression

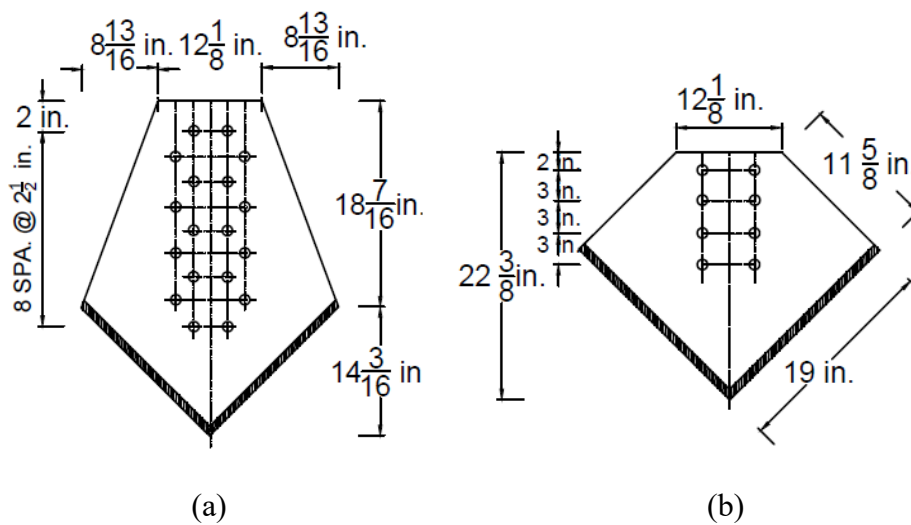


Figure 7.3 Dimensions of both large and small gusset plates:
 (a) Large and (b) Small

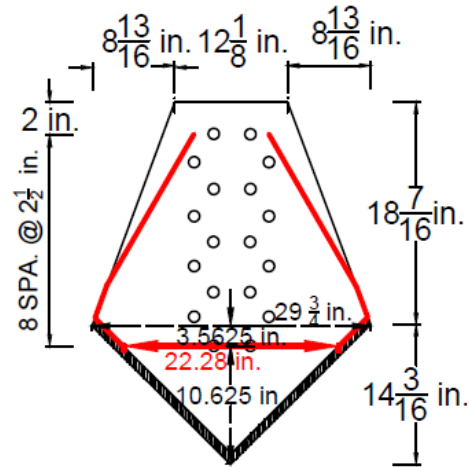


Figure 7.4 Effective Whitman width for the large gusset plate



Figure 7.5 Deformation of the gusset plate under compression

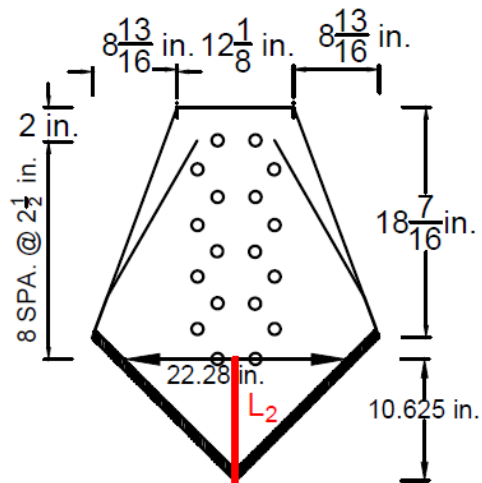
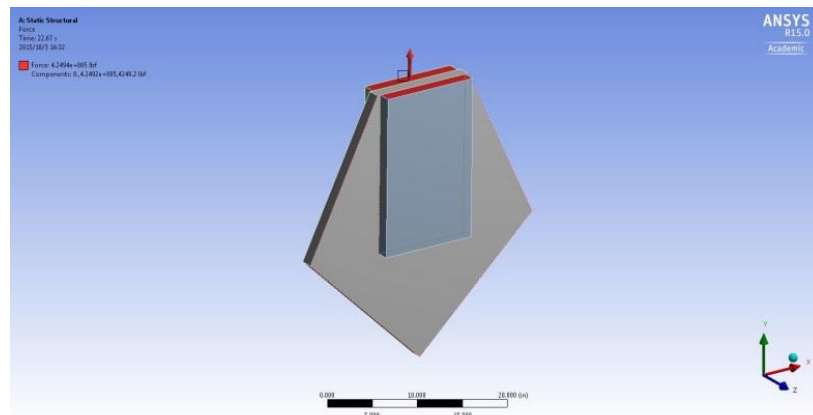
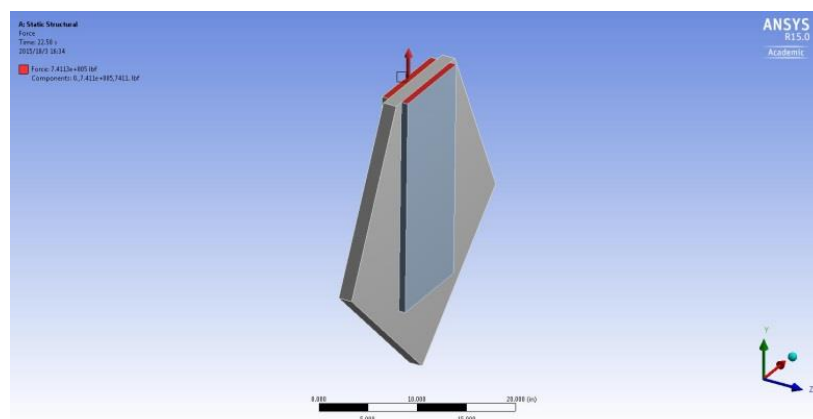


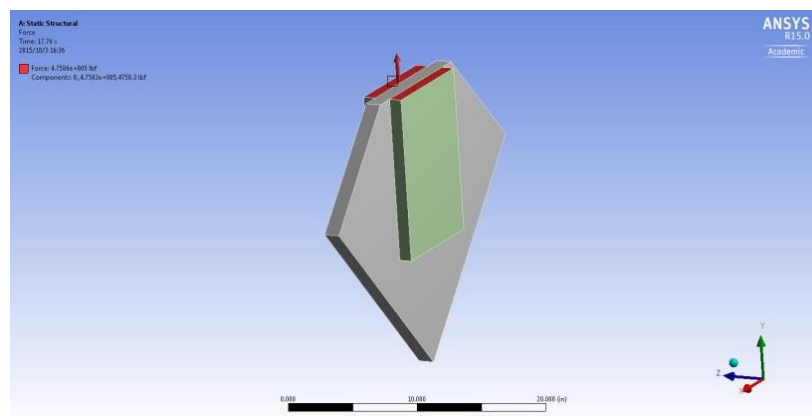
Figure 7.6 Distance L_2



(a)

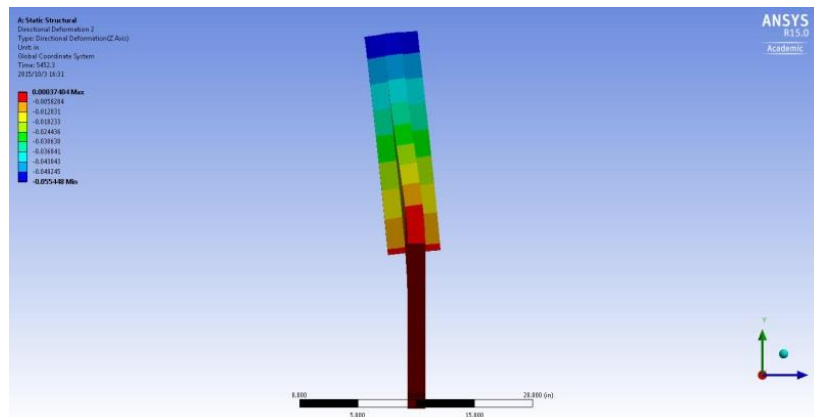


(b)

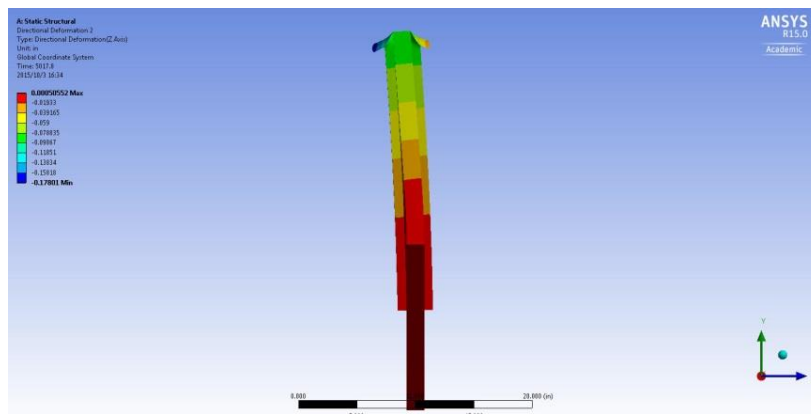


(c)

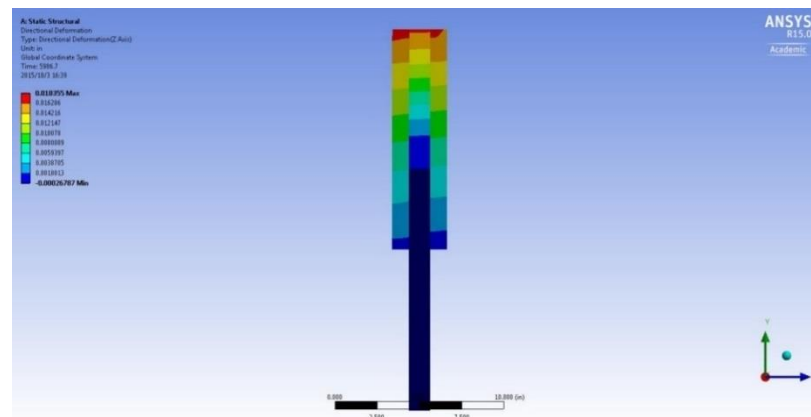
Figure 7.7 Geometry of gusset plates and connection plates for three models used in ANSYS: (a) Test 3, (b) Test 4 and (c) Test 5



(a)

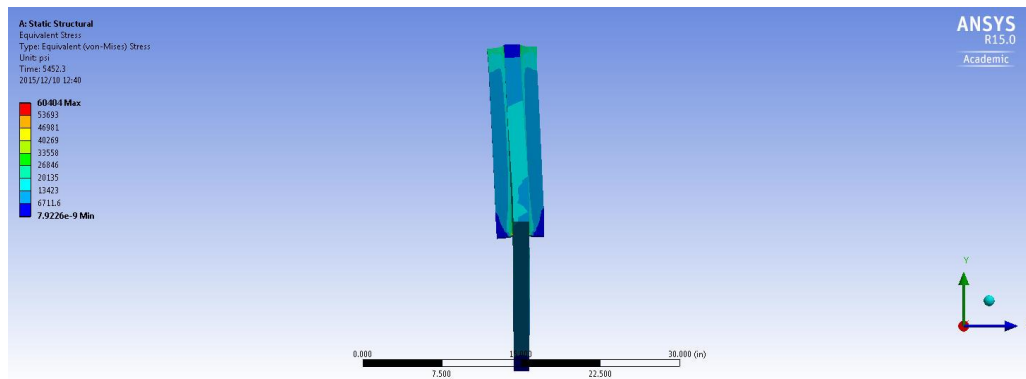


(b)

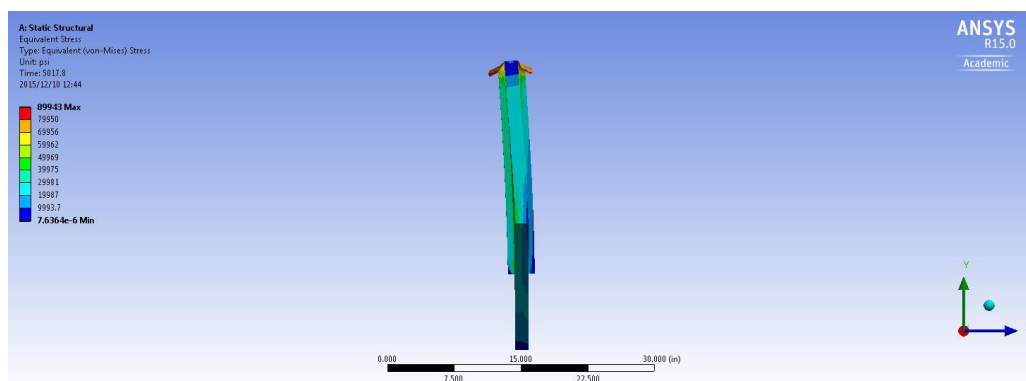


(c)

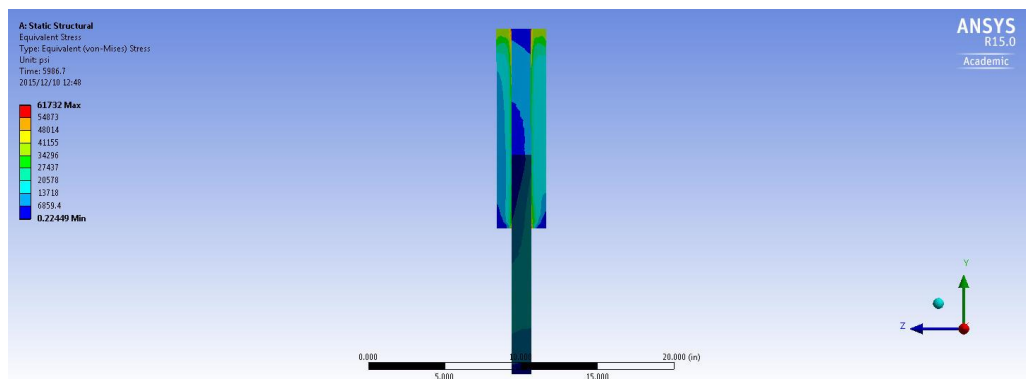
Figure 7.8 Deformation for gusset plates and connection plates in simulation for tests 3 through 5: (a) Test 3, (b) Test 4, and (c) Test 5



(a)



(b)



(c)

Figure 7.9 Von Mises stress distribution on gusset plates and connection plates in simulation for tests 3 through 5: (a) Test 3, (b) Test 4, and (c) Test 5

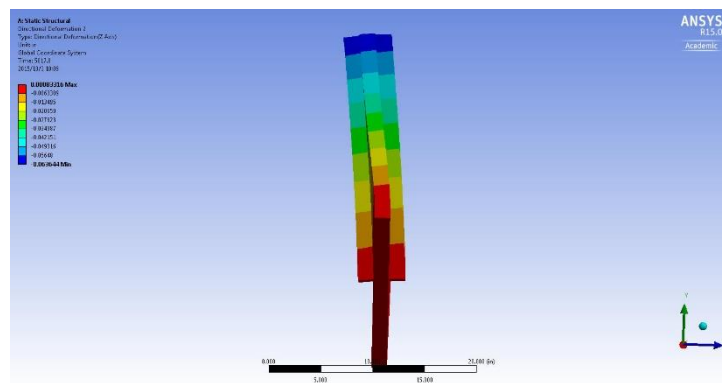


Figure 7.10 Deformation for large gusset plate and connection plates with the dimension of 1.5 in. × 10 in. × 24 in.

CHAPTER 8

SUMMARY AND CONCLUSIONS

Nine full-scale new-generation buckling restrained braces (BRBs) were tested in this investigation; they differ from conventional BRBs in that they utilize straight steel plates for the core and connection plates oriented perpendicular to the core to attach the BRB to gusset plates. This results in efficient use of the steel material and economy in manufacturing. Based on the fact that the connection plate is perpendicular to the single core or dual core plates, it is much easier to build welded, pinned, or bolted connections compared with conventional BRBs for which the connection plate and core plates are one piece.

The hysteretic loops of the nine full-scale BRBs exhibited repeatable and stable behavior with positive incremental stiffness. There was no rupture, brace instability, or brace end connection failure up to displacements corresponding to 2% story drift; the strain achieved in the core plates ranged from 2.89% to 4.16%, which is more than ten times of the yielding strain of the steel. For each cycle reaching a deformation greater than the BRB yield displacement, the maximum tension forces were greater than the nominal strength of the steel core. In other words, the strain hardening adjustment factor, ω , is greater than 1.0. In all tests, the ratio of maximum compression to maximum tension force (the compression strength adjustment factor, β) was less than 1.30. Both adjustment factors meet requirement of AISC-341 (2010).

In compression, larger cross-sectional area of the core plate helps to prevent buckling. In tension, increasing the cross-sectional area of the core plate can increase its resistance. Therefore, the cumulative hysteretic energy dissipation of the full-scale BRBs was found to increase with increasing cross-sectional area of the steel core plates. Specimens with a smaller area of steel core plates were efficient with respect to cumulative hysteretic energy dissipation per unit cross-sectional area of the steel core. Compared to conventional BRBs, new generation BRBs with a similar steel core area dissipated similar amounts of cumulative hysteretic energy. Full-scale BRBs in element tests subjected to axial load dissipated more hysteretic energy than BRBs in subassembly tests because the BRB tested in subassembly tests subjected to an initial moment; in addition to axial load, a bending moment was applied at the BRB ends. The reduced energy dissipated by the BRBs in subassembly tests is evidence that the latter are more severe than element tests. Regardless of strong-axis, weak-axis, or both strong- and weak-axis buckling, new generation BRBs performed in a satisfactory manner and met AISC-341 (2010) requirements.

Equations for the buckling force of the core plates and contact force between the concrete and the core plates are derived when strong-axis buckling happens to the core plates. The equations for the buckling force are verified with the FEM and the test results.

The mode of core plates buckling is controlled by the geometric relationship between BRB steel casing and steel core plates and is explained with the aid of a strut-and-tie model of the BRB cross-section. The general equations for the critical angle between the strut and the tie are derived, which triggers strong-axis buckling. The critical angle expressions are different for an odd wave number and an even wave number. The

calculated critical angles for the specimens are compared with the real angles obtained by the geometry of the cross-section of the BRBs. When the actual angle is close to the critical angle, either strong-axis or a combination of strong-axis and weak-axis buckling occurs in the core plates. When the real angle is much larger than the critical angle, weak-axis buckling occurs in the core plates. Simply increasing the thickness of the steel casing can make it more stable. Therefore, when the distance between the outer-edge of the core plate to the inner-edge of the steel casing (thickness of concrete) decreases, increasing the thickness of the steel casing wall can help to prevent steel casing yielding, and bulging.

The nine BRB specimens tested with cyclic load are simulated with FEM using ANSYS. The hysteretic loops and the hysteretic energy dissipation are compared to those obtained in the tests. The parameters for the model which simulated the specimen in test 3 are used for further simulation to determine the casing thickness for different lengths of the BRB. In the simulation, the axial load applied is 1.5 times the yielding force of the core plate to satisfy design recommendations. The transverse drift of BRBs applied in the simulation is the transverse displacement corresponding to the 2% interstory drift. To create the buckling performance of the BRB, the eccentricity is needed. The relationship between the eccentricity and the length of the BRB is obtained for certain cross-sectional dimensions of the casing. From this relationship, the minimum wall thickness of the steel casing can be found for certain length of the BRB without global buckling; this is valid when the performance of the BRB meets the 2% of interstory drift requirement of AISC-341 (2010).

Out-of-plane buckling of the gusset plate was observed in test 4. According to the calculation for the tensile and compressive resistant capacity of the gusset plates

following the AISC code (2011), the gusset plate used in test 3 is safe, while the gusset plates used for test 4 and 5 are not safe. However, out-of-plane buckling of the gusset plate only occurred in test 4. Therefore, the FEM is adopted to investigate further. The models of the combined gusset plate and connection plates used in tests 3 through 5 are simulated with cyclic load with 1% eccentricity. The models for test 3 and 5 had very small deflection, which was 0.055 in. and 0.018 in., respectively. The model for test 4 had a very large deflection (0.178 in.), causing out-of-plane buckling of the gusset/connection plate system. After increasing the thickness of the connection plate from 0.75 in. to 1.5 in for test 4, the model only had 0.06 in. deflection and no buckling. Therefore, the factors affecting the occurrence of out-of-plane buckling of the gusset plate include the maximum load applied on the system, the combined stiffness of the gusset plate and the connection plates, and the thickness of the connection plate. When the maximum load applied and the dimensions of the gusset plates are given, increasing the thickness of the connection plates can help prevent the out-of-plane buckling of the gusset plate.

Overall, test results verified that BRBs with connection plates perpendicular to core plates performed very well under cyclic load. The derived equation can reasonably predict axial compressive force for a given BRB. The critical angle can tell which direction of the core plate buckles for a given BRB. The critical thickness of steel casing for certain length of BRB can be found in the figures obtained from simulation results. When designing gusset plate, counting in connection plates can save material.

APPENDIX

CALCULATION OF THE DESIGN STRENGTH (LRFD)

AND ALLOWABLE STRENGTH (ASD) OF

THE SMALL GUSSET PLATES

A.1 Calculation of the Tensile Resistance of the Gusset Plate

Figure A.1 shows that effective Whitmore width for the small gusset plate, which is the summation of $2\frac{1}{2}$ in, $2\frac{1}{2}$ in, and double of $11 \times \tan(30^\circ)$. The effective Whitmore length is obtained from Eq. (A.1).

$$\text{Effective Whitmore length} = 2 \times 2\frac{1}{2} + 2 \times (3 \times 3) \tan(30^\circ) = 15.39 \text{ in.} \quad (\text{A.1})$$

The effective Whitmore length will be used to calculate the gross area of the gusset plate subject to tension and compression and net area of the gusset plate subjected to tensile rupture.

A.1.1 Calculation of Tensile Yielding Resistance of the Small Gusset Plate

The yield stress of the gusset plates is 50 *ksi*. The thickness of the gusset plate is 1.25 in. Therefore, the gross area of the gusset plate subject to tension, and the tensile yielding capacity of the gusset plate are calculated as follows:

$$A_g = 1.25 \times 15.39 = 19.24 \text{ in.}^2 \quad (\text{A.2})$$

$$R_r(LRFD) = \phi_y F_y A_g = 0.9 \times 50 \times 19.24 = 865.69 \text{ kips} \quad (\text{A.3})$$

$$R_r(ASD) = \phi_y F_y A_g = \frac{1}{1.67} \times 50 \times 19.24 = 575.97 \text{ kips} \quad (\text{A.4})$$

The data obtained from Eqs. (A.3) and (A.4) are listed in the first row of Table 7.3.

A.1.2 Calculation of Tensile Rupture Resistance of the Small Gusset Plate

The tensile rupture resistance of the gusset plate can be calculated using Eq. (7.2). The net width of the gusset plate for rupture is the effective Whitmore length, deducting the total width of the bolt holes. In the tests $1\frac{1}{8}$ in. bolts were used. The ultimate strength

of the gusset plate is 65 *ksi*. The net area of the gusset plate subjected to tensile rupture and the tensile rupture resistance of the gusset plate can be calculated as follows:

$$A_n = 1.25 \times \left[15.39 - 2 \times \left(1 + \frac{1}{8} \right) \right] = 1.25 \times 13.14 = 16.43 \text{ in}^2 \quad (\text{A.5})$$

$$R_r(\text{LRFD}) = \phi_u F_u A_n U = 0.75 \times 65 \times 16.43 \times 1 = 800.96 \text{ kips} \quad (\text{A.6})$$

$$R_r(\text{ASD}) = \phi_u F_u A_n U = \frac{1}{2} \times 65 \times 16.43 \times 1 = 533.98 \text{ kips} \quad (\text{A.7})$$

The data obtained from Eqs. (A.6) and (A.7) are listed in the second row of Table 7.3.

A.2 Calculation of the Compression Resistance of the Small Gusset Plate

The deformation of the gusset plate under compression is shown in Figure A.2. In this case, the *k* value should be chosen as 1.2 according to Table 7.1.

Figure A.3 shows the distance of L_1 , L_2 , and L_3 . Since the total depth of this gusset plate is 22.25 in. and the distance from the last row of bolts to the top section of the gusset plate is 11 in., the distance from the last row of bolts to the bottom section of the gusset plate is 11.25 in., which is the length L_2 . The horizontal distance from the center of the bottom row of bolts to one edge of the gusset plate equals the length of L_2 due to isosceles right triangle, which is 11.25 in. Therefore, the horizontal distance between the right corner of the Whitmore width and the right edge of the gusset plate is $(11.25 - 15.39/2)$ in., which is 3.555 in. Due to the geometrical symmetry, the lengths of L_1 and L_3 are the same, which is 3.555 in.

The slenderness of the gusset plate, KL/r , can be calculated as follows:

$$r = \sqrt{\frac{I_g}{A_g}} = \sqrt{\frac{15.39 \times 1.25^3 / 12}{15.39 \times 1.25}} = 0.361 \quad (\text{A.8})$$

$$L = \frac{L_1 + L_2 + L_3}{3} = \frac{3.555 + 11.25 + 3.555}{3} = 6.12 \text{ in.} \quad (\text{A.9})$$

$$\frac{KL}{r} = \frac{1.2 \times 6.12}{0.361} = 20.34 \quad (\text{A.10})$$

Since $KL/r \leq 25$, the compressive resistance of gusset plates subject to yielding and buckling can be calculated by using Eq. (7.3). The compressive resistance of the gusset plate is calculated as follows:

$$R_r(LRFD) = \phi_c F_y A_g = 0.9 \times 50 \times 15.39 \times 1.25 = 865.69 \text{ kips} \quad (\text{A.11})$$

$$R_r(ASD) = \phi_c F_y A_g = \frac{1}{1.67} \times 50 \times 15.39 \times 1.25 = 575.97 \text{ kips} \quad (\text{A.12})$$

The data obtained from Eqs. (A.11) and (A.12) are listed in the third row of Table 7.3.

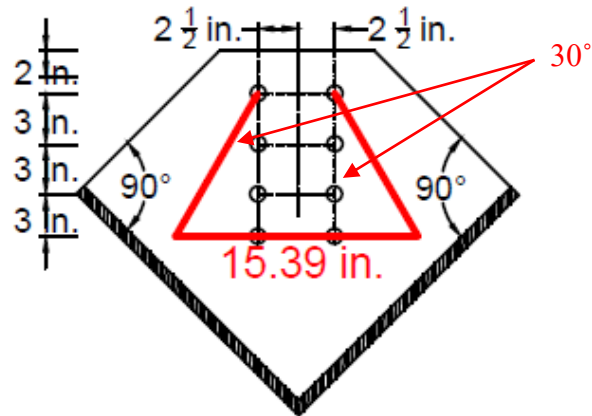


Figure A.1 Effective Whitmore length

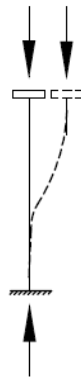
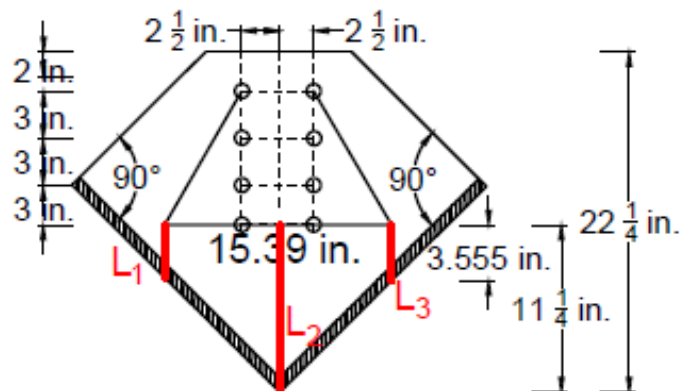


Figure A.2 The deformation of the gusset plate under compression

Figure A.3 The distance of L_1 , L_2 , and L_3

REFERENCES

- ACI (American Concrete Institute). (2014). "Building code requirements for structural concrete and commentary" *ACI 318-14*, Farmington Hills, MI.
- AISC (American Institute of Steel Construction). (2010). "Seismic Provisions for Structural Steel Buildings." *ANSI/AISC 341-10*, Chicago, IL
- AISC (American Institute of Steel Construction). (2011). "Steel Construction Manual". *AISC 325-11*, Chicago, IL
- AISC (American Institute of Steel Construction). (2010). Specification for structural steel buildings. *ANSI/AISC 360-10*, Chicago, IL
- Chou, C. and Chen, P. (2009). "Compressive behavior of central gusset plate connections for buckling-restrained braced frame." *J. Constr. Steel Res.*, 65, 1138-1148.
- Chou, C., Liu, J., and Pham, D. (2012). "Steel buckling-restrained braced frames with single and dual corner gusset connections: seismic tests and analyses." *Earthquake Eng. Struc.*, 41, 1137-1156.
- Chou, C., Chen, Y. Phan, D., and Truong, V. (2014). "Steel braced frames with dual core SCBs and sandwiched BRBs: mechanics, modeling and seismic demands". *Eng. Struct.*, 74, 26-40.
- Daniel, M. (2006). "Performance of eight buckling-restrained braces." Master Thesis, Univ. of Utah, Salt Lake City, UT.
- El-Tawil, S. and Ekiz, E. (2009). "Inhibiting steel brace buckling using carbon fiber-reinforced polymers: large-scale tests." *J. Struct. Eng.*, 10.1061/(ASCE)ST.1943-541X.0000003, 530-538.
- Fahnestock, L. A., Ricles, J. M. and Sause, R. (2007). "Experimental evaluation of a large-scale buckling-restrained braced frame". *J. Struct. Eng.*, 10.1061/(ASCE)0733-9445(2007)133:9(1205), 1205-1214.
- Genna, F., and Gelfi, P. (2012). "Analysis of the lateral thrust in bolted steel buckling-restrained braces. I: experimental and numerical results." *J. Struct. Eng.*, 10.1061/(ASCE)ST.1943-541X.0000558, 1231-1243

Hikino, T., Okazaki, T., Kajiwara, K. and Nakashima, M. (2013). "Out-of-plane Stability of Buckling-Restrained Braces Placed in Chevron arrangement." *J. Struct. Eng.*, 10.1061/(ASCE)ST.1943-541X,0000767,1812-1822.

Ibrahim, F. I. S. (2009). "Loading rating guidance and examples for bolted and riveted gusset plates in truss bridges." US Department of Transportation Federal Highway Administration.

Ju, Y., Kim, M., Kim, J., and Kim, S. (2009). "Component tests of buckling-restrained braces with unconstrained length." *Eng. Struct.*, 31, 507-516.

Koetaka, Y., Kinoshita, T., Inoue, K., and Iitani, K. (2008). "Criteria of buckling-restrained braces to prevent out-of-plane buckling." *The 14th World Conf. on Earthquake Engineering*, Beijing, China.

Lin, P., Tsai, K., Wang, K., Yu, Y., Wei, C., Wu, A., Tsai, C., Lin, C., Chen, J., Schellenberg, A., Mahin, S. and Roeder, C. (2012). "Seismic design and hybrid tests of a full-scale three-story buckling-restrained braced frame using welded end connections and thin profile." *Earthquake Eng. Struct.*, 41, 1001-1020.

Liu, L., Liu, C., and Yin, X. (2012). "Experimental verification of a full-size buckling restrained brace." *Appl. Mech. Mater.*, 166-169, 3147-3150.

Mazzolani, F. M., Corte, G. D., and D'Aniello, M. (2009). "Experimental analysis of steel dissipative bracing systems for seismic upgrading." *J. Civ. Eng. Manag.*, 15(1), 7-19.

Midorikawa, M., Asari, T., Iwata, M., Murai, M. and Tanaka, Y. (2012). "Cyclic behavior of buckling-restrained braces using steel mortar planks; buckling mode number and strength ratio." *15th WCEE*, Lisbon, Portugal.

Miller, D. J., Fahnestock, L.A., and Eatherton, M. R. (2012). "Development and experimental validation of nickel-titanium shape memory alloy self-centering buckling-restrained brace." *Eng. Struct.*, 40, 288-298.

Okazaki, T., Hikino, T. and Kajiwara, K. (2012). "Out-of-plane stability of buckling-restrained braces." *15th WCEE*, Lisbon, Portugal.

Palazzo, G., Lopez-Almansa, F., Cahis, X., and Crisafulli, F. (2009). "A low-tech dissipative buckling restrained brace: design, analysis, production and testing." *Eng. Struct.*, 31, 2152-2161.

Rabbat, B. and Russell, H. (1985). "Friction coefficient of steel on concrete or grout." *J. Struct. Eng.*, 10.1061/(ASCE)0722-9445(1985)111:3(505), 505-515.

Rahai, A. R., Alinia, M. M., and Salehi, S. M. F. (2009). "Cyclic performance of

buckling restrained composite braces composed with selected materials.” *Int. J. Civ. Eng.*, 7(1), 1-8.

Shanley, F. R. (1947). "Inelastic column theory." *J. Aeronautical Sci.*, 14 (5), 261-268.

Shen, B. and Deng, C. (2007). "Continuous transition from point contact to line contact between the axially compressed inner core and the flexible sleeve in a sleeved column." *Eng. Mech.*, 24(2), 154-160.

Staker, R. (2002). "Selected study on buckling restrained braces." Master Thesis, Univ. of Utah, Salt Lake City, UT.

Sun, F., Li, G., Guo, X., Hu, D., and Hu, B. (2011). "Development of new-type buckling-restrained braces and their application in aseismic steel frameworks." *Adv. Struc. Eng.*, 14(4), 717-730.

Takeuchi, T., Matsui, R., Tada, T., and Nishimoto, K. (2012). "Out-of-plane stability of buckling-restrained braces including their connections." *15th WCEE*. Lisbon, Portugal.

Takeuchi, T., Ozaki, H., Matsui, R. and Sutcu, F. (2014). "Out-of-plane stability of buckling restrained braces including moment transfer capacity." *Earthquake Eng. Struc.*, 43, 851-869.

Timoshenko, P. S., and Gere, M. J. (1961). *Theory of elastic stability: Inelastic buckling of bars*, Engineering Societies Monographs, New York, 175-177.

Tremblay, R., Bolduc, P., Neville, R. and Devall, R. (2006). "Seismic testing and performance of buckling-restrained bracing systems." *Can. J. Civil Eng.*, 33, 183-198

Tsai, K., Hsiao, P., Wang, K., Weng, Y., Lin, M., Line, K., Chen, C., Lai, J., and Lin, S. (2008). Pseudo-dynamic tests of a full-scale CFT/BRB frame-part II: seismic performance of buckling-restrained braces and connections. *Earthquake Eng. Struc.*, 37, 1099-1115.

Wang, C., Usami, T., Funayama, J., and Imase, F. (2013). "Low-cycle fatigue testing of extruded aluminum alloy buckling restrained braces." *Eng. Struct.*, 46, 294-301.

Watanabe, A., Hitomi, Y., Saeki, E., Wada, A., and Fujimoto, M. (1988). "Properties of brace encased in buckling-restraining concrete and steel tube." *Proc., 6th World Conf. on Earthquake Engineering*. Vol. IV. Tokyo-Kyoto, Japan, 719-724.

Wu, J., Liang, R., Wang, C. and Shi, J. (2012). "Research on the multi-wave buckling process of the core component of the buckling-restrained brace." *Eng. Mech.*,

29(8), 136-142.

Wu, A., Lin, P. and Tsai, K. (2014). "High-mode buckling responses of buckling-restrained brace core plates". *Earthquake Eng. Struc.*, 43(3), 375-393.

Yoshino, T. and Karino, Y. (1971). "Experimental study on shear wall with braces: part2". *Summaries of Technical Papers of Annual Meeting, Architectural Institute of Japan, Structural Engineering Section*. 11, 403-404 (in Japanese).

Zhao, J., Wu, B., Li, W., and Ou, J. (2014). "Local buckling behavior of steel angle core members in buckling-restrained braces: cyclic tests, theoretical analysis, and design recommendations." *Eng. Struct.*, 66, 129-145.

Zsarnoczay, A. (2013). "Experimental and numerical investigation of buckling restrained braced frames for Eurocode conform design procedure development." Ph.D. dissertation, Budapest Univ. of Technology and Economics. Hungary21